

**MECHANICAL PROPERTIES OF A ZR-BASED BULK
METALLIC GLASS UNDER TENSILE CONFINEMENT
CONDITION**

WANG ZHITAO

NATIONAL UNIVERSITY OF SINGAPORE

2012

**MECHANICAL PROPERTIES OF A ZR-BASED BULK
METALLIC GLASS UNDER TENSILE CONFINEMENT
CONDITION**

WANG ZHITAO

(B. Eng, HIT)

(M. Eng, HIT)

A THESIS SUBMITTED

FOR THE DEGREE OF DOCTOR OF PHILOSOPHY

DEPARTMENT OF MATERIALS SCIENCE &

ENGINEERING

NATIONAL UNIVERSITY OF SINGAPORE

2012

Declaration

I hereby declare that the thesis is my original work and it has been written by me in its entirety. I have duly acknowledged all the sources of information which have been used in the thesis.

This thesis has also not been submitted for any degree in any university previously.

WANG ZHITAO

3 August 2012

Acknowledgements

First of all, I would like to express my sincere gratitude to my supervisor, Professor Li Yi, who is a dedicated scientist, supportive friend and grateful teacher. Over the past four years, his great vision and rigorous attitude towards scientific issues have enlightened me on my way of research. I have learned from him how to do research, and more importantly, how to think properly and scientifically, which I believe would benefit me for the rest of my life. I cherished the memory of discussion and argument with him each Saturday afternoon. I feel deeply indebted to him and thank him again.

I am also grateful to Associate Professor Zeng Kaiyang from department of mechanical engineering, NUS. His valuable suggestions on nanoindentation have benefited me tremendously. I would like to thank the technicians, Wang Weide and Shen Lu at IMRE, for their constant support and help on the experiment. I would like to thank the laboratory technologists in department of materials science and engineering, especially Mr. Chan, Agnes, Chen Qun and Roger. I wish to express my appreciation to the technical staff at Impact lab in department of mechanical engineering, especially Joe and Mr. Chaim. Without their help, I cannot finish my project.

Special appreciation is given to group members of our Non-Equilibrium Materials Lab, former seniors Drs. Wu Wenfei, Yang Hai, Han Zheng, Grace Lim, Guo Qiang and Wang Zhiyu. It was very nice for me to work with them. I also like to thank the current colleagues Wang Yinxiao, Dr. Pan Jie, Zuo Lianyong and Aaron Ong.

I am grateful to my friends in Singapore, Deng Qinqiu, Liu Li, Yang Yang, Liu Zijuan and Liu Jing. I have enjoyed the time we spent together and remebered the happy time I lived in Singapore.

Finally, I feel deeply indebted to my families. I would like to express my sincerest gratitude to my parents for raising me up and their unconditional love. I miss you two very much these four years. I also would like to thank my wife, Ye Linying, for her love and sacrifice these years.

July 2012, Singapore

Wang Zhitao

Table of Contents

Declaration	i
Acknowledgements	ii
Table of Contents	iv
Summary	vii
List of Tables	x
List of Figures	xi
Chapter 1 Introduction	1
1.1 Background knowledge of metallic glasses (MGs)	1
1.2 Deformation mechanisms of BMGs	7
1.2.1 Deformation map	7
1.2.2 Deformation models	9
1.3 Mechanical behavior of BMGs at room temperature	15
1.3.1 Yield criteria	15
1.3.2 Plasticity	18
1.3.3 Mechanical behavior under confinement condition	24
1.4 Objective and outline of this thesis	26

Chapter 2 Experimental Procedures	29
2.1 Alloy preparation	29
2.2 Structure characterization	30
2.3 Thermal testing	33
2.4 Mechanical testing.....	33
2.4.1 Uniaxial compression.....	33
2.4.2 Tensile testing.....	34
2.4.3 Micro-hardness testing	36
Chapter 3 Achieving tensile ductility of BMGs at room temperature.....	38
3.1 Introduction.....	38
3.2 Results	42
3.2.1 Deformation behavior of circumferentially-notched samples	42
3.2.2 Deformation behavior of slit-notched samples	50
3.2.3 Deformation behavior of rectangularly-notched samples.....	57
3.2.4 Deformation behavior of a 5 mm cylindrical sample with Bridgman notch	60
3.3 Discussion.....	72
3.3.1 Comparison between homogeneous deformation at high temperature and at room temperature.....	72
3.3.2 Variation of tensile ductility as stress state parameter.....	73
3.4 Conclusion.....	75
Chapter 4 Approaching ideal tensile strength of BMG.....	77
4.1 Introduction.....	77
4.2 Results and discussion.....	80
4.2.1 Variation of tensile stress as stress state parameter.....	80
4.2.2 Approaching ideal tensile strength.....	81

4.2.3 Fracture morphology under tensile confinement	86
4.3 Conclusion	92
Chapter 5 Strain hardening and densification in metallic glass	94
5.1 Introduction.....	94
5.2 Results	96
5.2.1 Strain hardening characterized by micro hardness	96
5.2.2 Densification characterized by DSC	104
5.3 Discussion.....	108
5.3.1 The possibility of crystallization of BMGs during plastic deformation.....	108
5.3.2 Comparison between thermal annealing and mechanical annealing for BMGs	110
5.3.3 Strain hardening mechanism in BMG	112
5.4 Conclusion.....	114
Chapter 6 Concluding remarks	116
6.1 Summary of this thesis.....	116
6.2 Future work.....	119
Bibliography	121

Summary

In the absence of structural defects such as dislocations and grain boundaries in crystalline materials, bulk metallic glasses (BMGs) exhibit unique mechanical properties as compared to their crystalline counterparts, such as high strength and high elastic strain. However, the Achilles heel of BMGs is that they lack of plasticity at room temperature, which is detrimental to their application as engineering materials. Abundant works have been conducted on the mechanical behavior of BMGs under compression over past decade; however, there is limited work on the tensile behavior of monolithic bulk metallic glasses. Thus, there is a compelling need for research studying the mechanical behavior of BMGs under tension, both for a better understanding of the fundamental mechanism and for supporting the application of BMGs as practical engineering materials.

This work employs tensile tests to study mainly the mechanical behaviors of monolithic bulk metallic glass (BMG) at room temperature. Through designing series of tensile confinement samples and carrying out systematic experiments, this work aims to reveal, essentially, tensile plastic deformation, tensile strength, and fracture mechanism of metallic glass. Our

ultimate goal is to provide insights for understanding the mechanical behavior of BMGs.

The first significant finding of this work is achieving tensile ductility in a variety of confined BMGs at room temperature. It is revealed that tensile elongation can reach up to ~25 % before fracture, and homogeneous tensile plasticity can reach as high as 10 %, which are both records for the deformation of BMGs. Such extraordinary tensile ductility is in sharp contrast to the usually observed negligible plastic deformation for BMGs at room temperature. The tensile plasticity exhibited by BMGs under confinement condition provides a useful guideline for engineers in selection of BMGs as structural materials.

High strength is a long-standing goal for structural materials and is the primary considering factor for engineering applications. BMGs are considered to possess high strength, corresponding to the strength of $\sim E/50$. The second contribution of this work is to identify the ultrahigh tensile strength of BMG. Through investigating the tensile strength variation of BMG samples with various stress state, it is revealed that tensile strength is as high as 3.6 GPa, which is comparable to that computed from Griffith's theory. This value is approximately $E/20$ (where E is Young's modulus), approaching the theoretic strength limit and placing BMG among the highest strength materials. In addition, the unique fracture features, namely cracks, micro voids and

'dimple-like' structure are also revealed in this work. These features are in contrast to the conventional reported core and radiating veins tensile features. Such fracture morphology provides insights not only for understanding fracture mechanism but also for analyzing the failure of BMG component.

Finally, the major contribution of this work is to uncover the strain hardening behavior of metallic glass. This phenomenon is in sharp contrast to the usual observations of deformation induced 'strain softening' in metallic glasses, where the plastic strain is accommodated by shear bands. We believe this 'strain hardening' behavior is attributed to the densification of the structure induced by high level of tensile stress. We propose that metallic glass can behave like ductile crystalline materials if it is 'shear band free'. This work is the first to provide the definitive prove that deformation induced hardening can occur in monolithic BMGs, and is of paramount importance for reinterpreting the mechanical behavior of metallic glass.

List of Tables

Table 1.1 Representative bulk metallic glass compositions with critical size larger than 10 mm and the year of first reporting.	4
Table 1.2 Application fields that currently have been proceeded for BMGs, adapted from [29].	6
Table 3.1 Mechanical properties of circumferentially notched and slit notched samples.	53
Table 3.2 Stress state parameter calculated by Bridgman’s analysis.	74
Table 4.1 Experimentally measurd ultra-high strengths in metals.	85
Table 5.1 Geometries of the samples for compression, tension and annealing tests.	97
Table 5.2 Thermal properties of the as-cast, annealed and plastically deformed samples corresponding to Figure 5.7.	106

List of Figures

Figure 1.1 Schematic diagram of time-temperature-transformation (TTT) for glass formation by rapid quenching of a liquid without crystallization. Line a corresponds to crystallization at low cooling rate, line b corresponds to vitrification at high cooling rate.....2

Figure 1.2 Schematic deformation map for an amorphous metal illustrating the temperature and stress regions for homogeneous and inhomogeneous plastic flow, adapted from [31].....8

Figure 1.3 Two-dimensional schematics of the atomistic deformation mechanisms proposed for amorphous metals (a) free volume model (b) shear transformation zone model, reproduced from [53].11

Figure 1.4 Comparison of typical fracture surfaces of $Zr_{59}Cu_{20}Al_{10}Ni_8Ti_3$ metallic glassy specimens induced by a) compressive loading and b) tensile loading, adapted from [75].16

Figure 1.5 TEM bright-field images of in situ tested Zr-based monolithic MG samples with a gauge dimension of about $100 \times 100 \times 250 \text{ nm}^3$, showing a) necking, and b) stable shear, adapted from [104].21

Figure 1.6 SEM micrographs showing the microstructure of the BMG matrix composites labeled as a) DH1 and b) DH3 where the dark contrast is from the glass matrix and the light contrast is from the dendrites. c) The corresponding tensile engineering stress-strain curves of composites DH1 and DH3, together with the curves of another composite DH2 and a monolithic BMG (Vitreloy 1), adapted from [115].22

Figure 1.7 a) The SEM micrograph of necking in $Zr_{39.6}Ti_{33.9}Nb_{7.6}Cu_{6.4}Be_{12.5}$ BMG matrix composites, and b) Brittle fracture representative of all monolithic BMGs, adapted from [115].	22
Figure 1.8 Engineering tensile stress–strain curves of the BMG composites. Dashed lines indicate the unloading process. Top inset shows the outer appearance of the tensile samples pre-strained at the different stages and the lower inset shows the true tensile stress–strain curves, indicating a significant strain-hardening behavior, adapted from [116].	23
Figure 1.9 Decrease in hardness (nanoindentation and Vickers at two different loads) with increasing plastic strain, adapted from [103].	25
Figure 2.1 Optical image of the arc-melting furnace with a cylindrical copper mold of 5 mm in diameter.	30
Figure 2.2 XRD pattern of the as-cast $Zr_{64.13}Cu_{15.75}Ni_{10.12}Al_{10}$ rod with a diameter of 5 mm.	31
Figure 2.3 DSC trace of the as-cast $Zr_{64.13}Cu_{15.75}Ni_{10.12}Al_{10}$ rod with a diameter of 5 mm., showing the glass transition temperature (T_g) and onset of crystallization temperature (T_x).	32
Figure 2.4 Schematic illustration of the confined tensile bars used in this study: a) circumferentially-notched round samples with a notch angle α of 120°, 90° and 45°, respectively, b) slit-notched samples with aspect ratios (a/q) of 2, 1 and 0.5, respectively, c) rectangularly-notched samples with width 2.0 mm and height 0.5 mm, d) a 5 mm rod with a fixed aspect ratio of 0.19 ($a=2.6$ mm, $q=0.5$ mm).	36
Figure 3.1 Variation of shear stress with the angle between shear plane and stress axis. The inset shows the resolved tensile stress σ and shear stress τ in the shear plane of angle θ .	41
Figure 3.2 Optical image (OM) of the circumferentially-notched samples with angles of 120°, 90° and 45°, respectively.	43

Figure 3.3 SEM images of the circumferentially-notched samples with angles of 120°, 90° and 45°, respectively.....	43
Figure 3.4 Nominal tensile stress-extension curves for circumferentially-notched $Zr_{64.13}Cu_{15.75}Ni_{10.12}Al_{10}$ BMG, with notch angles of 120°, 90° and 45°, respectively.....	44
Figure 3.5 SEM image showing the side view of a 120° notched sample after fracture, with multiple shear bands on the surface.....	46
Figure 3.6 SEM images of a circumferentially-notched sample with a notch angle of 90° before fracture. The higher magnification of A and B in a) are shown in b) and c), respectively.....	47
Figure 3.7 SEM images of a circumferentially-notched sample with a notch angle of 45° before fracture. The higher magnification of A in a) is shown in b), and the higher magnification of four corners illustrated in a) are shown in c)-f), respectively.	49
Figure 3.8 SEM images of the side view of circumferentially-notched samples with notch angles of 120°, 90° and 45° after fracture, respectively.	50
Figure 3.9 Optical image of the slit-notched samples with aspect ratios of 2:1, 1:1 and 0.5:1, respectively.....	51
Figure 3.10 SEM images of the slit-notched samples with aspect ratios of 2:1, 1:1 and 0.5:1, respectively.....	51
Figure 3.11 Tensile net stress-extension curves for slit-notched samples, with aspect ratios of 2:1, 1:1 and 0.5:1, respectively.	52
Figure 3.12 SEM images of the side view of the slit-notched samples after fracture, with aspect ratios of 2:1, 1:1 and 0.5:1, respectively. The fracture angles for a), b) and c) are approximately 57°, 45° and 63°, respectively.	53

Figure 3.13 SEM images of a slit-notched sample with aspect ratio of 1:1 before rupture. Side view of the sample is shown in a), rotating 180° of the same sample c), higher magnification shown in b) and d).	55
Figure 3.14 Loading-unloading curves of a slit-notched sample with aspect ratio of 0.5:1, unloading at 2.1 GPa.....	55
Figure 3.15 SEM images of the corresponding unloading sample of an aspect ratio of 0.5:1. The initial morphology of the sample before tension a), unloading at about 2.1 GPa b), rotating 180° of the unloading sample c).	56
Figure 3.16 Representative stress-extension curve of the rectangularly-notched sample. The inset shows the SEM image of the rectangularly-notched sample before tension.	57
Figure 3.17 Loading-unloading curves of the rectangularly-notched sample and the bare rods without notch. The insets show the morphology of the rectangularly-notched sample and the bare rod.	58
Figure 3.18 SEM images of the rectangularly-notched sample unloading at 2.2 GPa. a) before tensile testing, and b) after tensile testing. The higher magnification of the sample before c) and after d) tensile testing.	60
Figure 3.19 Schematic illustration of the 5 mm cylindrical sample with Bridgman notch shown in a). The optical image and SEM image of the Bridgeman notched sample are shown in b) and c).....	61
Figure 3.20 Tensile stress-strain curves of the 5 mm cylindrical rod with Bridgman notch. The inset shows a sample before and after tensile testing, showing 9.3 % elongation in the loading direction.	63
Figure 3.21 Tensile behavior and corresponding in-situ camera shooting strain of the 5 mm cylindrical rod with Bridgman notch. a) Stress-strain curve calculated from the raw load-extension data. b) In-situ camera shooting strain at the places marked in the stress-strain curve. c) higher magnification images of the shooting strain, together with the measurement from the reflected light spot at notch surface.	65

Figure 3.22 Loading-unloading tensile behavior and corresponding in-situ camera shooting strain of the 5 mm cylindrical rod with Bridgman notch. a) Stress-strain curve calculated from the raw load-extension data. b) In-situ camera shooting strain at the places marked in the stress-strain curve. c) SEM images of the testing sample before and after unloading.67

Figure 3.23 Representative cross sectional SEM image of a 7 % plastically deformed sample, showing no voids or microcracks. The inset shows the entire morphology of the plastically deformed notch.....68

Figure 3.24 Schematic illustration of the plastically deformed sample through different deformation modes. a) original sample before deformation, b) plastically deformed through shear banding, showing multiple intersecting shear bands, c) plastically deformed through homogeneous deformation, showing shear offsets on the surface due to stress concentration.69

Figure 3.25 SEM images of the morphologies of plastically deformed samples. a) surface morphology of a tensile sample of 7% ductility, showing shear offsets, b) surface morphology of a 8% compressed sample with gauge dimension similar to the tensile sample, showing shear bands, c) cross-sectional morphology of the 7% ductility sample, showing shear offsets on the outer surface.70

Figure 3.26 Schematic illustration of the geometry at the neck.73

Figure 3.27 Extension as a function of stress state parameter75

Figure 4.1 Schematic map of material ideal strengths for metals and ceramics. The blue and red dashed lines showing the boundary of strengths for metals and ceramics, respectively. s_m and t_m denote the maximum shear and tensile strength of a perfect crystal, adapted from [150].79

Figure 4.2 Tensile stress as a function of stress state parameter81

Figure 4.3 Correlation between fracture strength and Young's modulus. The data in this work is tested under tensile confinement condition. The data for crystalline materials are also shown for comparison [4].	82
Figure 4.4 Atomistic model of ideal tensile strength.	83
Figure 4.5 Representative fracture morphology of circumferentially-notched sample with a notch angle of 120°.	87
Figure 4.6 Representative fracture morphology of circumferentially-notched sample with a notch angle of 90°.	88
Figure 4.7 Representative fracture morphology of circumferentially-notched sample with a notch angle of 45°.	89
Figure 4.8 Fracture morphology of slit-notched samples with various aspect ratios. a) b) aspect ratio 2:1, c) d) aspect ratio 1:1, e) f) aspect ratio 0.5:1.	90
Figure 4.9 Representative fracture morphology of the 5 mm cylindrical sample with Bridgeman notch.	92
Figure 5.1 Stress-strain curves of BMG samples under compression and tension with different aspect ratios.	98
Figure 5.2 SEM images showing the side view of BMG samples after fracture. a) compression 2:1 sample, b) compression 1:1 sample, c) tension 2:1 sample, d) tension 1:5 sample.	99
Figure 5.3 Mircohardness traces of the plastically deformed samples with different permanent strain. The inset shows the trace of hardness measurement.	100
Figure 5.4 Mircohardness traces of the annealed samples.	102

Figure 5.5 SEM images of the indent morphology. a) 2 mm away from the center of a 7% plastically deformed sample, b) center of the corresponding 7% plastically deformed sample, c) 573 K annealed sample.....	103
Figure 5.6 SEM images of the samples for DSC testing. a) a plastically deformed sample, b) an undeformed reference.	104
Figure 5.7 DSC curves of the plastically deformed and annealed samples.	105
Figure 5.8 Variation of Normalized relaxation enthalpy and Vickers hardness as a function of plastic strain.	107
Figure 5.9 TEM images of as-cast, 2% plastically deformed and 7% plastically deformed sample.	109
Figure 5.10 Variation of Vickers hardness as a function of reduced relaxation enthalpy.	112

Chapter 1

1 Introduction

1.1 Background knowledge of metallic glasses (MGs)

Solid is one of the three classical states of matter, with the other two being liquid and gas. It can be further divided into two sub-categories based on the arrangement of its constituents. If the atoms, molecules or ions that consist of the solid are arranged with long-range order, it is known as crystal. But in other materials, there is no long-range order. These materials are called non-crystalline (amorphous) solid. The earliest amorphous solid that humans used is glass. Glassmaking by humans can be traced back to 2500 BCE in Mesopotamia (i.e. modern Iraq), and was subsequently developed by the Roman Empire. Nowadays, glass plays an important role in science and

industry and is widely used in our daily life. For example, it can be made into containers, optical components, laboratory equipment and glassy arts.

Unlike conventional metals which are normally crystalline materials, metals can also form glasses, which refer to as metallic glasses or glassy alloys. Metallic glasses can be prepared by rapid solidification of the molten alloy so that crystallization can be bypassed (**Figure 1.1**).

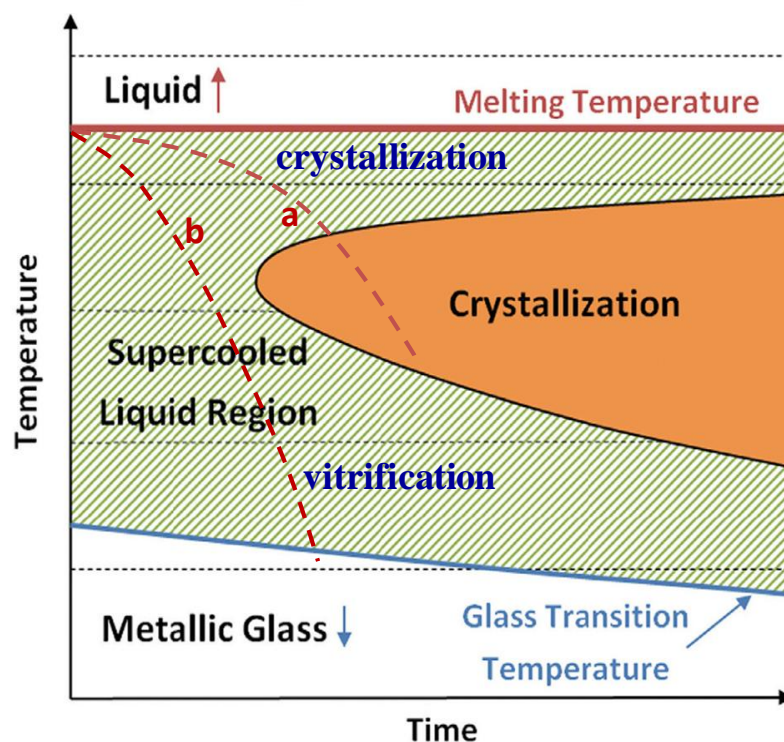


Figure 1.1 Schematic diagram of time-temperature-transformation (TTT) for glass formation by rapid quenching of a liquid without crystallization. Line a corresponds to crystallization at low cooling rate, line b corresponds to vitrification at high cooling rate.

The first discovery of metallic glasses was reported in Au-25at.%Si alloy at Caltech by Duwez in 1960 [1]. After this foundation work, enormous work has been carried out to find metallic glasses in various alloy systems, which

was facilitated by the development of rapid quenching technique. However, the size of metallic glasses was limited in micrometers due to the requirement of high cooling rate (on the order of 10^6 K/s) to avoid crystallization. In 1969, a Pd-based metallic glass, whose size was larger than 1 mm, was reported to have a low critical cooling rate between 10^2 - 10^3 K/s [2]. If millimeter scale is defined as bulk, that alloy was the first reported bulk metallic glass (BMG). In the early 1980s, a 1-cm-diameter ingot of fluxed $\text{Pd}_{40}\text{Ni}_{40}\text{P}_{20}$ glass was discovered [3].

Beginning from 1988, Inoue's group at Tohoku University, carried out systematic searches for bulk metallic glasses in multi-component systems, which boosted the interest in the discovery of bulk metallic glasses [4]. In 1992, a Zr-based Be-bearing alloy, namely $\text{Zr}_{41.2}\text{Ti}_{13.8}\text{Cu}_{12.5}\text{Ni}_{10}\text{Be}_{22.5}$ (Vitreloy 1), was successfully developed at Caltech by Johnson and co-workers [5]. This bulk metallic glass is the first commercial amorphous alloy. Today, dozens of centimeter-sized BMGs in a variety of alloy systems have been reported [6-22].

Table 1.1 summarizes the compositions and critical sizes in various bulk metallic glasses forming alloy systems. All these alloys are based on multicomponent system with at least three elements, and the critical cooling rate could be as low as 1 K/s.

Table 1.1 Representative bulk metallic glass compositions with critical size larger than 10 mm and the year of first reporting.

Base metal	Composition (atomic %)	Critical diameter (mm)	Production method	Year	Ref.
Pd-based	Pd ₄₀ Ni ₄₀ P ₂₀	10	Fluxing	1984	[3]
	Pd ₄₀ Cu ₃₀ Ni ₁₀ P ₂₀	72	Water quenching	1997	[6]
Zr-based	Zr ₆₅ Al _{7.5} Ni ₁₀ Cu _{17.5}	16	Water quenching	1993	[7]
	Zr _{41.2} Ti _{13.8} Cu _{12.5} Ni ₁₀ Be _{22.5}	25	Copper mold casting	1996	[22]
	Zr ₄₆ Cu _{30.1} Ag _{8.36} Al ₈ Be _{7.5}	72	Copper mold casting	2011	[8]
Cu-based	Cu ₄₆ Zr ₄₂ Al ₇ Y ₅	10	Copper mold casting	2004	[9]
	Cu ₄₉ Hf ₄₂ Al ₉	10	Copper mold casting	2006	[10]
Rear Earth-based	Y ₃₆ Sc ₂₀ Al ₂₄ Co ₂₀	25	Water quenching	2003	[11]
	La ₆₂ Al _{15.7} Cu _{11.15} Ni _{11.15}	11	Copper mold casting	2003	[12]
Mg-based	Mg ₅₄ Cu _{26.5} Ag _{8.5} Gd ₁₁	25	Copper mold casting	2005	[13]
	Mg ₆₅ Cu _{7.5} Ni _{7.5} Zn ₅ Ag ₅ Y ₅ Gd ₅	14	Copper mold casting	2005	[14]
Fe-based	Fe ₄₈ Cr ₁₅ Mo ₁₄ Er ₂ C ₁₅ B ₆	12	Copper mold casting	2004	[15]
	(Fe _{44.3} Cr ₅ Co ₅ Mo _{12.8} Mn _{11.2} C _{15.8} B _{5.9}) _{98.5} Y _{1.5}	12	Copper mold casting	2004	[16]
	Fe ₄₁ Co ₇ Cr ₁₅ Mo ₁₄ C ₁₅ B ₆ Y ₂	16	Copper mold casting	2005	[18]
Co-based	Co ₄₈ Cr ₁₅ Mo ₁₄ C ₁₅ B ₆ Er ₂	10	Copper mold casting	2006	[17]
Ti-based	Ti ₄₀ Zr ₂₅ Cu ₁₂ Ni ₃ Be ₂₀	14	Copper mold casting	2005	[19]
Ca-based	Ca ₆₅ Mg ₁₅ Zn ₂₀	15	Copper mold casting	2004	[20]
Pt-based	Pt _{42.5} Cu ₂₇ Ni _{9.5} P ₂₁	20	Water quenching	2004	[21]

Due to the unique structure of metallic glasses, they exhibit very different properties such as high strength, high corrosion resistance and excellent soft magnetism, which made them promising materials for future structural, chemical and magnetic application. Among these properties, the mechanical properties of BMGs have received enormous attention in the past decade [23-25]. For example, metallic glasses exhibit unique mechanical properties, such as high strength, high elastic limit (about 2%), and high hardness.

It was reported by Inoue's group that the fracture strengths of Co-Fe-Ta-B [26] and Co-Fe-Ta-B-Mo [27] reach to 5.2 GPa and 5.5 GPa, respectively, approaching the theoretical limit. The high elastic limit enables BMGs to store large elastic energy and be applied in sports equipment, such as golf club heads, baseball bats, tennis racquets, bicycle parts, fishing equipment and marine applications [28]. The high strength and hardness also make it possible for these materials to be employed in medical surgery and aerospace coatings. Considering the rapid development of fundamental and applied research on metallic glasses, it is expected that these materials will become more significant in the near future. The possible application field for BMGs are summarized in **Table 1.2** [29].

Table 1.2 Application fields that currently have been proceeded for BMGs, adapted from [29].

-
1. Structural
 2. Sensor
 3. Precision machinery
 4. Optical
 5. Ornamental
 6. Spring
 7. Sporting goods
 8. Wear-resistant coating
 9. Precision nozzle
 10. Corrosion-resistant
 11. Magnetic
 12. Micro-technology
 13. Nano-technology
 14. Information data storage
 15. Biomedical
 16. Medical instrument
 17. Fuel-cell separator
-

Advantages: net-shape processing, viscous flow forming processing.

1.2 Deformation mechanisms of BMGs

1.2.1 Deformation map

Deformation maps, which was firstly introduced by Ashby in 1972, were maps which display the field of stress and temperature in which a particular mechanism of plastic flow is dominant [30]. A point on the map then identifies the dominant mechanism and indicates the resulting strain-rate. This concept of deformation map was firstly introduced to metallic glasses by Spaepen in 1977 [31]. Based on his free volume model, Spaepen proposed that there are two modes of deformation for BMGs depending on strain rate, applied shear stress and temperature (**Figure 1.2**).

The first mode is homogeneous deformation, in which bulk metallic glass deforms at relatively high temperature (in or near the supercooled liquid regime) and low strain rate, and each element of bulk metallic glass is able to contribute to the deformation. The homogenous flow of metallic glass is intimately related to shape-forming applications [32-41], and for this reason it has been investigated extensively. Homogeneous flow was also observed to occur below glass transition temperature at high strain rate. By conducting nanoindentation experiment over different strain rate and a wide range of

temperature, Schuh et al. [42] demonstrated that homogeneous deformation of metallic glass can occur even below glass transition temperature when deformation rates exceed the characteristic rate for shear band nucleation.

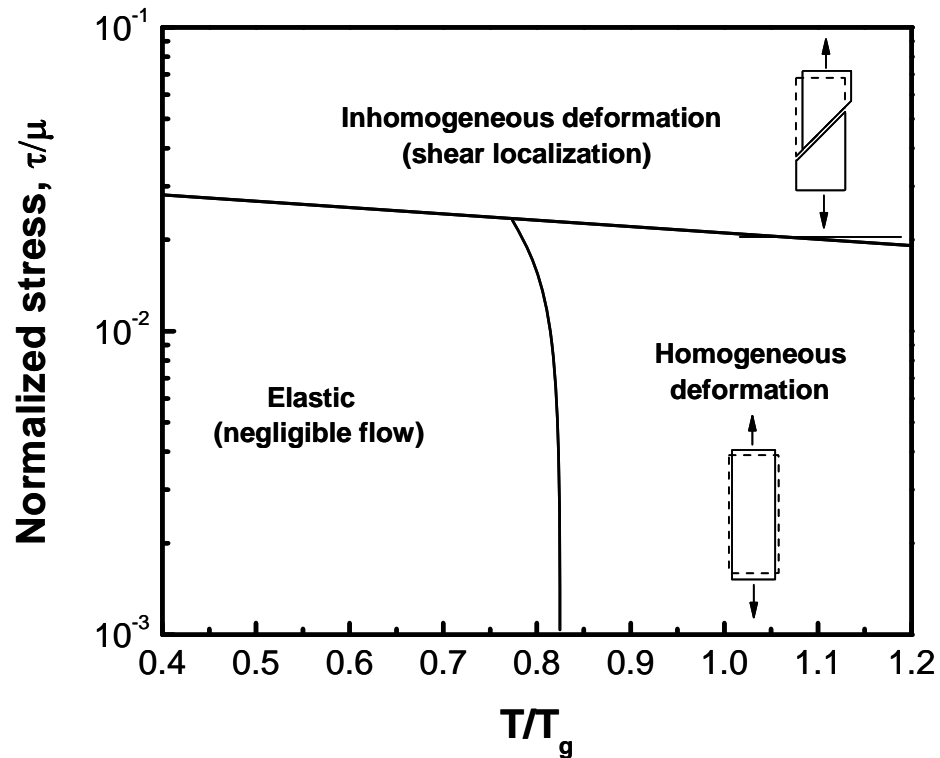


Figure 1.2 Schematic deformation map for an amorphous metal illustrating the temperature and stress regions for homogeneous and inhomogeneous plastic flow, adapted from [31].

The second mode is inhomogeneous deformation, in which bulk metallic glass deforms at relatively low temperature ($\leq 0.7T_g$) and high strain rate. Deformation occurs in localization processes, in which highly localized, discrete, and thin shear bands are formed, leaving the rest of the material plastically undeformed. Upon yielding, metallic glasses often show serrated plastic flow without work hardening, tending to exhibit work softening which

leads to shear localization. The deformation map was later revisited by Argon [43, 44]. Recently, Lu [45] and Schuh [42] updated this map in terms of bulk metallic glass instead of amorphous ribbons.

While homogeneous deformation can be well described by rheological models that average the operation of many local atomic-scale events, the process of inhomogeneous deformation of metallic glasses is still lack of in-depth understanding. However, the inhomogeneous deformation of shear bands has important practical consequences for the strength, ductility, toughness and eventual application of metallic glasses.

1.2.2 Deformation models

Although extensive studies have been carried out on the macroscopic mechanical behavior of BMGs, a deep understanding on the microscopic deformation mechanism in these amorphous metals is still far from comprehensive. It is generally accepted that upon yielding, shear localization occur and lead to a sharp viscosity drop within shear bands. However, it is still under debate as to why the viscosity within shear bands drops. There are two major hypotheses to account for shear localization or strain softening. One hypothesis is that during plastic deformation, stress induced dilatation

(volume expansion) causes the density decreases within shear bands and thus minimizes their resistance to deformation. The other hypothesis is that temperature rise (thermal expansion) takes place during plastic deformation, and the temperature rise is beyond the glass transition temperature or even beyond the melting point, and thus decreasing the viscosity by several orders of magnitude. The two most acknowledged deformation mechanisms based on volume expansion hypothesis for BMGs are the 'free volume' model [31, 46, 47] and the 'shear transformation zone' (STZ) model [43, 48, 49], as illustrated with the two-dimensional schematics in **Figure 1.3** (a) and (b), respectively. Another model based on the thermal expansion hypothesis is heat evolution model [50-52]. All these three models will be reviewed in next section.

1.2.2.1 Free volume model

The concept of 'free volume', which refers to the fraction of matter having a lower atomic coordination than that in a reference material having a dense random packing, was firstly introduced to amorphous metals by Cohen and Turnbull in 1959 [46]. The initial free volume in metallic glass is fixed when the super cooled liquid solidifies at the glass transition temperature. Such concept was subsequently adopted by Spaepen [31], and a 'free volume' model to describe the deformation mechanism for metallic glasses was proposed.

Spapen considered that the deformation process for metallic glasses is a competition between two processes: creation of free volume by the applied shear stress and annihilation of extra free volume by structural rearrangement. At a sufficiently high stress, an atom with hard sphere volume can overcome the energy barrier and be squeezed into its neighbor with a small volume, creating a certain amount of extra volume, as shown in **Figure 1.3 (a)**. Competing with this is a relaxation process, which tends to annihilate the excess free volume and restore the system to its initial structural state by series of diffusional atomic jumps.

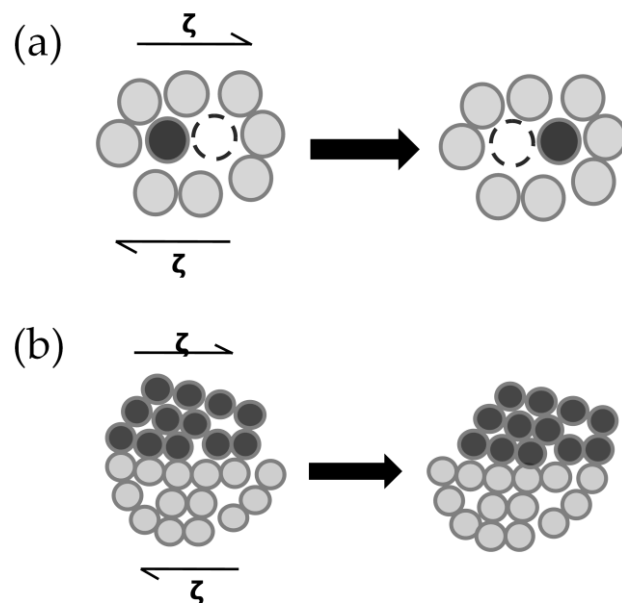


Figure 1.3 Two-dimensional schematics of the atomistic deformation mechanisms proposed for amorphous metals (a) free volume model (b) shear transformation zone model, reproduced from [53].

Based on this model, the homogeneous deformation behavior [45, 54, 55] and some aspects of the inhomogeneous deformation behavior [56-59] in BMG can be explained. However, one should be cautious to use this model as it does not describe the exact motion and rearrangement of constitute atoms within shear bands. In addition, series of recent studies, including computer simulations, creep test and high temperature nano-indentation test [60-64], have shown that the deformation process of metallic glasses involves a collective motion of a cluster of atoms rather than a single atomic jump.

1.2.2.2 Shear transformation zone (STZ) model

Based on an atomic-analog bubble-raft model, Argon and Kuo [48] proposed a 'shear transformation zone' model to explain the deformation mechanism in metallic glasses. The shear transformation zone is essentially a local cluster of atoms that undergoes an inelastic shear distortion from one relatively low energy configuration to a second such configuration, crossing an activated configuration of higher energy and volume. Unlike Spapen's free volume model which attributes the plastic flow to a single atomic jump, STZ model considers a cluster of localized atoms as the plastic flow unit. Upon loading, such STZs can spontaneously flow along the activation path and accommodate strain, resulting in local softening at ambient temperature. The

STZ model has also been successfully applied to explain the steady state deformation behavior of BMGs [65, 66].

Since the original analog model of Argon et al. [43, 48, 67], more sophisticated computer models have been developed to study glass deformation in both two and three dimensions [49, 61, 68-71]. These results suggest that STZs are common to deformation of all amorphous metals, although details of the structure, size and energy scales of STZs may vary from one glass to the next.

The major difference for these two models is the fundamental unit event to accommodate the shear strain: in STZ model it is a collective motion of a cluster of atoms whereas in free volume model it is a more highly localized atomic jump. Although differences between the 'free-volume' model and 'STZs' model, these two models share many common features on the atomic level, which are very important to understand the macroscopic deformation behavior of metallic glasses: (1) both mechanisms consist of a two-step system; forward jumps or STZ operations compete with backward ones, which can occur simultaneously at the same spatial positions. (2) both mechanism are thermally activated and exhibit similar energy scales. (3) both mechanisms are dilatational.

1.2.2.3 Heat evolution

There has been considerable debate as to whether viscosity drop within shear bands is due to shear induced disordering (dilatation) or to thermal effects. Principally different from the 'free volume' model and 'shear transformation zone' model, the heat evolution model consider that almost all of the work done on the sample in , plastic deformation for metallic glasses is dissipated as heat. If the deformation is heavily concentrated in a few bands, one can expect a substantial increase in temperature (as high as glass transition temperature or even melting temperature) and a corresponding drop in viscosity.

It was firstly proposed by Leamy and co-workers [50] that the shear banding events are essentially adiabatic phenomena, but was quickly doubted by other researcher [72] on the grounds that rapid thermal conduction may limit the temperature rise in a thin shear band. One approach to prove confirmative evidence on the temperature rise is to measure the temperature directly inside a shear band. However, as the shear bands are thin, move fast and are short-lived, it is very challenged to measure this temperature rise directly. Although infrared measurements clearly show temperature rises, the poor spatial and temporal resolution would not determine the temperature evolution in the band.

Recently, Lewandowski and Greer [73] invented a smart and simple way to improve the resolution. They coated a Zr-based bulk metallic glass sample with a thin layer of tin, and found that after deformation, the tin near the shear bands had beaded up as it had melted. Their method has unprecedented resolution: 30 ps (the thermal diffusion time through the coating) and 100 nm (the scale of the bead pattern), respectively. It allows them to estimate the temperature rise, which, depending on the duration of the shear, may be several thousand degrees. By making a lower estimation on the shear band propagation time, Lewandowski and Greer further illustrate that the shear bands cannot be fully adiabatic.

1.3 Mechanical behavior of BMGs at room temperature

1.3.1 Yield criteria

The deformation and fracture behavior of several structural materials, such as metals, ceramics, concrete, rocks, etc, have been studied for more than 200 years, and many theories and criteria have been proposed and developed. For example, for polycrystalline metals, the fundamental carrier of plastic deformation is the motion of an individual dislocation. Slip deformation can

proceed only on some low index crystallographic planes, such as $\{111\}$ planes in fcc metals or $\{0001\}$ planes in hcp metals. Two well-known criteria that are commonly used are those of Tresca and von Mises, the latter of which matches well with experiment data for a variety of metals and alloys [74]. An important characteristic of these yield criteria is their symmetry, predicting the same value of yield stress either in tension or compression. However, several studies have shown that MGs exhibit asymmetric yield behavior [75, 76], and suggested that MGs have fundamentally different deformation mechanism compared with polycrystalline metals.

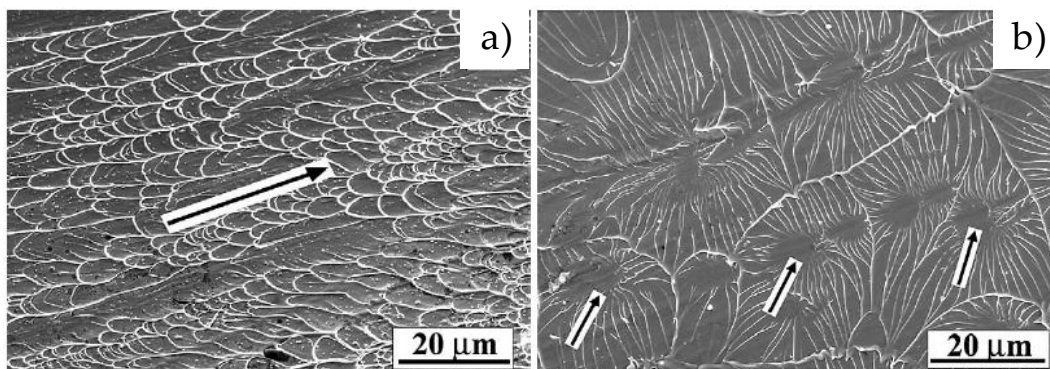


Figure 1.4 Comparison of typical fracture surfaces of $Zr_{59}Cu_{20}Al_{10}Ni_8Ti_3$ metallic glassy specimens induced by a) compressive loading and b) tensile loading, adapted from [75].

For example, it was demonstrated by Zhang et al. that the yield stress in compression is higher than that observed in tension for the same Zr-based BMG samples [75]. Meanwhile, the main feature of the fracture morphology for compressive samples is 'vein pattern', whereas those for the tensile samples are cores and radiating vein like patterns (seen in **Figure 1.4**). In

addition, the fracture angle with respect to the load direction is different between tension and compression. Many investigations have shown that the compressive fracture angle (denoted as θ_c) is smaller than 45° [77-81], while the tensile fracture angle (denoted as θ_T) is larger than 45° [44, 52, 65, 75, 77, 81-91], covering several different alloy systems such as Zr-, Cu-, Ti-, Fe-, Co-, La-, Al-, Ni-, Pd-based alloys.

The Mohr-Coulomb criterion was proposed in 1773, and it has been suggested as an alternative form that the shear failure depends not only on the shear stress, but also on the normal stress:

$$\tau_y = \tau_0 - \alpha\sigma_n \quad (1.1)$$

Where τ_y is the effective shear stress at which yielding occurs, τ_0 is a constant, α is a system-specific coefficient that controls the strength of the normal stress effect, and σ_n is the applied stress normal to the shear plane. The Mohr-Coulomb criterion was originally proposed for granular materials, but may also apply to amorphous metals as the relative motion of randomly packed atoms in a metallic glass is comparable to that of randomly packed particles in a granular solid. Using a fundamental model of shear atomic shuffles, Schuh and Lund [92] found that simulated amorphous metals plastically yield in a manner consistent with the Mohr-Coulomb criterion. The result agrees well with another simulation work [93] and a variety of independent experimental data [79, 94]. They also proposed that future studies on MGs should be

conducted within the frame work of such a pressure- or normal stress-dependent yield criterion, and indicated that MGs are uniformly weaker in tension than they are in compression.

1.3.2 Plasticity

In the absence of structural defects such as dislocations and grain boundaries in crystalline materials, bulk metallic glasses (BMGs) exhibit unique mechanical properties, such as high strength and high elastic strain (about 2%). Therefore, BMGs are promising materials for engineering applications. However, due to the lack of macroscopic plasticity, the application of BMGs as structural materials is hindered. Generally speaking, plastic strain in metallic glasses is accommodated by highly localized narrow bands (~10 nm in thickness) [95], which are named shear bands. Once shear bands are operated under applied shear stress, a sharp drop in viscosity in these bands occurs, resulting in catastrophic failure without any considerable macroscopic plasticity.

During the past decade, extensive studies have been conducted on the improvement of plasticity for BMGs under compression. Schroers and Johnson [96] reported that 20% plasticity was achieved in a Pt-based BMG

under compression, and they correlated the extraordinary room temperature plasticity with a high value of Poisson ratio ($\nu=0.41$). Starting from a $Zr_{65}Cu_{15}Ni_{10}Al_{10}$ metallic glass and subsequently maximizing Poisson ratio, Liu et al. [97] found a series of BMGs can sustain large compressive strain without fracture. Recently, several studies have reported that plasticity can be affected by extrinsic factors (sample geometry, confinement, and machine stiffness). For example, it was reported by Han et al. [98] that the stiffness of a testing machine can influence the stability of shear bands and further the plastic deformation of BMGs. A parameter called shear band instability index (SBI), which is proportional to sample size and inversely proportional to machine stiffness, was proposed to govern the plastic deformation.

However, characterization on mechanical properties of BMGs by compression may suffer from two major drawbacks. The first major drawback associated with compression test is the small dimension of specimen that is compressed between the two parallel platens. The friction and stress non-uniformity caused by the nonparallel surface between the specimen and the platens can significantly change the stress-strain response, resulting in artificial compressive plasticity. In addition, the influence of constraint, sample alignment, lubrication, sample size, sample aspect ratio and the stiffness of the testing machine can significantly affect the plasticity of BMGs[59, 98-103]. The other major drawback is the asymmetrical mechanical

response of BMGs under tension and compression. Although significant enhancement on the plasticity under compression is revealed, negligible ductility (less than 0.5 %) is exhibited for BMGs under tension. This is most likely because both mode *I* (tensile mode) and mode *II* (shear mode) instability have been created in tension, whereas only mode *I* instability is produced in compression. Therefore, compressive plasticity may magnify the performance of BMGs under loading bearing condition, which is extremely dangerous for engineering applications. It is highly desired to enhance the ductility of BMGs under tensile condition.

Fortunately, several works have been carried out on improving tensile ductility of metallic glasses at small scales. For example, Guo et al. [104] reported large tensile ductility as high as 45 % of a monolithic metallic glass, with dimension of the order of 100 nm. The small samples were prepared by focused ion beam (FIB) micromachining technique, and subsequently tested during the in situ TEM experiment. The results clearly illustrated that homogeneous deformation or even necking can occur in small size metallic glasses (as seen in **Figure 1.5**). This behavior is similar to that of their crystalline counterparts. Similarly, superelongation behavior was observed in a $\text{Al}_{90}\text{Fe}_5\text{Ce}_5$ metallic glass when the dimension was smaller than 20 nm [105]. Remarkably, a superelongation up to 200 % was found, and even an atomic chain was formed after necking. These observations strongly suggest 'size

effect' in the mechanical properties of metallic glasses, i.e., small volume metallic glasses can deform via homogeneous or inhomogeneous flow without catastrophic failure.

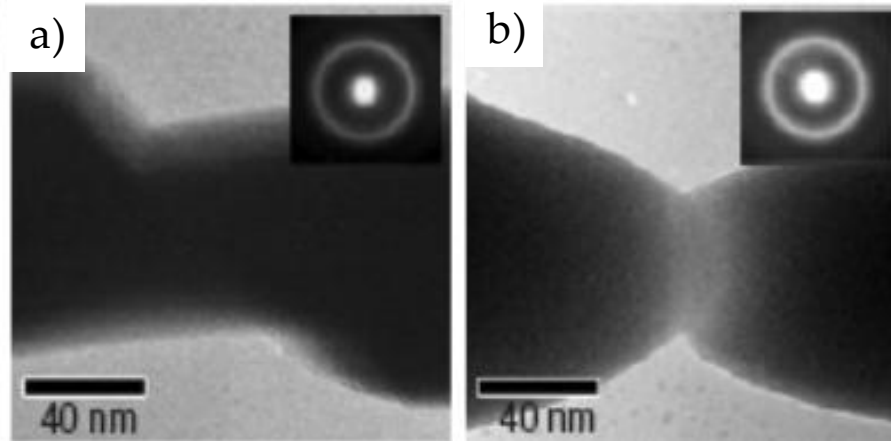


Figure 1.5 TEM bright-field images of in situ tested Zr-based monolithic MG samples with a gauge dimension of about $100 \times 100 \times 250 \text{ nm}^3$, showing a) necking, and b) stable shear, adapted from [104].

Besides achieving tensile ductility at small scales, another common approach of improving the tensile ductility is to introduce a second phase into the glass matrix to form bulk metallic glass matrix composites (BMGMCs) [22, 65, 106-115]. Recently, Hofmann et al. [115] reported a 'designed composites' by matching fundamental mechanical and microstructural length scale. These titanium-zirconium-based BMG composites exhibit tensile ductility up to 10 %, yield strengths of 1.2-1.5 GPa, K_{Ic} as high as $170 \text{ MPa m}^{1/2}$, and fracture energies for crack propagation to $G_{Ic} = 340 \text{ KJ m}^{-2}$. The stress-strain curve and fracture morphology of the BMG composite is shown in **Figure 1.6** and **Figure**

1.7, respectively. These extraordinary properties put BMG composites among the toughest known materials in an 'Ashby plot'.

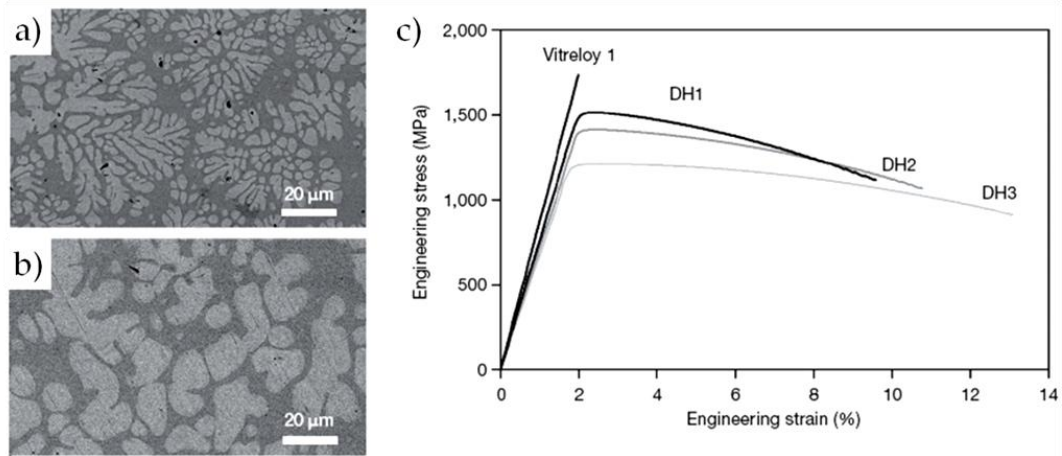


Figure 1.6 SEM micrographs showing the microstructure of the BMG matrix composites labeled as a) DH1 and b) DH3 where the dark contrast is from the glass matrix and the light contrast is from the dendrites. c) The corresponding tensile engineering stress-strain curves of composites DH1 and DH3, together with the curves of another composite DH2 and a monolithic BMG (Vitreloy 1), adapted from [115].

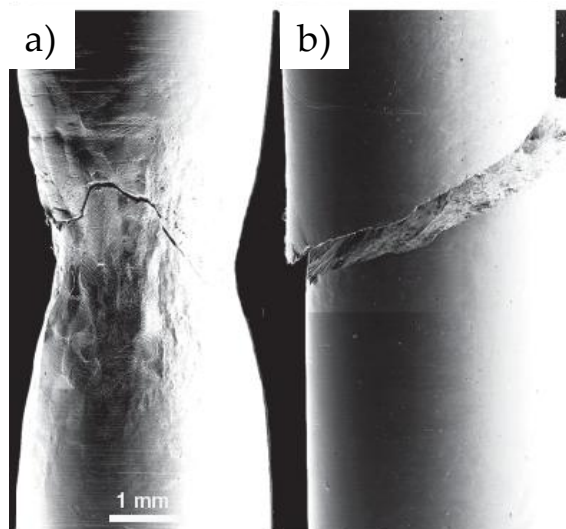


Figure 1.7 a) The SEM micrograph of necking in $Zr_{39.6}Ti_{33.9}Nb_{7.6}Cu_{6.4}Be_{12.5}$ BMG matrix composites, and b) Brittle fracture representative of all monolithic BMGs, adapted from [115].

Very recently, a BMG composite with work hardening capability was reported by Wu et al. [116]. Unlike the conventional BMGs or BMGMCs which are strain-softening during deformation, this new BMG composite exhibits large tensile ductility up to 7% with significant strain hardening ability (as shown in **Figure 1.8**). The authors attributed the hardening mechanism of this composite to the martensitic transformation of the crystalline phase during tensile deformation.

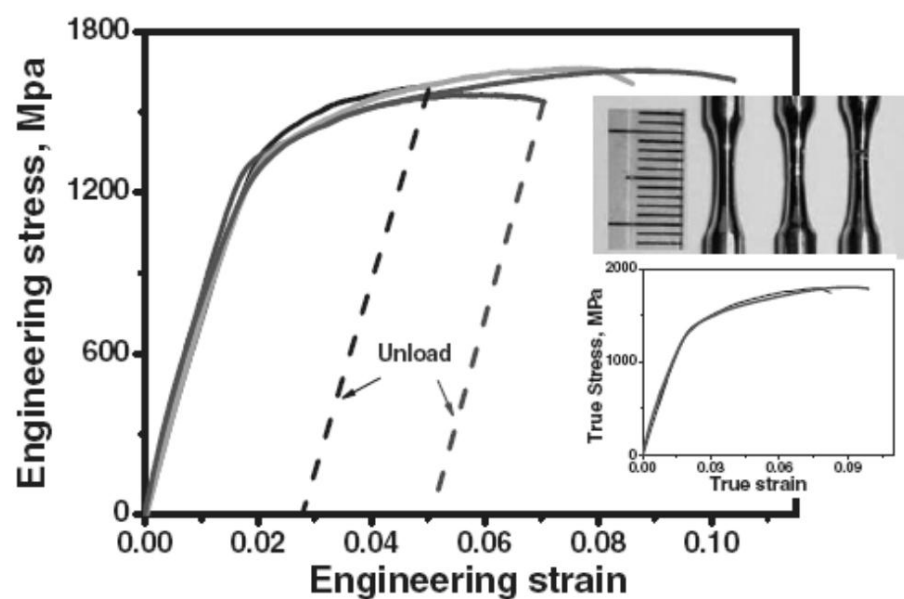


Figure 1.8 Engineering tensile stress–strain curves of the BMG composites. Dashed lines indicate the unloading process. Top inset shows the outer appearance of the tensile samples pre-strained at the different stages and the lower inset shows the true tensile stress–strain curves, indicating a significant strain-hardening behavior, adapted from [116].

Although continuous progress has been made on the compressive/tensile plasticity, there is only limited work on tensile ductility of monolithic bulk metallic glasses. Therefore, it is of crucial importance for studying mechanical behavior of BMGs under tension, both for a better understanding of the fundamental plastic mechanism and for supporting the application of BMGs as practical engineering materials.

1.3.3 Mechanical behavior under confinement condition

Most Engineering applications require a minimum level of damage tolerance (plasticity, toughness) under complicated loading conditions. As such, it is also important to study the mechanical behavior of BMGs under confinement condition. Several studies have shown that compressive plasticity can be enhanced under confinement condition [103, 117, 118].

For example, Bei et al. [103] demonstrated that compressive strain as high as 80% was obtained by reducing the aspect ratio of the testing sample. The researchers also reported a strain-induced softening phenomenon in contrast with a strain hardening as in crystalline metals. Profuse shear banding was observed and shear-induced local dilatation may be the source of the deformation-induced softening. The hardness as a function of plastic strain

can be seen in **Figure 1.9**. The hardness profile shows a clear decreasing trend as the plastic strain increasing. It is also reported by Han et al. [98] that the compressive plasticity can be enhanced for the sample with aspect ratio 1:1 by controlling the stiffness of the testing machine. Up to date, however, there is no report on the enhancement of tensile ductility for BMGs under confinement condition.

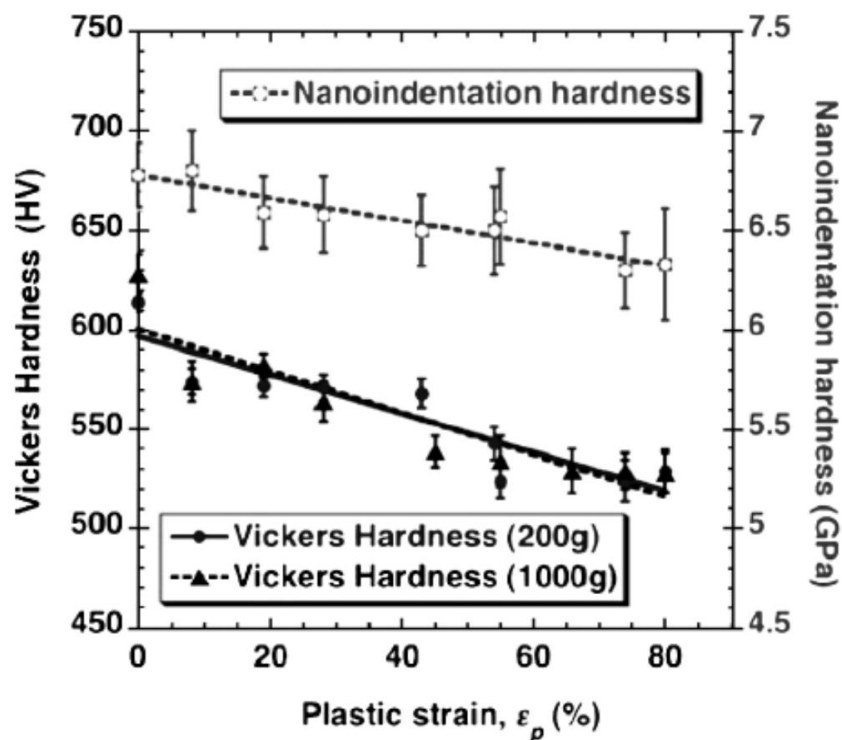


Figure 1.9 Decrease in hardness (nanoindentation and Vickers at two different loads) with increasing plastic strain, adapted from [103].

1.4 Objective and outline of this thesis

Despite abundant work has been carried out on the mechanical behavior of BMGs under compression [53], there is limited work on the tensile behavior of monolithic bulk metallic glasses. In addition, characterization on mechanical properties of BMGs by compression may exaggerate the performance of BMGs under loading bearing condition due to the asymmetrical mechanical response of BMGs under tension and compression. Thus, there is a compelling demand for research studying the mechanical behavior of BMGs under tension, both for a better understanding of the fundamental mechanism and for supporting the application of BMGs as practical engineering materials.

The objective of this thesis is to explore the mechanical behavior of BMGs with a variety of sample geometries under tensile confinement condition, providing in-depth understandings on the strength, ductility and fracture of metallic glasses. It was revealed that BMGs exhibit radically different mechanical behavior under tensile confinement condition as compared to that of uniaxial tensile condition. These findings provide insightful understanding on the fundamental deformation mechanisms of BMGs, and may pave the way for their engineering applications.

There are totally six chapters in this thesis.

In **Chapter 1** (this chapter), the background knowledge associated with metallic glass was firstly introduced. Subsequently, the progress on mechanical behavior of BMGs achieved so far was briefly reviewed. Finally, the objective and outline of this thesis was presented herein.

In **Chapter 2**, the alloy preparation, structure characterization, thermal and mechanical testing methods are presented. In **Chapter 3**, the plastic deformation behavior of BMGs under tensile confinement condition is studied. It is revealed that large tensile ductility and homogeneous deformation can be achieved. The mechanism for room temperature homogeneous flow is also discussed.

In **Chapter 4**, the strength and fracture of BMGs under tensile confinement is systematically investigated. It is revealed that the tensile strength is approaching the theoretical strength, placing BMGs among the strongest materials known so far. The fracture morphology for BMGs under tensile confinement condition is also discussed.

In **Chapter 5**, tensile stress induced strain hardening and densification are studied. For the first time, a 'straining hardening' phenomenon for bulk metallic glass is discovered. The mechanism of this phenomenon is attributed to the densification of structure during plastic deformation. In **Chapter 6**, the

results of this thesis are summarized and the topics for future research are suggested.

Chapter 2

2 Experimental Procedures

2.1 Alloy preparation

The alloy with a nominal composition of $\text{Zr}_{64.13}\text{Cu}_{15.75}\text{Ni}_{10.12}\text{Al}_{10}$ was selected for the study of this thesis. This alloy was reported to have a good glass forming ability up to 5 mm in cylindrical rod, and high compressive plasticity at ambient temperature [97]. The ingot was prepared by arc-melting mixtures of high purity metals in a Ti-gettered high-purity argon atmosphere. Each ingot was remelted at least five times to ensure the chemical homogeneity of the alloy. The rods with diameters larger than 4 mm were prepared by directly casting the melt into water-cooled copper mold (4 mm or 5mm in diameter, 75 mm in length). The rods with diameters smaller than 4

mm were prepared by remelt the ingot in a small arc-melter and cast the melt into rods by water-cooled copper mold (1mm, 2mm, or 3mm in diameter, 30 mm in length) suction casting.



Figure 2.1 Optical image of the arc-melting furnace with a cylindrical copper mold of 5 mm in diameter.

2.2 Structure characterization

To characterize the amorphous nature of the alloy, the longitudinal cross-section of the rods was examined by X-ray diffraction (XRD) employing a Bruker AXS (D8 ADVANCE) instrument with Cu-K α radiation at 40 KV. Differential scanning calorimetry (DSC, 2920 TA instruments) experiment was

taken at a heating rate of 0.33 Ks^{-1} to measure the thermal properties of the as-cast and deformed samples. **Figure 2.2** shows the XRD pattern of a as-cast 5 mm rod sample. No crystalline peak is found, confirming the amorphous nature at the XRD resolution. Clear glass transition and sharp crystallization events are observed in the DSC trace as shown in **Figure 2.3**, further confirming the alloy is fully amorphous.

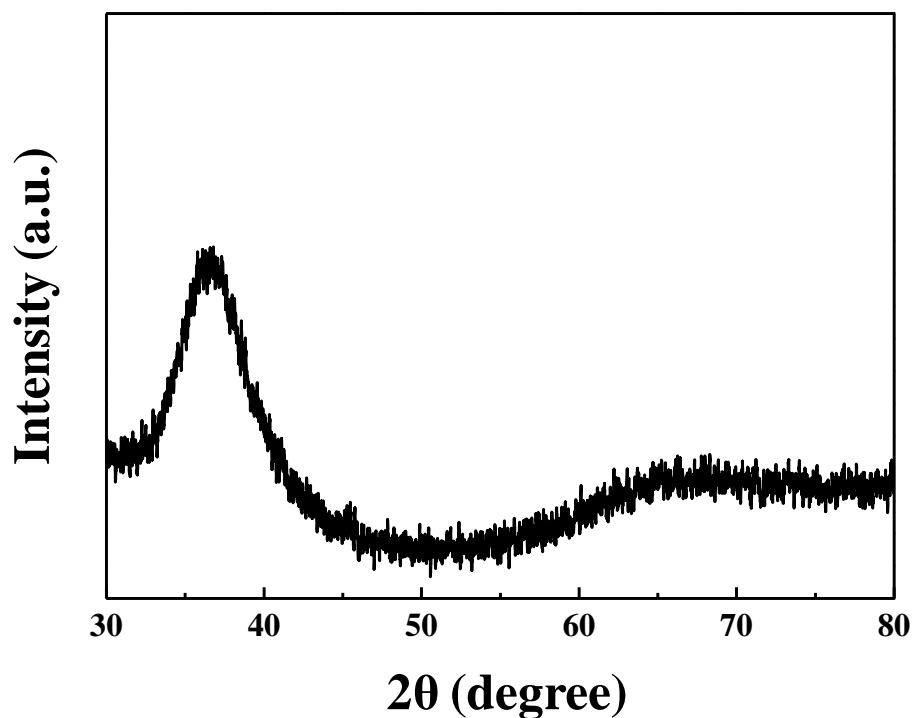


Figure 2.2 XRD pattern of the as-cast $\text{Zr}_{64.13}\text{Cu}_{15.75}\text{Ni}_{10.12}\text{Al}_{10}$ rod with a diameter of 5 mm.

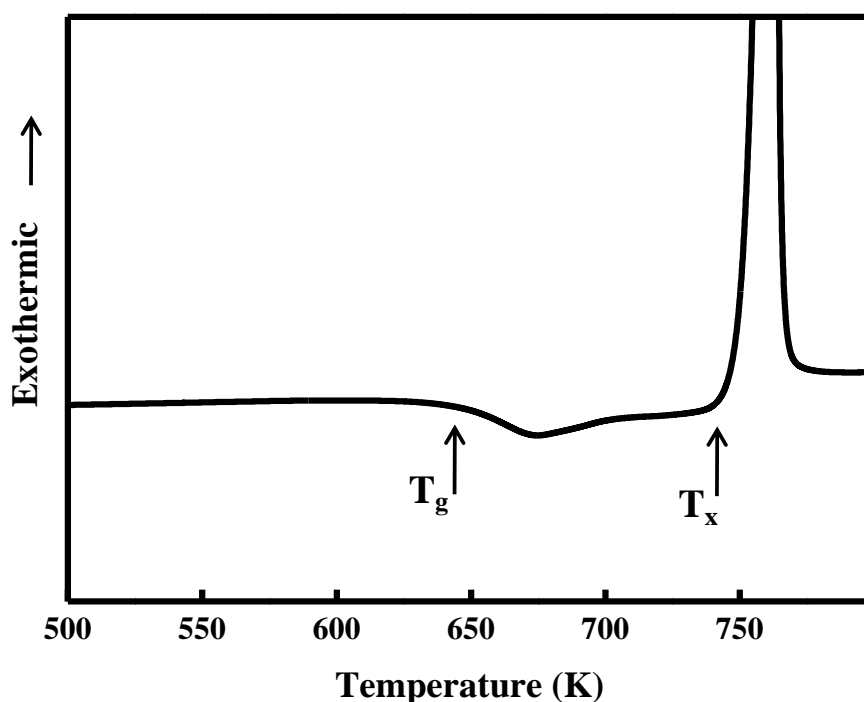


Figure 2.3 DSC trace of the as-cast $Zr_{64.13}Cu_{15.75}Ni_{10.12}Al_{10}$ rod with a diameter of 5 mm., showing the glass transition temperature (T_g) and onset of crystallization temperature (T_x).

The morphology of the sample was examined by scanning electron microscopy (SEM, Philips XL30 FEG instruments). To further study the structure of the alloy, transmission electron microscopy (TEM, JEM, 2010F) with an accelerating of 100 KV was utilized. The TEM samples was firstly polished to the thickness about 20 μm by sandpaper, and subsequently thinned by ion milling. To avoid the artifact induced by ion milling [119-122], the ion beam energy was set to be 3.5 KeV and a glazing angle of 8° , respectively. Samples were finally cleaned at a lower angle of 4° for 5 minutes. Bright field (BF) and dark field (DF) images as well as selected-area electron

diffraction patterns (SADP) were taken to examine the amorphous nature of the samples.

2.3 Thermal testing

Low temperature annealing, also known as structural relaxation was carried out to take the quenched glass approaching the equilibrium glassy state by annihilation of the excess free volume. To avoid any possible crystallization, the annealing treatments were conducted for 30 min at temperature of 473K, 523K and 573 K, respectively (which are all lower than their glass transition temperatures, T_g). To prevent oxidation, the annealing was performed in a furnace after placing the samples inside a vacuum-sealed silicate tube. The thermal properties were measured by differential scanning calorimetry (DSC) at a heating rate of 0.33 Ks⁻¹.

2.4 Mechanical testing

2.4.1 Uniaxial compression

Uniaxial compression testing was performed at room temperature with a constant strain rate of 10^{-4} s^{-1} , using the LLOYD (model EZ50) universal materials testing machine. The compression specimens were first sectioned from the cast rods using a Struers diamond cutter, followed by a grinding process with a customized specimen jig to carefully grind the sample into “orthogonal” shape. This sample preparation process not only ensures parallelism of two ends of the specimen, but also guarantees that the ends were exactly perpendicular to the longitudinal axis of the specimen. This process is extremely important to the mechanical tests of BMG samples as described in Ref. [123]. The compression samples were sandwiched between two WC (tungsten carbide) bearing blocks and their ends were lubricated by Black MOLY (molybdenum disulfide in premium grease). Each sample was carefully centered on the loading axis to ensure uniaxial loading, and true applied strains were calculated from the crosshead displacement after correction for machine stiffness. The machine stiffness was determined by compressing the two WC bearing blocks without sample centering in.

2.4.2 Tensile testing

The tensile confinement condition was created by fabricating the tensile samples into various geometries with a customer designed machine. In this

thesis, four series of tensile confinement samples were studied. In series *one*, the bars were processed into circumferentially notched round samples with a notch angle (α) of 120°, 90° and 45°, respectively. In series *two*, the slit notched samples were altered by changing their aspect ratios. In series *three*, the rectangularly-notched bar samples were fabricated with width 1.6 mm and height 0.5 mm. In series *four*, a 5 mm rod with a Bridgman notch with aspect ratio of 0.19 was used. The detailed geometries and dimensions for the various confined tensile samples were illustrated in **Figure 2.4**.

Before tensile test, the samples were initially polished by sand paper and followed by fine polishing with Al₂O₃ suspension. The tensile samples were then clamped at the ends and attached to the load frame. Tensile tests were carried out using an electro-servo-hydraulic system (Instron 8521 machine) with a maximum load of 100 KN at a cross head speed of 0.02 mm/min, corresponding to a constant engineering strain rate of 10⁻⁴ s⁻¹. To measure the elongation of the notch, an extensometer was attached across the notch and the elongation was monitored. The force-extension raw data was recorded to calculate the stress-strain curve.

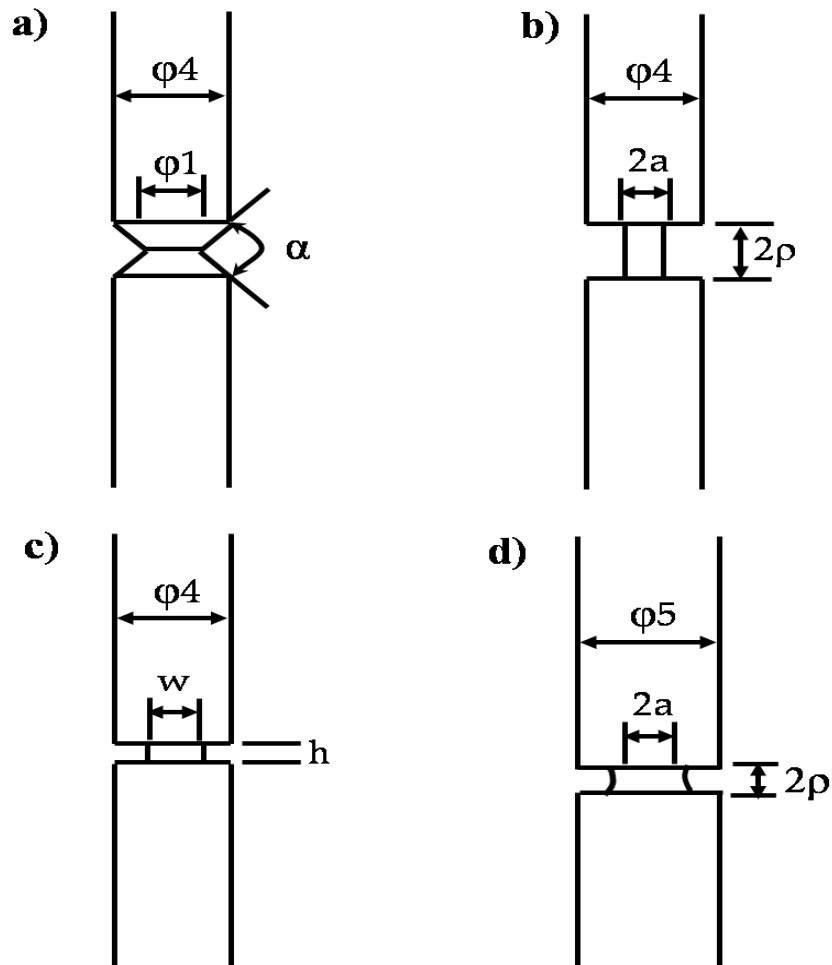


Figure 2.4 Schematic illustration of the confined tensile bars used in this study: a) circumferentially-notched round samples with a notch angle α of 120° , 90° and 45° , respectively, b) slit-notched samples with aspect ratios (a/ρ) of 2, 1 and 0.5, respectively, c) rectangularly-notched samples with width 2.0 mm and height 0.5 mm, d) a 5 mm rod with a fixed aspect ratio of 0.19 ($a=2.6$ mm, $\rho=0.5$ mm).

2.4.3 Micro-hardness testing

A microhardness tester (Buehler, miromet 2103) with a pyramid indenter was used for microhardness measurement. The samples for microhardness

measurement were prepared by polishing the longitudinal cross-section of the cylindrical shaped sample with sandpaper, followed by fine polishing with Al_2O_3 suspension. Microhardness measurement was made along the middle line of the sample with a maximum load of 50 g and a dwell time of 10 s. The Vickers hardness was calculated from the length of the indentation diagonal measured by an optical microscope of 100 magnification.

Chapter 3

3 Achieving tensile ductility of BMGs at room temperature

3.1 Introduction

Bulk metallic glasses (BMGs) are superior to their crystalline counterparts as they exhibit an extraordinary combination of high strength and high elastic limit, and considered to be a promising engineering material [4, 23, 29]. However, the Achilles heel of BMGs is that they lack of plasticity at room temperature. It is generally believed that strain highly localized in a narrow shear band during deformation, and catastrophic fracture occurs along one dominant shear band without macroscopic plasticity.

Progresses have been made over the past years to improve plasticity of BMGs at room temperature [53]. Different explanations have been given for reasons contributing to the plasticity of BMGs, such as large Poisson ratio ν [96, 124, 125], nanocrystallization during deformation [126, 127], phase separation [128-132] and geometries of the testing specimen [103]. For example, Schroers and Johnson [96] purposed that a Pt-based BMG exhibit large compressive plasticity as a consequence of large Poisson ratio ($\nu=0.41$), which blocks the cracks nucleation and propagation. On the other hand, Bei et al. [103] reported that large compressive plasticity can be achieved when reducing the aspect ratio of the specimen by formation of multiple, intersecting shear bands.

However, without exception, BMGs exhibit negligible macroscopic tensile ductility at room temperature. For example, Yokoyama et al. [133] demonstrated that a hypoeutectic Zr-Ni-Cu-Al BMG shows a tensile ductility of about 1.7% at room temperature. They attributed the tensile ductility to the modifications of glass structure with increase in the number of Zr-Zr atomic pairs in the hypoeutectic composition. On the other hand, some researchers have shown that tensile ductility can be achieved in small samples (sub-micrometer scale) [104, 134-136]. These small samples show a transition of reduced shear banding propensity to increased homogeneous flow. There is still intense debate as to why small samples show this transition from

localization of shear banding to homogeneous deformation without formation of shear bands. Up to date, the report on the enhancement of tensile ductility for BMGs is yet available.

For BMGs under tension, the specimen fails along one dominant single shear plane. The resolved normal stress σ and shear stress τ on the shear plane of angle θ can be expressed as,

$$\sigma = \frac{P}{A} \sin \theta \sin \theta \quad (3.1)$$

$$\tau = \frac{P}{A} \sin \theta \cos \theta \quad (3.2)$$

where P is the applied load, A is the cross sectional area, θ is the angle with respect to the loading direction. **Figure 3.1** shows the variation of shear stress with the angle between shear plane and stress axis. It can be seen that when $\theta=45^\circ$, the shear stress reaches its maximum and shear banding on the plane becomes catastrophic and fracture occurs along this plane.. This is the most possible explanation that why most BMGs preferentially fracture along 45° shear plane [52, 137]. Although the resolved normal stress also plays a role in the fracture process [138], the key factor that governs the failure is commonly believed to be shear stress. The shear stress decreases when θ deviates from 45° . When the resolved shear stress on shear plane A_1 (indicated in **Figure 3.1**)

reaches τ_c (the critical shear stress, which is a material constant depending on the alloy system), the resolved shear stress on shear plane A_2 (indicated in **Figure 3.1**) is smaller than the critical value.

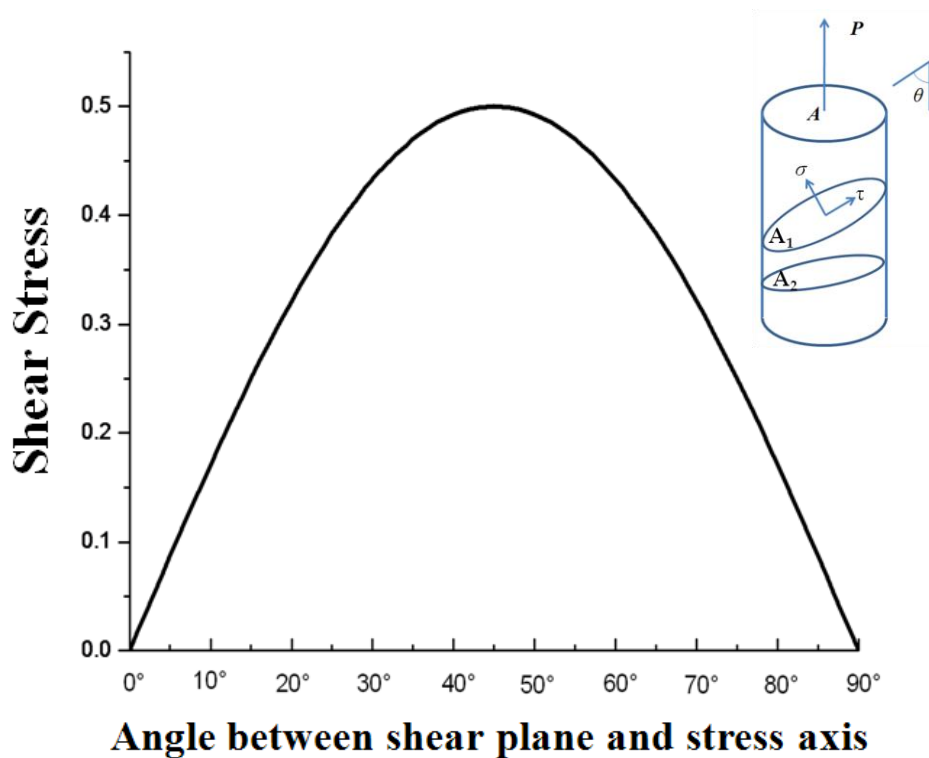


Figure 3.1 Variation of shear stress with the angle between shear plane and stress axis. The inset shows the resolved tensile stress σ and shear stress τ in the shear plane of angle θ .

Based on the above analysis and equations (3.1) and (3.2), one could expect that if the area of the shear plane of the tensile specimen can be properly controlled (for example, decreasing A_2), the resolved shear stress on specific plane will be lower than the critical shear stress whereas the tensile

stress will be dominant. As such, shear banding instability in tension may be suppressed or delayed, and it would be very interesting to see how BMG behaves at room temperature without shear banding. In this chapter, through designing of various tensile confinement specimens, we show that large tensile ductility can be achieved at room temperature. The possible reason for room temperature ductility of BMGs is also presented.

3.2 Results

3.2.1 Deformation behavior of circumferentially-notched samples

Figure 3.2 shows the optical image of the fabricated circumferentially-notched samples with angles of 120° , 90° and 45° , respectively. These samples were fabricated from 4 mm rods, which were produced by chill cast technique as described in **Chapter 2**. The minimum part of each circumferentially-notched sample is about 1 mm in diameter, and is carefully calibrated by SEM before tensile test. The corresponding SEM morphologies of these circumferentially-notched samples are shown in **Figure 3.3**.

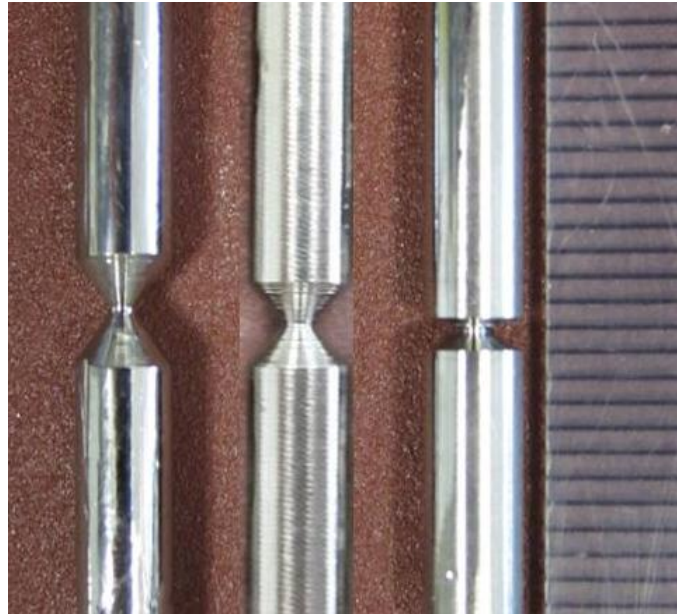


Figure 3.2 Optical image (OM) of the circumferentially-notched samples with angles of 120°, 90° and 45°, respectively.

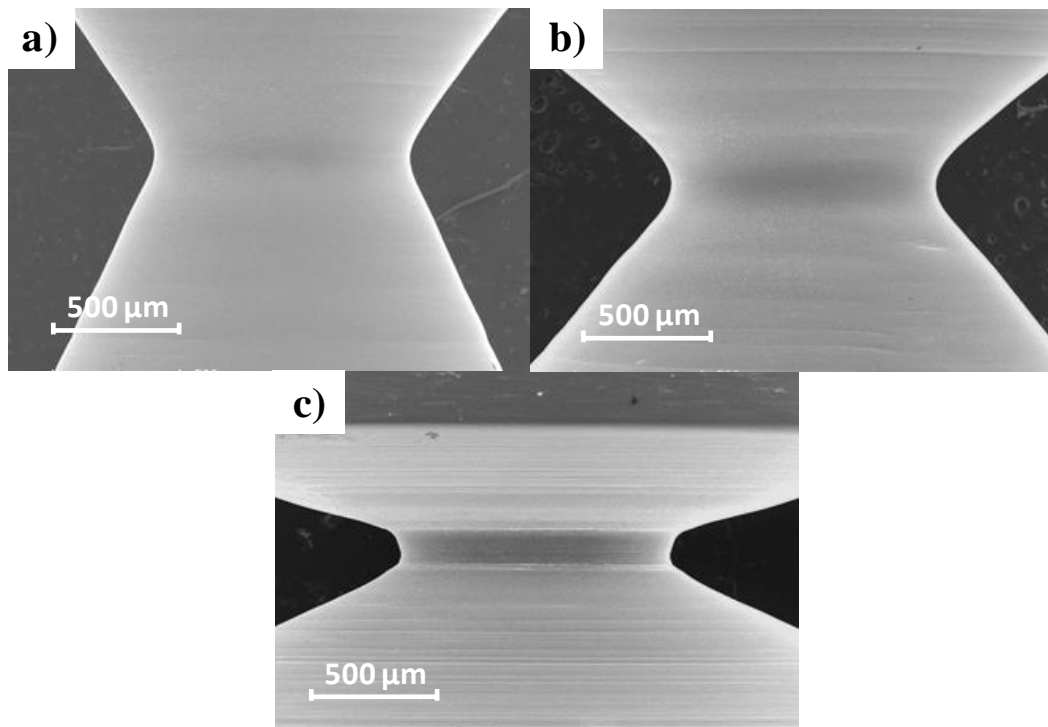


Figure 3.3 SEM images of the circumferentially-notched samples with angles of 120°, 90° and 45°, respectively.

Figure 3.4 shows the nominal tensile stress-extension curves for circumferentially-notched samples, with notch angles of 120° , 90° and 45° , respectively. The nominal stress is defined as the load divided by the minimum area of the circumferentially-notched specimen. The notched samples exhibit a plastic extension, followed by a maximum load and finally fracture. There are several important features for the net stress-extension curves need to be emphasized herein.

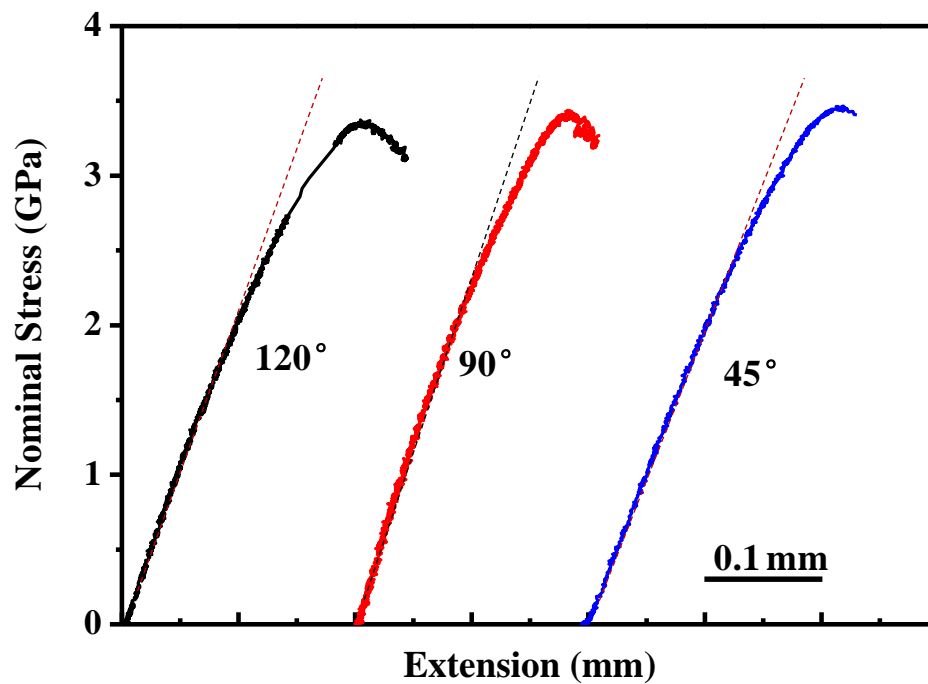


Figure 3.4 Nominal tensile stress-extension curves for circumferentially-notched $\text{Zr}_{64.13}\text{Cu}_{15.75}\text{Ni}_{10.12}\text{Al}_{10}$ BMG, with notch angles of 120° , 90° and 45° , respectively.

Firstly, both the general yielding stress and the maximum tensile stress show an increasing trend as the notch angle decreases. The general yielding stresses for samples with notch angles of 120° , 90° and 45° are 1.9 GPa, 2.1 GPa and 2.4 GPa, respectively. The maximum tensile stresses for samples with notch angles of 120° , 90° and 45° are approximately 3.3 GPa, 3.4 GPa and 3.5 GPa, respectively. Secondly, the tendency of serrated flow shows a decreasing trend as the notch angle decreases. It is commonly known that the plastic flow carrier in BMGs is shear band. Upon yielding, shear band is initiated and corresponds to one 'serrated flow' in the stress-strain curves. For the nominal tensile stress-extension curves of samples with notch angles of 120° and 90° , numerous serrated flows are found after maximum stress. However, there is negligible serrated flow for the sample of 45° notch. Therefore, it strongly indicates that shear banding can be controlled by changing the geometry of the tensile samples. Finally, all the nominal tensile stress-extension curves exhibit a strain hardening behavior after general yielding, which is quite different as compared with unconfined samples exhibiting strain softening behavior. This 'strain hardening' behavior will be discussed in **Chapter 5**.

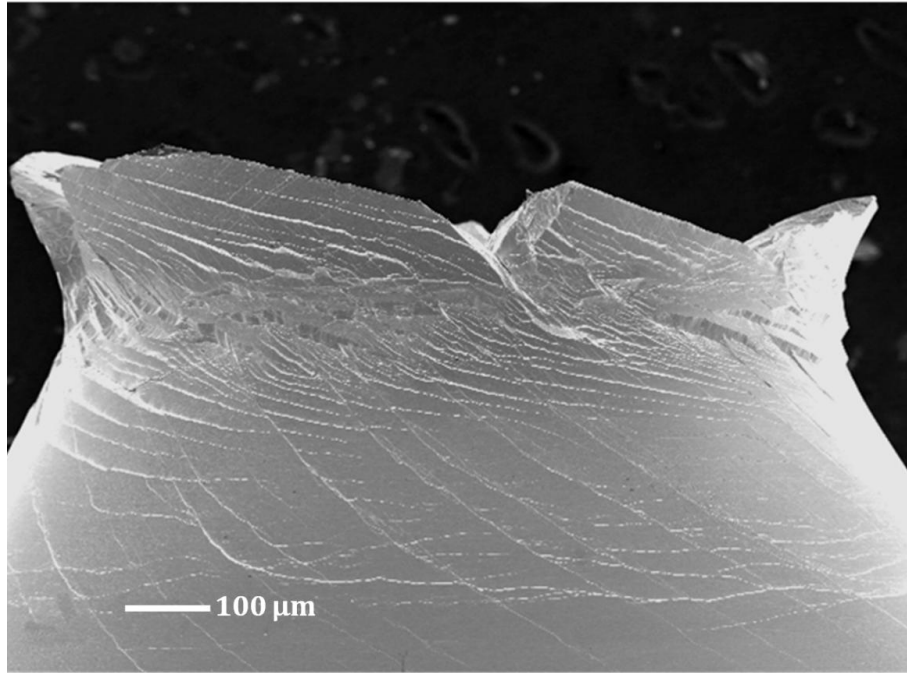


Figure 3.5 SEM image showing the side view of a 120° notched sample after fracture, with multiple shear bands on the surface.

Figure 3.5 shows the side view of a 120° notched sample after fracture. Profuse shear bands are found not only in the confined part (minimum area) of the sample, but also found out of the confined part of the sample, intersecting with each other. The angle of shear band in the confined part is only about 20° due to the effect of confinement, while the angle of shear band outside the confined part is about 40° which is comparable to that of notch free specimen in tensile test. Therefore, the circumferentially-notched sample with a notch angle of 120° cannot constrain all the shear bands within the confined region.

The SEM images of a circumferentially-notched sample with a notch angle of 90° before fracture are shown in **Figure 3.6**.

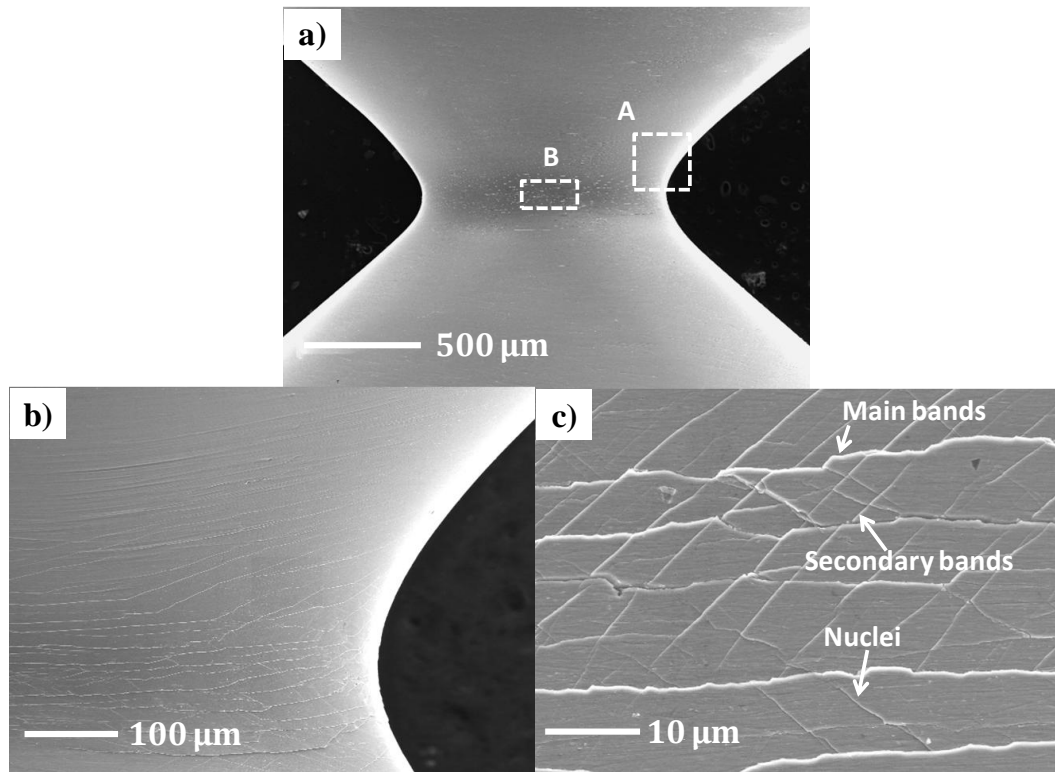


Figure 3.6 SEM images of a circumferentially-notched sample with a notch angle of 90° before fracture. The higher magnification of A and B in a) are shown in b) and c), respectively.

Unlike the surface morphology of a 120° notched specimen where profuse shear bands are found both in and outside the confined region, shear bands of the 90° notched sample are mostly concentrated in the confined region. Only tiny shear bands are detected outside the confined region, as shown in **Figure 3.6 b)**. As shown in **Figure 3.6 c)**, some of the main shear bands located in the center of the confined region are nearly normal to the loading direction, while the secondary shear bands are approximately 45°

with respect to the main bands. Furthermore, several shear-band nuclei, intersecting with the main shear bands and secondary shear bands, are also found. Based on these observations, it can be seen that the effect of confinement on shear banding process is enhanced by decreasing notch angle.

The SEM images of a circumferentially-notched sample with a notch angle of 45° before fracture are shown in **Figure 3.7**. As the notch angle decreasing to 45° , shear bands on the surface of notched sample is very limited. Compared with the shear bands on the surface of 120° and 90° notched samples, only shear steps and tiny shear bands can be observed, as shown in **Figure 3.7 b**).

To further verify the effect of confinement of 45° notched sample, the surface morphologies in the four corners of the 45° notched sample are carefully examined. **Figure 3.7 c-f**) show that no shear bands or shear offsets are found outside the confined region, which provides definitive proof that shear banding process can be controlled by reducing the notch angle. In addition, the trend of shear bands reducing as decreasing notch angle is consistent with that of serrations reducing in the stress-strain curves.

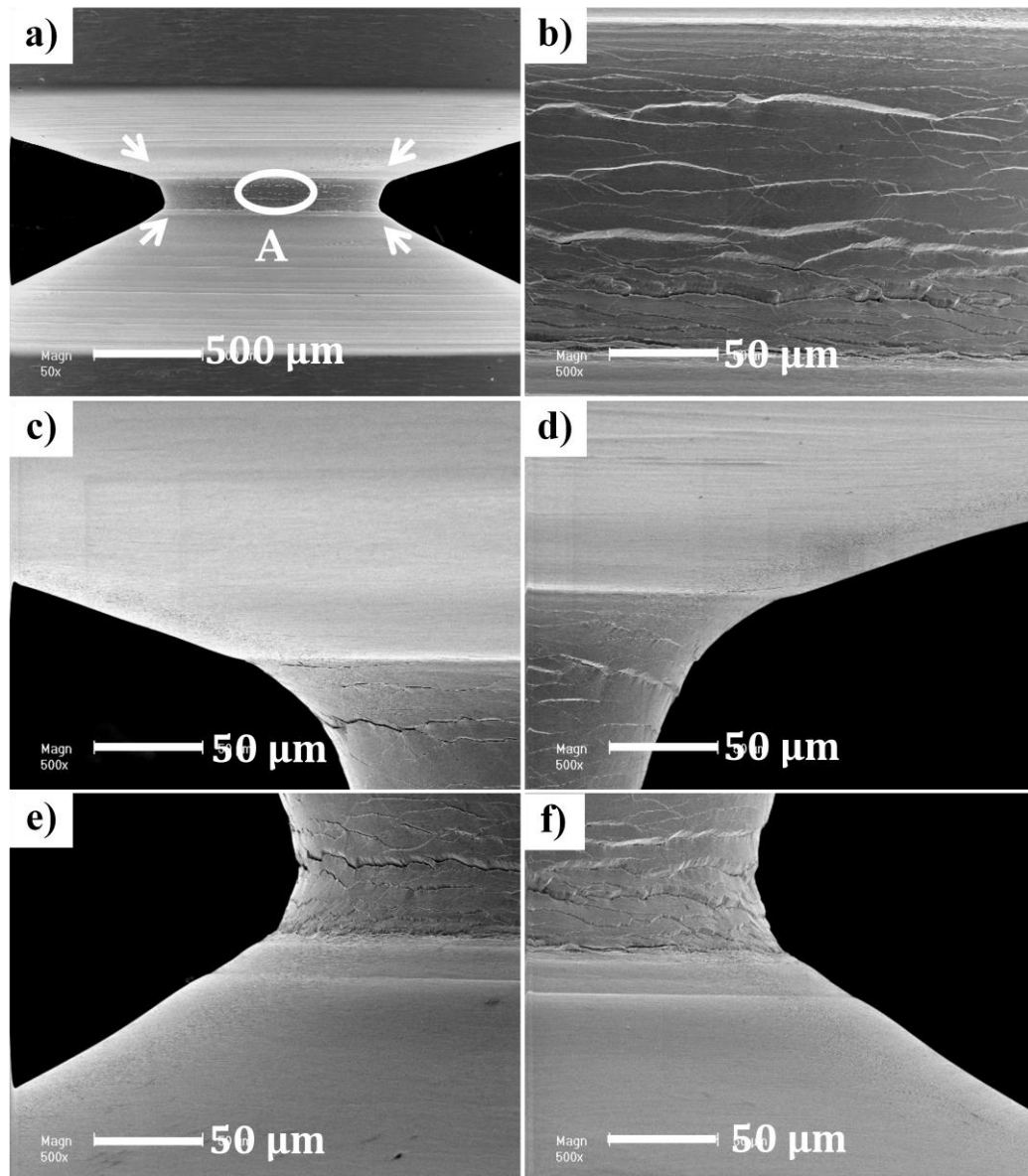


Figure 3.7 SEM images of a circumferentially-notched sample with a notch angle of 45° before fracture. The higher magnification of A in a) is shown in b), and the higher magnification of four corners illustrated in a) are shown in c)-f), respectively.

Figure 3.8 shows the SEM images of the side view of circumferentially-notched samples with notch angles of 120° , 90° and 45° after fracture, respectively. For the 120° notched sample, the fracture plane is along one dominant shear plane, which is approximately 45° with respect to the loading

direction. This feature is similar as that of notch free samples, in which catastrophic failure occurs along one dominant shear band. For the 90° notched sample, the fracture plane is almost normal to the loading direction. For the 45° notched sample, a cup and cone feature is formed after fracture, indicating a ductile fracture behavior for the BMG under highly confinement condition.

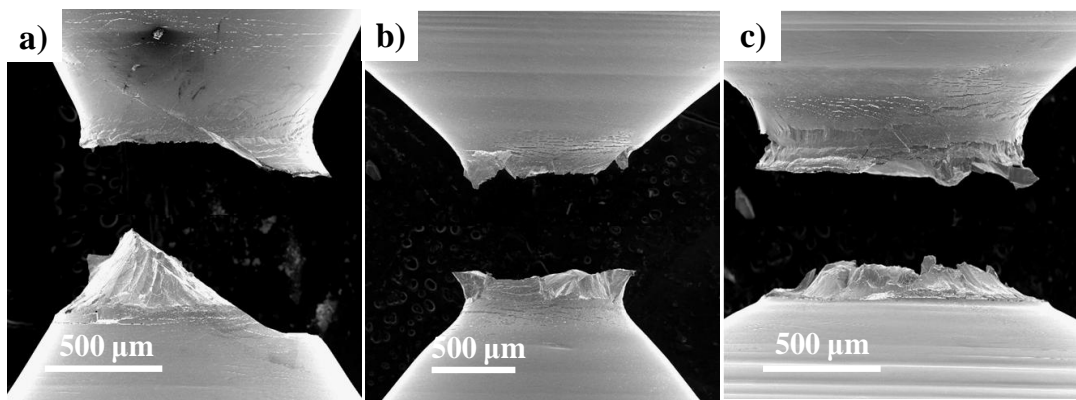


Figure 3.8 SEM images of the side view of circumferentially-notched samples with notch angles of 120°, 90° and 45° after fracture, respectively.

3.2.2 Deformation behavior of slit-notched samples

Figure 3.9 shows the optical image of slit-notched samples with aspect ratios of 2:1, 1:1 and 0.5:1, respectively. The corresponding SEM morphologies of these samples are shown in **Figure 3.10**.

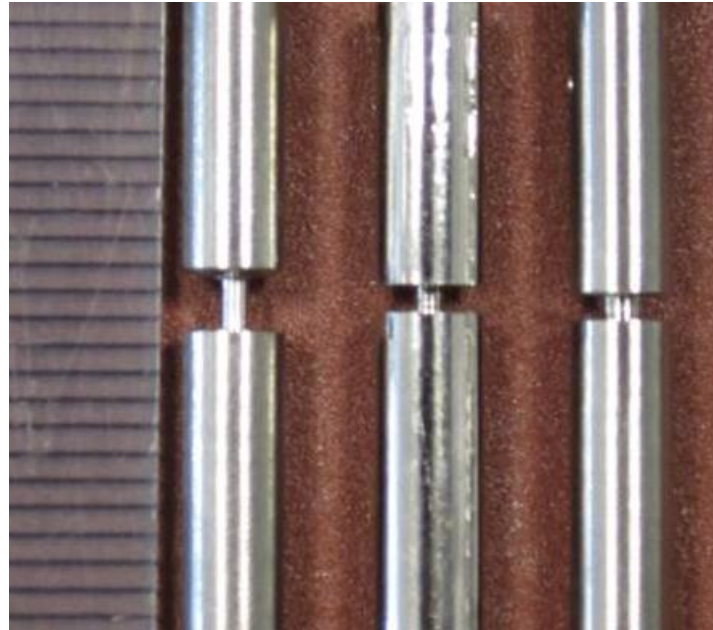


Figure 3.9 Optical image of the slit-notched samples with aspect ratios of 2:1, 1:1 and 0.5:1, respectively.

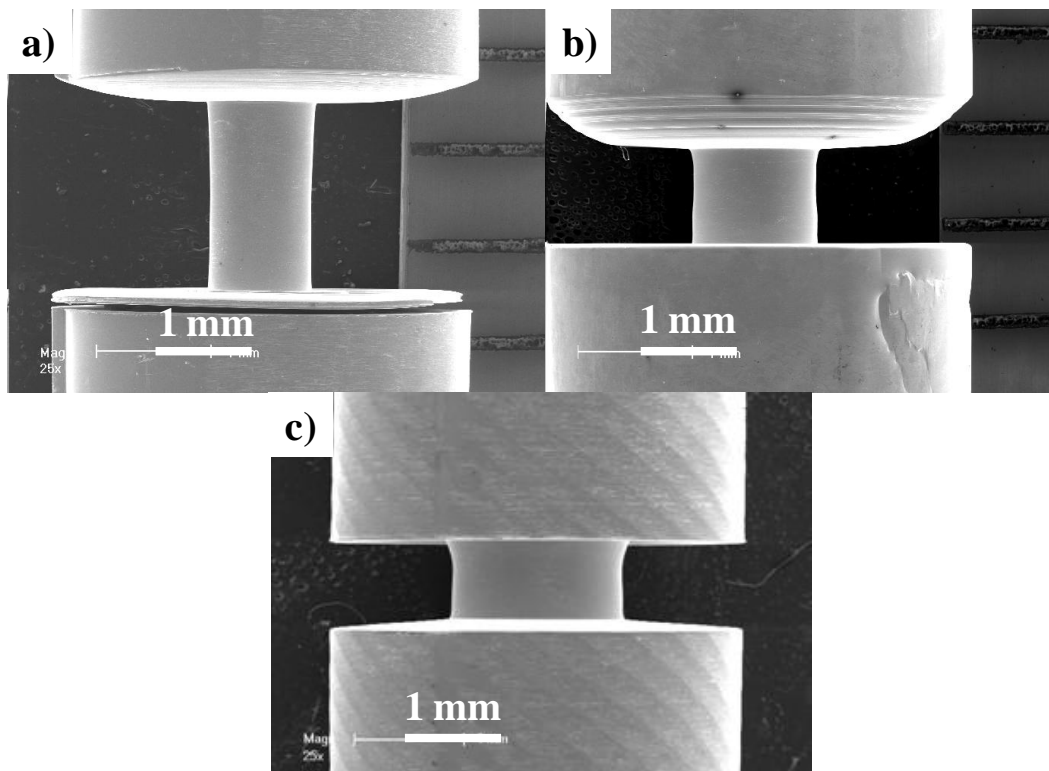


Figure 3.10 SEM images of the slit-notched samples with aspect ratios of 2:1, 1:1 and 0.5:1, respectively.

Figure 3.11 shows the nominal stress-extension curves of the slit-notched samples with aspect ratios of 2:1, 1:1, and 0.5:1, respectively.

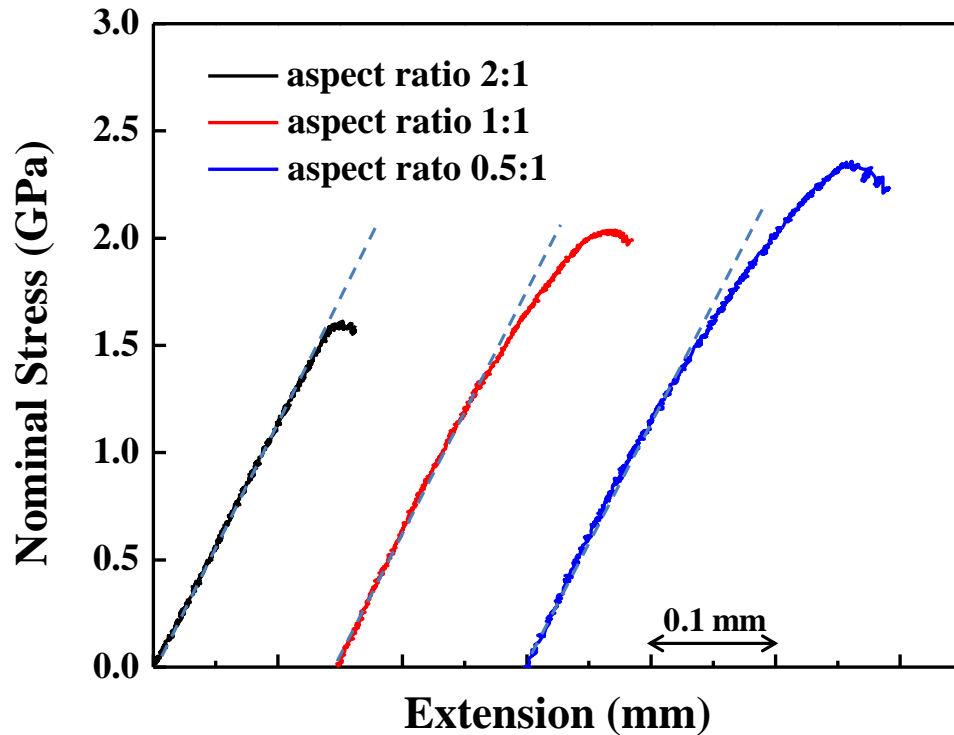


Figure 3.11 Tensile net stress-extension curves for slit-notched samples, with aspect ratios of 2:1, 1:1 and 0.5:1, respectively.

For the 2:1 sample, yielding occurs at about 1.6 GPa, and the sample fails with a few pop-in serrations. For the 1:1 sample, the yielding stress is about 1.4 GPa. However, the fracture stress increases to about 2.1 GPa. For the 0.5:1 sample, the fracture stress further increases to about 2.3 GPa, and followed by a few serrations. It should be noted that the stress-extension curves for 1:1 and 0.5:1 samples exhibit plastic deformation behavior after yielding. Moreover, the plastic deformation for the 0.5:1 sample is larger than that of 1:1 sample. These results indicate that tensile plastic deformation is enhanced as the

3. Achieving tensile ductility of BMGs at room temperature

sample's aspect ratio decreasing. If the sample aspect ratio can be further decreased, large tensile plastic deformation may be obtained.

The mechanical behaviors of the circumferentially-notched and slit-notched samples are summarized in **Table 3.1**.

Table 3.1 Mechanical properties of circumferentially notched and slit notched samples.

Sample	Yield strength (GPa)	Tensile strength (GPa)	Plastic extension (mm)
Cir-120°	1.9	3.3	0.15
Cir-90°	2.1	3.4	0.12
Cir-45°	2.4	3.5	0.10
Slit-2:1	1.6	1.6	0.02
Slit-1:1	1.4	2.0	0.11
Slit-0.5:1	1.5	2.3	0.15

Cir refers to circumferentially-notched samples; Slit refers to slit-notched samples

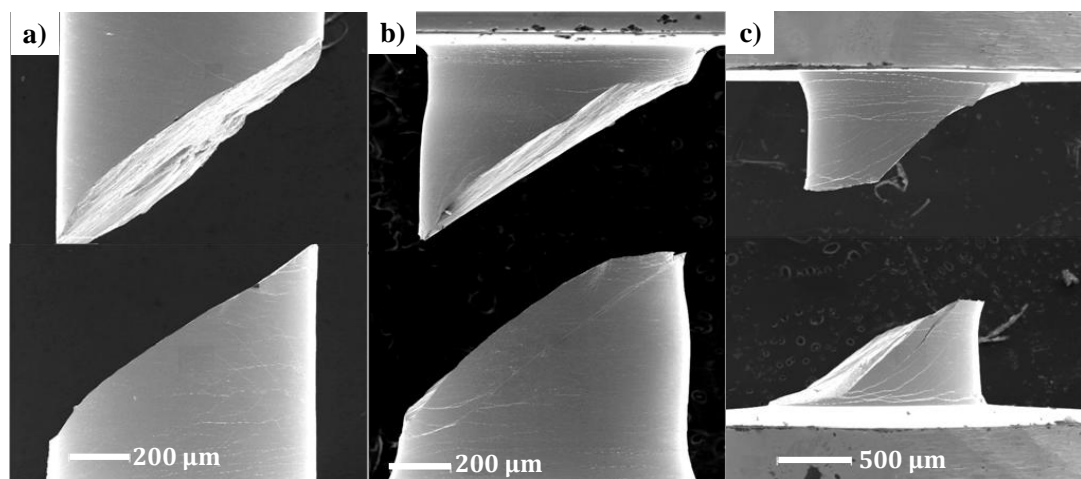


Figure 3.12 SEM images of the side view of the slit-notched samples after fracture, with aspect ratios of 2:1, 1:1 and 0.5:1, respectively. The fracture angles for a), b) and c) are approximately 57°, 45° and 63°, respectively.

Figure 3.12 shows the SEM morphologies of slit-notched samples after fracture. The fracture angle for the 2:1 sample is about 57° , which is close to the reported value for Zr-based BMGs without confinement [75]. As for the sample with aspect ratio of 1:1, the fracture angle is about 45° , from the upper right to lower left of the sample. With further decreasing the aspect ratio to 0.5:1, the fracture angle changes to about 63° with respect to the loading direction. Therefore, it can be concluded that the fracture angle of the BMG can be tuned by changing the aspect ratio of the sample.

To further investigate the deformation behavior of the slit-notched sample, the morphology of the sample before rupture was also carefully examined. **Figure 3.13** shows the SEM images of a slit-notched sample with aspect ratio of 1:1 before rupture. One dominant shear band appears from the upper right to lower left corner of the sample, indicating this sample would fracture along the shear plane. Besides, large shear offset together with tiny shear bands are also found, as shown in **Figure 3.13 b**). When rotating the same sample to the back side for further observation, a high density of shear bands are found, spreading from upper left to lower right corner of the sample. Despite profuse shear bands are found in this 1:1 sample, the fracture mode is still shear banding.

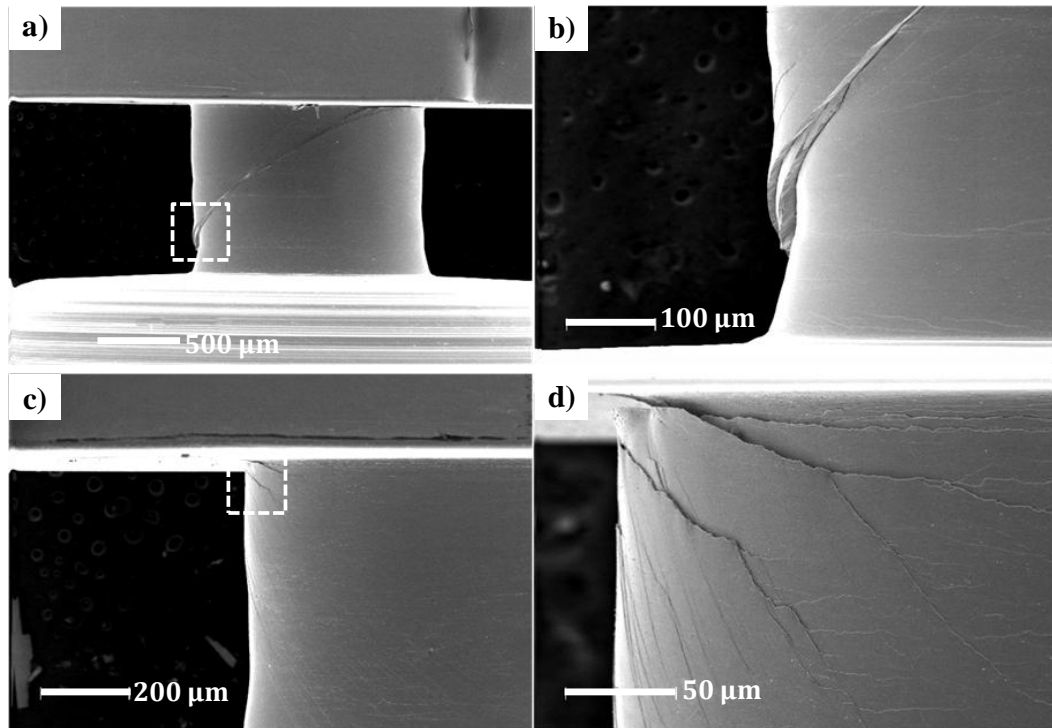


Figure 3.13 SEM images of a slit-notched sample with aspect ratio of 1:1 before rupture. Side view of the sample is shown in a), rotating 180° of the same sample c), higher magnification shown in b) and d).

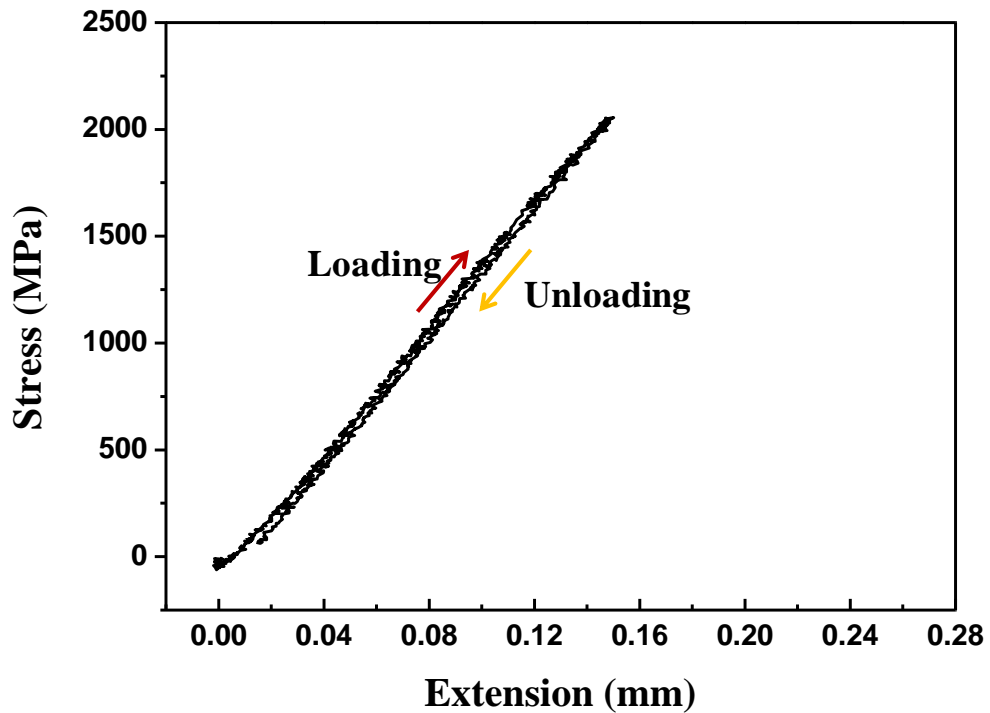


Figure 3.14 Loading-unloading curves of a slit-notched sample with aspect ratio of 0.5:1, unloading at 2.1 GPa.

Figure 3.14 shows the loading-unloading curve of a slit-notched sample with aspect ratio of 0.5:1. Upon loading, the curve exhibits good linearity. After unloading at about 2.1 GPa, the unloading curve almost goes back to the initial position, indicating a total elastic behavior in this region. The corresponding SEM morphologies of the unloading sample are shown in **Figure 3.15**.

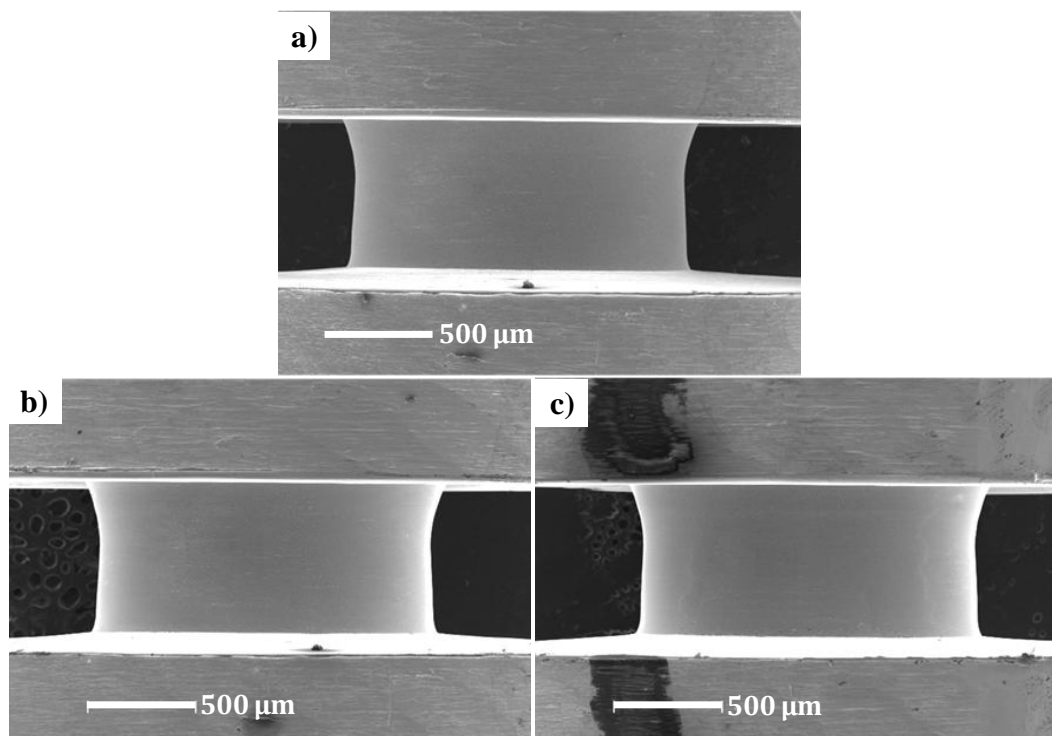


Figure 3.15 SEM images of the corresponding unloading sample of an aspect ratio of 0.5:1. The initial morphology of the sample before tension a), unloading at about 2.1 GPa b), rotating 180° of the unloading sample c).

Before loading, no shear bands or other contaminations is observed. After unloading at about 2.1 GPa, the sample perfectly goes back to its initial

state and no elongation can be seen in the current SEM resolution, showing completely elastic behavior. Furthermore, no shear bands or shear offsets are detected by carefully screening the front side and back side of this sample (Figure 3.15 b) and c). Compared with the yield stress (1.5-1.6 GPa) of bulk sample under uniaxial tensile condition, yield stress of the confined sample is undoubtedly increased. Therefore, our strategy to change the geometry of aspect ratio is a feasible way to delay shear banding.

3.2.3 Deformation behavior of rectangularly-notched samples

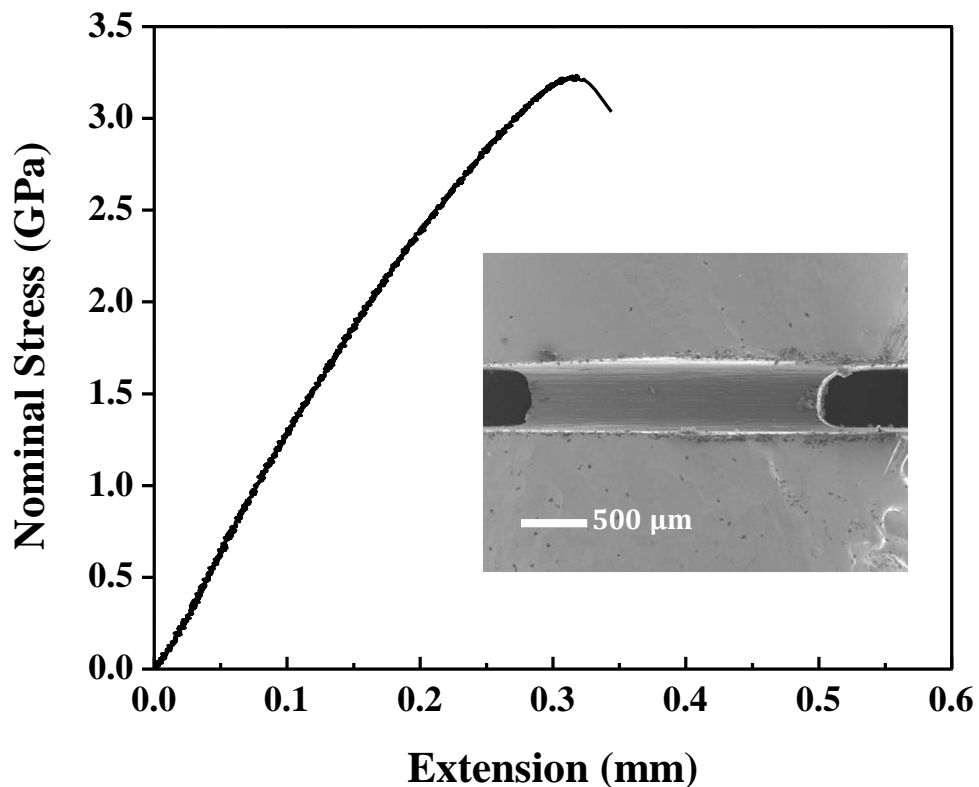


Figure 3.16 Representative stress-extension curve of the rectangularly-notched sample. The inset shows the SEM image of the rectangularly-notched sample before tension.

The representative stress-extension curve of the rectangularly-notched sample is shown in **Figure 3.16**. The stress-extension curve shows a non-linear deformation behavior after general yielding, just as the behavior of circumferentially-notched samples, and followed by a maximum stress at about 3.2 GPa. The non-linear deformation behavior indicates tensile ductility can also be achieved for the rectangularly-notched sample. The morphology of the rectangularly-notched sample is shown in the inset.

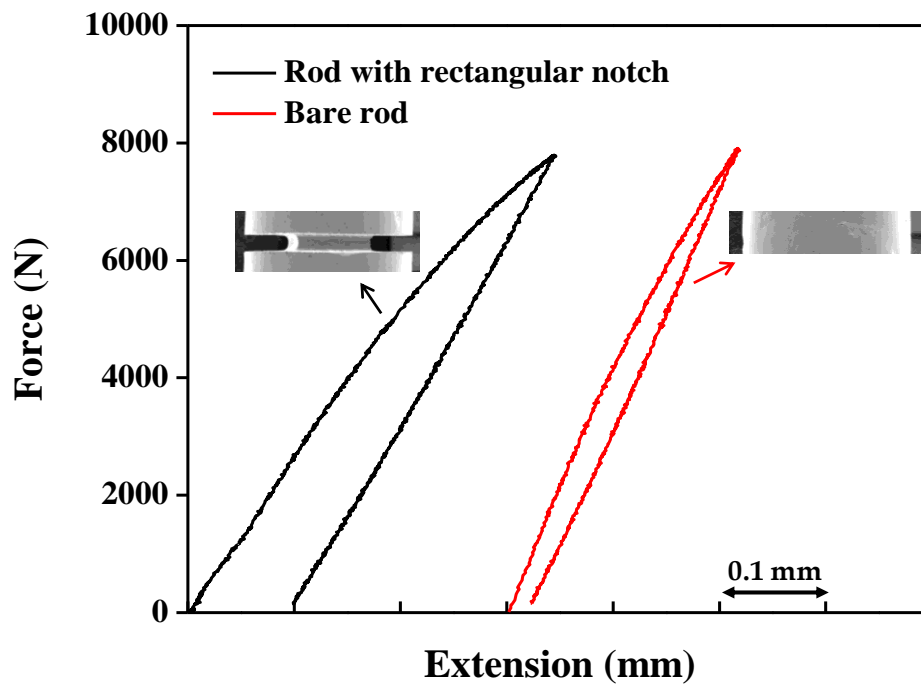


Figure 3.17 Loading-unloading curves of the rectangularly-notched sample and the bare rods without notch. The insets show the morphology of the rectangularly-notched sample and the bare rod.

To study the deformation behavior of the rectangularly-notched sample, unloading experiment was carried out both for the notched sample and notch

free sample. **Figure 3.17** show the loading-unloading curves of the notched and notch free samples.

The sample with notch is loaded up to 8000 N, corresponding to a stress of 2.2 GPa, and followed by unloading. After unloading, about 0.1 mm elongation is obtained. However, it has to be emphasized here that this 0.1 mm elongation cannot be regarded as the plastic deformation experienced by the sample. The effect of the testing machine has to be considered. The loading-unloading experiment was also taken for the notch free sample. After unloading at about 8000 N, which corresponds to only 640 MPa for the notch free sample and is totally within the elastic regime, about 0.03 mm elongation is obtained. Therefore, this 0.03 mm could be regards as the system error for the testing system. Despite a system error of 0.03 mm, plastic deformation is unquestionably experienced by the rectangularly-notched sample.

The corresponding SEM images of the rectangularly-notched at 2.2 GPa are shown in **Figure 3.18**. Before tensile testing, the morphology of the rectangularly-notched sample is shown in **Figure 3.18 a)**. No shear bands or shear offsets is detected on the surface of the sample, as shown in the high magnification SEM image in **Figure 3.18 c)**. After tensile testing, the morphology of the sample is shown in **Figure 3.18 b)** and **d)**. Compared with the dimension of the sample before tensile testing, about 11 % tensile elongation is obtained which is comparable to the elongation (13 %) measured

by stress-extension curve. In addition, shear offsets rather than profuse shear bands intersecting with each other are found on the surface of the sample.

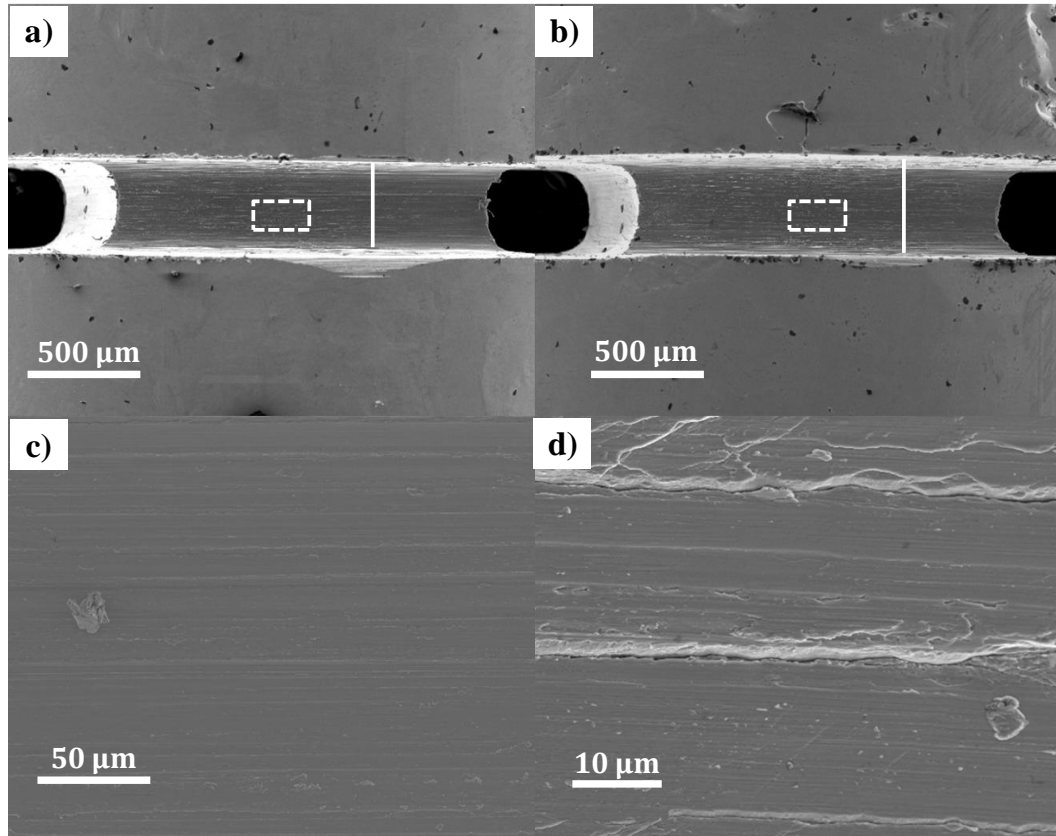


Figure 3.18 SEM images of the rectangularly-notched sample unloading at 2.2 GPa. a) before tensile testing, and b) after tensile testing. The higher magnification of the sample before c) and after d) tensile testing.

3.2.4 Deformation behavior of a 5 mm cylindrical sample with Bridgman notch

Based on the results presented in sections 3.2.1-3.2.3, it can be found that there is a clear transition from shear banding dominant deformation to less

shear banding dominant deformation as the confinement condition is more severe, i.e., decreasing the notch angle or decreasing the aspect ratio of the confined samples. In this section, to increase the severity of the confinement condition, we design a 5 mm cylindrical sample with the geometry of Bridgman notch. The deformation behavior of the samples with this geometry is studied and presented. **Figure 3.19 a)** shows the schematic illustration of a 5 mm cylindrical sample fabricated with Bridgman notch. The corresponding optical image and SEM image are also shown in **Figure 3.19 b) and c)**.

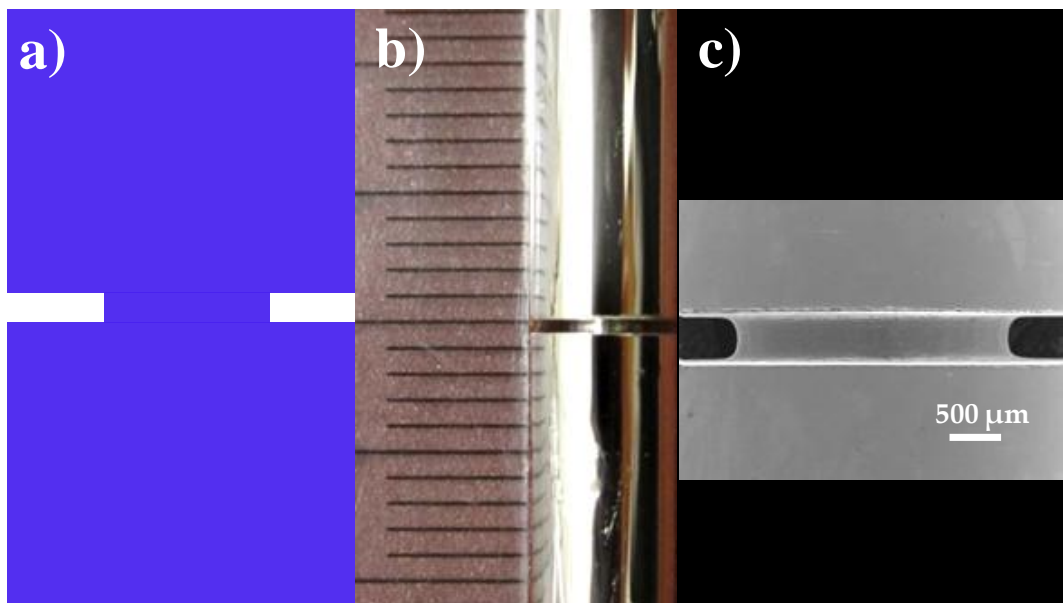


Figure 3.19 Schematic illustration of the 5 mm cylindrical sample with Bridgman notch shown in a). The optical image and SEM image of the Bridgman notched sample are shown in b) and c).

Figure 3.20 shows the tensile stress-strain curves of the 5 mm cylindrical sample with Bridgman notch, the strain in the figure has no unit and all the curves are shifted for comparison. **Curve 1** is the stress-strain curve for a

sample that has been pulled apart. After general yielding at about 1.8 GPa, the stress-strain curve starts to deviate from linearity, followed by a 'strain hardening' phenomenon until a maximum stress about 2.9 GPa, and finally ruptured by the characteristic of a few serrations in the stress-strain curve. For BMGs, it is generally known that 'strain softening' [103, 139] occurs upon yielding instead of 'strain hardening' as in crystalline materials. Therefore, this apparent 'strain hardening' capability is worthy of a focused study and will be presented in **Chapter 5**.

Curve 2 is the loading-unloading stress-strain curve. After unloading at about 2.5 GPa which corresponds to a strain reaching 15%, about 6% plastic deformation is achieved. Based on this information, the elastic limit for the sample under this confinement condition would be about 9%, which is much beyond the 2% elastic limit for BMGs under confinement free condition. Furthermore, the 9% recoverable elastic strain also means the sample exhibits non-linear elastic behavior after yielding.

Curve 3 is the stress-strain curve unloaded at 2.1 GPa. After unloading, the stress-strain curve recovers back, and no detectable plastic deformation is found at the current testing system resolution.

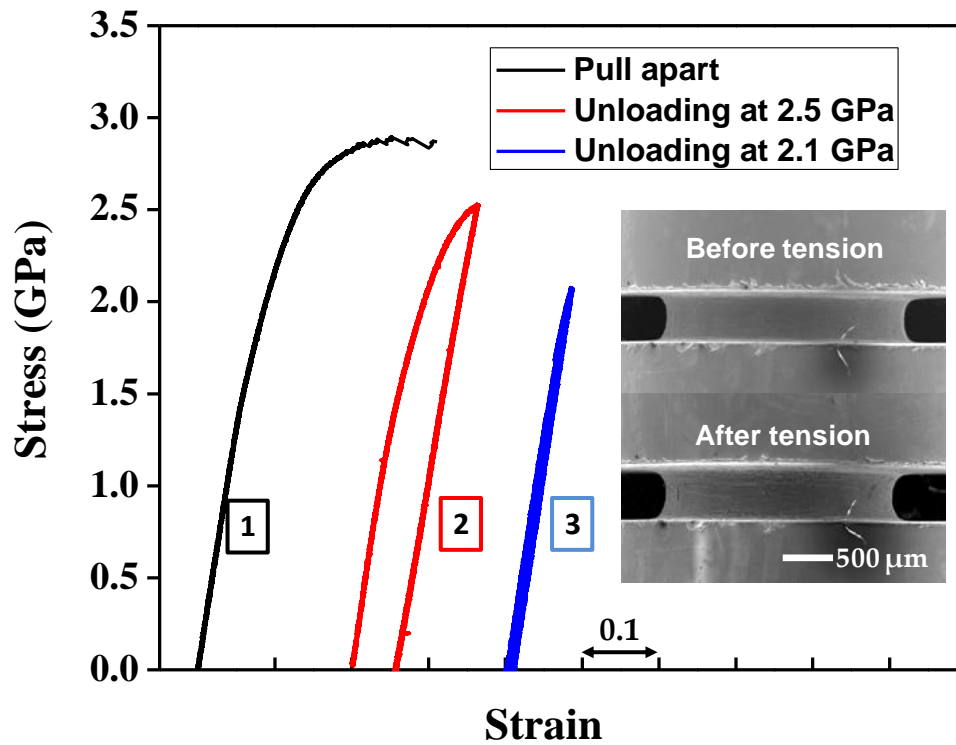


Figure 3.20 Tensile stress-strain curves of the 5 mm cylindrical rod with Bridgman notch. The inset shows a sample before and after tensile testing, showing 9.3 % elongation in the loading direction.

The inset in **Figure 3.20** shows the SEM images of the sample before and after tensile testing. According to the measurement in these SEM images, about 9.1 % elongation (from 394 μm to 430 μm) in the loading direction and about 4.5 % shrinkage (from 2360 μm to 2258 μm) in the diameter direction are obtained. The elongation in length and shrinkage in diameter indicate a homogeneous deformation mechanism for this BMG under tensile confinement condition. Moreover, based on the measurement of the SEM image, the volume of the sample decreases approximately 0.0012 after plastic deformation. This result indicates that the density increases (densification).

An in-depth study and discussion of the densification phenomenon will be presented in **Chapter 5**.

To investigate the tensile deformation behavior of the Bridgman notched sample, in-situ camera shooting was carried out at various moments during the strain evolution. **Figure 3.21 a)** shows the stress-strain curve of the Bridgman notched sample. The green stars (I - V) represent the places where in-situ camera shooting images are taken, and the corresponding images are shown in **Figure 3.21 b)**. As the load increases, the measured strain also increases. The measured strains for I - V are 0%, 8%, 11%, 16% and 31%, respectively.

To further verify the strain, images with higher magnifications are shown in **Figure 3.21 c)**. We notice that there is a light spot reflected from the surface during the tensile testing, which is a good indicator for the measurement of the tensile strain. By measuring the length of the light spot, tensile strain can reach as high as ~30% which is an extremely large value as compared with the value (2%) for BMGs tested at confinement free condition.

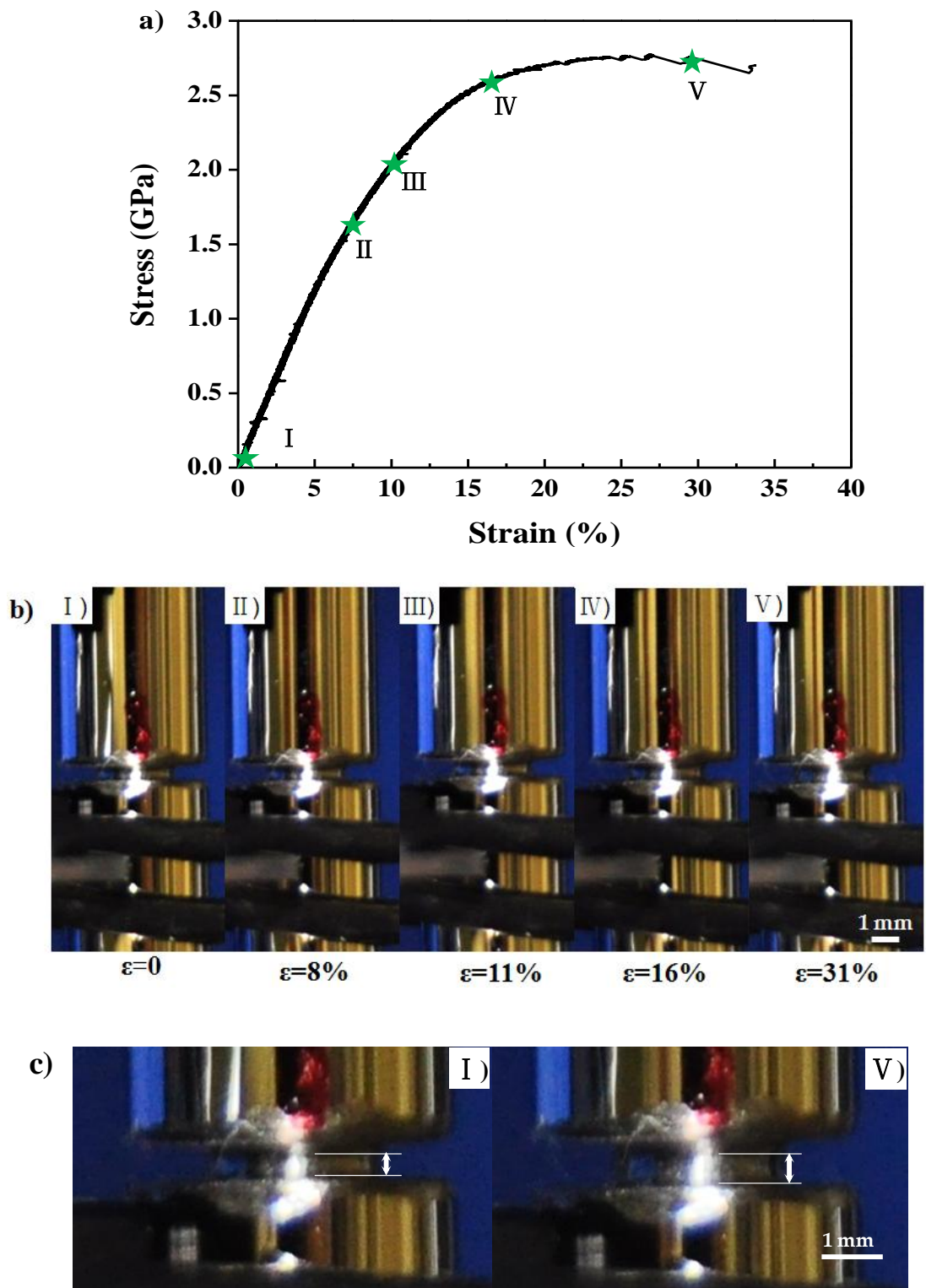


Figure 3.21 Tensile behavior and corresponding in-situ camera shooting strain of the 5 mm cylindrical rod with Bridgman notch. a) Stress-strain curve calculated from the raw load-extension data. b) In-situ camera shooting strain at the places marked in the stress-strain curve. c) higher magnification images of the shooting strain, together with the measurement from the reflected light spot at notch surface.

The loading-unloading tensile behavior of the Bridgman notched sample is shown in **Figure 3.22**. **Figure 3.22 a)** shows the loading-unloading stress-strain curve of the sample. The sample is firstly loaded, and followed by unloading at about 2.5 GPa. Based on the loading-unloading curve, about 6.3 % permanent plastic deformation is obtained.

In addition, three in-situ camera shooting images were taken at initial position, maximum loading position and completely unloading position, marked as I , II , III in the loading-unloading curve, respectively. The in-situ camera images corresponding to I , II , III are shown in **Figure 3.22 b)**. According to the measurement, the strains for I , II , III are 0 % , 19 % and 6 % , respectively, which are comparable to those measured by loading-unloading stress- strain curve. To double check the strain measurement, post SEM image of the unloading sample is also taken. The sample is about 6 % increase in length and about 2.5 % shrinkage in diameter after tensile testing, as shown in **Figure 3.22 c)**. Based on the measurement results, the strains measured by stress-strain curve, in-situ camera shooting and post-SEM images are in good agreement with each other, providing detailed information of strain evolution during plastic deformation.

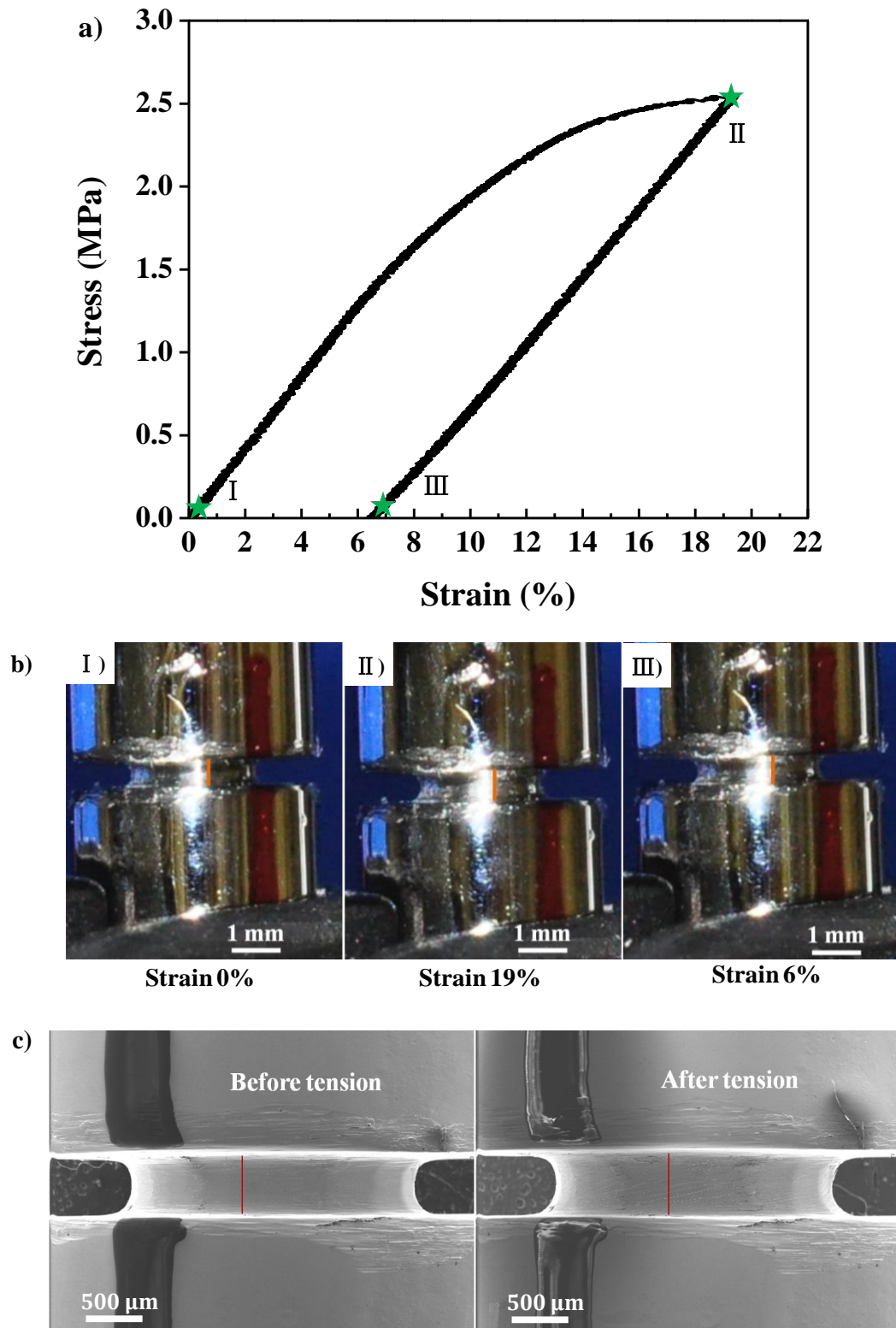


Figure 3.22 Loading-unloading tensile behavior and corresponding in-situ camera shooting strain of the 5 mm cylindrical rod with Bridgman notch. a) Stress-strain curve calculated from the raw load-extension data. b) In-situ camera shooting strain at the places marked in the stress-strain curve. c) SEM images of the testing sample before and after unloading.

3. Achieving tensile ductility of BMGs at room temperature

To rule out the possibility of voids or microcracks formation during the homogeneous plastic deformation, the entire cross sectional area of the deformed sample was carefully examined by SEM. **Figure 3.23** shows the representative SEM image of a 7 % plastically deformed sample. No voids or microcracks can be found. Therefore, it can be concluded that the large tensile elongation and homogeneous plastic deformation achieved in this work is not caused by the formation of voids or microcracks.

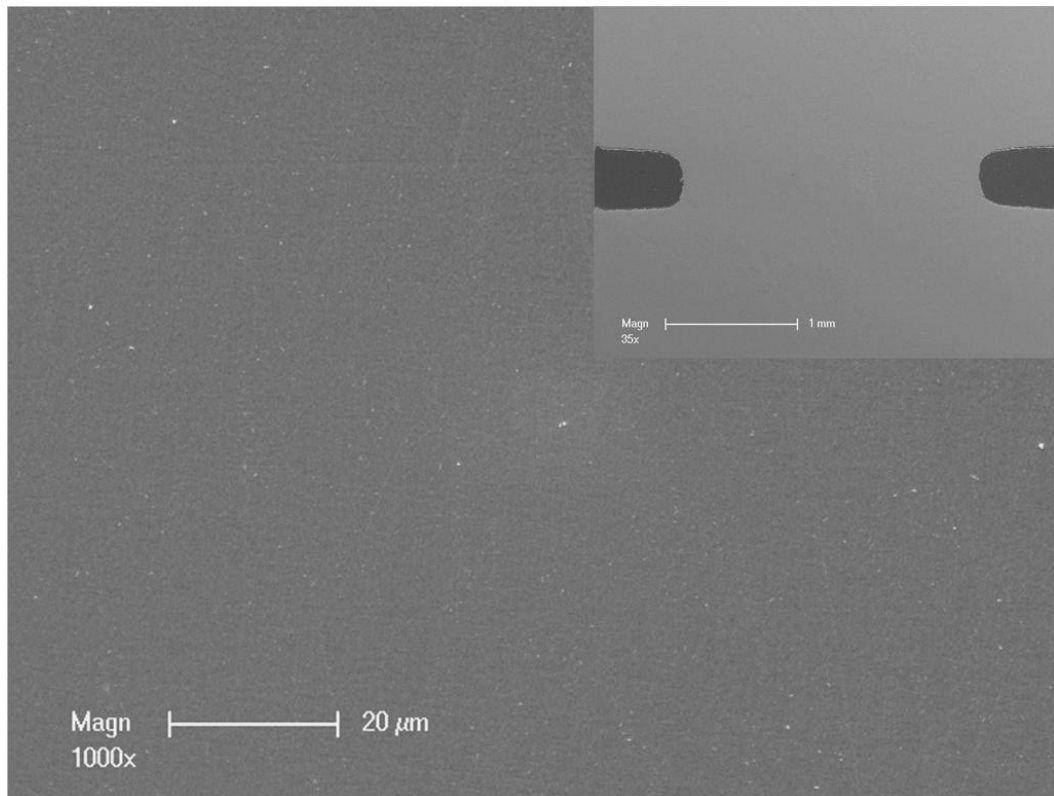


Figure 3.23 Representative cross sectional SEM image of a 7 % plastically deformed sample, showing no voids or microcracks. The inset shows the entire morphology of the plastically deformed notch.

However, it has to be admitted that shear offsets are observed on the surface of the plastically deformed sample. People may argue that these

'shear offsets' are indicators of shear banding, therefore, the sample is deformed through shear banding deformation mode rather than homogeneous deformation mode. Our defense on this argument is presented as follows.

Firstly, it is commonly known that shear banding is a process of strain localization. During plastic deformation, plastic strain is spontaneously allocated into narrow bands, termed as shear bands. Therefore, if the sample deforms homogeneously through shear banding, geometrically speaking, multiple shear bands have to be formed and intersect with each other among the entire sample, as illustrated in **Figure 3.24 b)**.

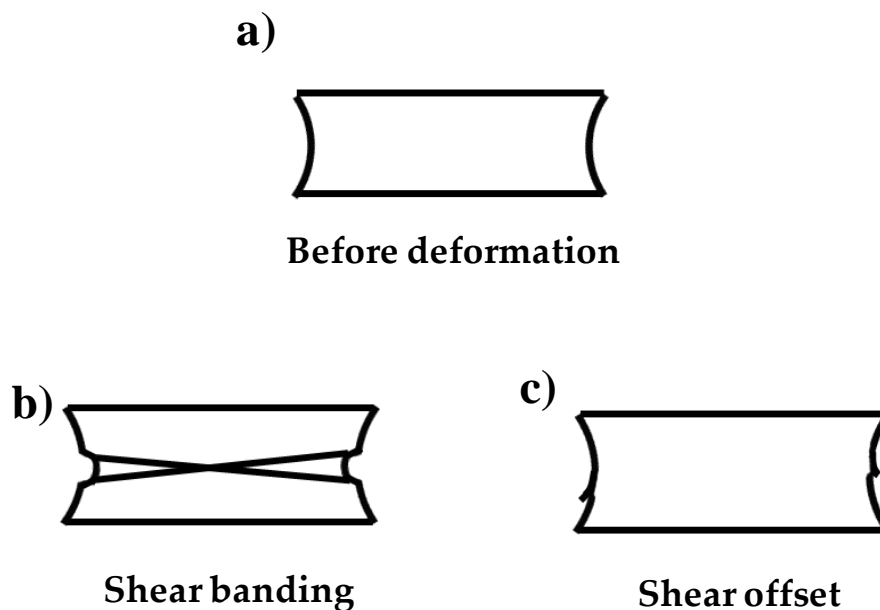


Figure 3.24 Schematic illustration of the plastically deformed sample through different deformation modes. a) original sample before deformation, b) plastically deformed through shear banding, showing multiple intersecting shear bands, c) plastically deformed through homogeneous deformation, showing shear offsets on the surface due to stress concentration.

On the other hand, it is known that notches, holes, and cracks are served as stress concentrators during deformation. In the current circumstance, despite the sample is deformed homogeneously, shear offset may occur at the notch root due to stress concentration but should not propagate into the whole sample, as illustrated in **Figure 3.24 c)**.

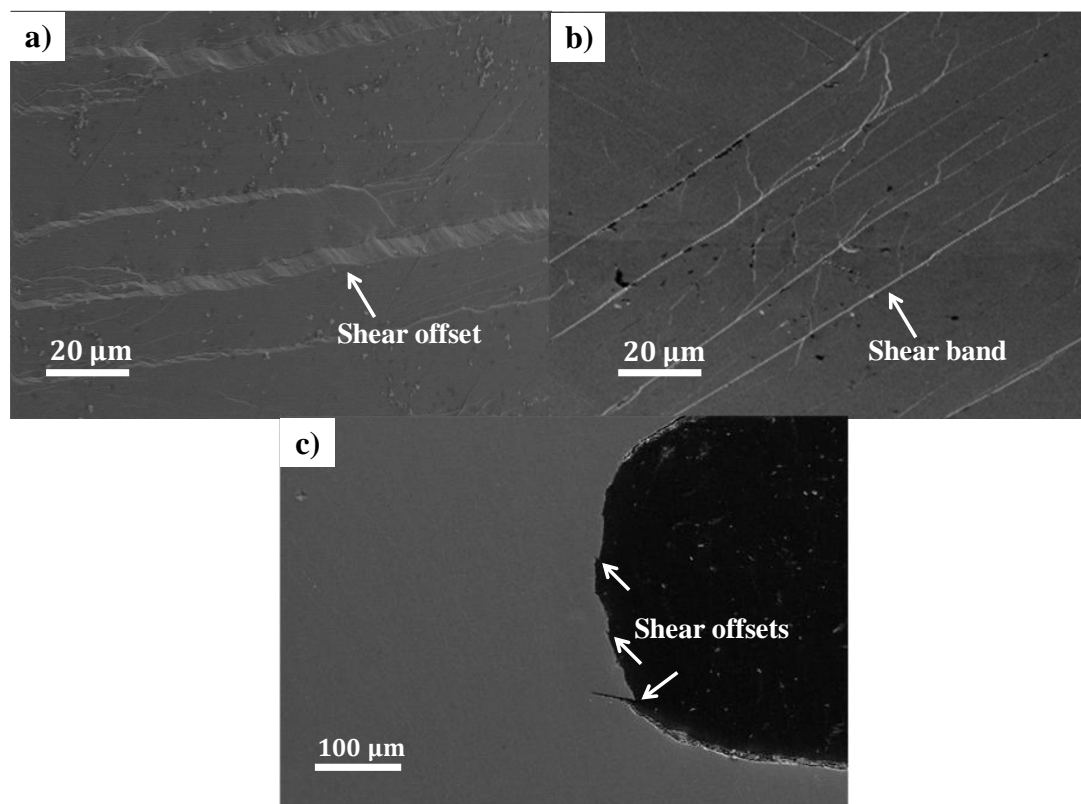


Figure 3.25 SEM images of the morphologies of plastically deformed samples. a) surface morphology of a tensile sample of 7% ductility, showing shear offsets, b) surface morphology of a 8% compressed sample with gauge dimension similar to the tensile sample, showing shear bands, c) cross-sectional morphology of the 7% ductility sample, showing shear offsets on the outer surface.

To verify which scenario is the case, the morphologies of the plastically deformed sample is examined by SEM, and are shown in **Figure 3.25**. **Figure**

3.25 a) shows the surface morphology of a tensile sample of 7% ductility. It is clearly seen that shear offset instead of multiple shear bands are detected. For comparison, the surface morphology of a compressive sample is also shown, as in **Figure 3.25 b)**. In this case, shear bands are found on the surface, indicating a deformation mode by shear banding. The cross-sectional morphology of the 7% deformed sample is shown in **Figure 3.25 c)**. Only shear offsets are seen on the outer surface.

Secondly, if the deformation mode is shear banding; multiple shear bands would form through the entire sample, which causing dilatation and softening of the sample. As such, there would be hardness valleys if the hardness measurement is conducted. However, this is not the case according to the hardness measurement result (will be presented in **Chapter 5**). Therefore, based on the above analysis, the deformation mode in our case is homogenous deformation.

3.3 Discussion

3.3.1 Comparison between homogeneous deformation at high temperature and at room temperature

Homogeneous deformation of metallic glasses is known to occur at temperatures near or above the glass transition temperature ($T_g=645$ K for this metallic glass). In that case, STZs are uniformly distributed, and large ductility is achieved due to the viscous-like homogeneous flow [53]. The representative tensile stress-strain curve for high temperature homogeneous flow exhibits the characteristics of a peak stress near the elastic limit, followed by strain softening and steady flow, and finally fracture occurs when the area of the sample is drawing-to-a-point [31, 140]. These characteristics of high temperature homogeneous flow are totally different from the room temperature homogeneous flow here in two aspects. Firstly, the room temperature homogenous flow reported here shows strain hardening (details will be presented in **Chapter 5**) and ~25 % elongation before failure, as opposed to strain softening at high temperature. Secondly, shear failure may still occur as some of the testing samples show serrated flow which is an indication of shear banding. Although the shear banding mechanism may not be fully suppressed, at least, it is delayed and requires higher stress to initiate.

3.3.2 Variation of tensile ductility as stress state parameter

In order to rationalize the virous tensile confinement state in this study, stress state parameter is introduced. Under fully plastic conditions, Bridgman's analysis of the stress distribution in a necking bar may be used to estimate the stress state parameter, the ratio of the mean stress (σ_m) to the effective stress (σ_{eff}), at the center of the notched bar [141]:

$$\frac{\sigma_m}{\sigma_{eff}} = \frac{1}{3} + \ln\left(\frac{a}{2\rho} + 1\right) \quad (3.1)$$

where a is the final minimum bar radius and ρ is the radius of the notch. By changing the notch or bar radii, the stress state may be varied from uniaxial ($a/2\rho \rightarrow 0$, $\sigma_m/\sigma_{eff} \rightarrow 1/3$) to nearly triaxial ($a/2\rho \rightarrow \infty$, $\sigma_m/\sigma_{eff} \rightarrow \infty$). The schematic illustration of the geometry at the neck is shown in **Figure 3.26**.

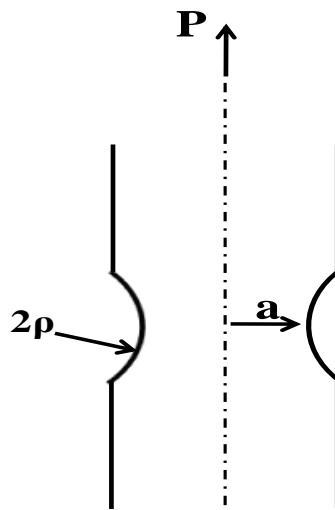


Figure 3.26 Schematic illustration of the geometry at the neck.

3. Achieving tensile ductility of BMGs at room temperature

Based on the Bridgman's analysis, the stress state parameters in this study are summarized in **Table 3.2**.

Table 3.2 Stress state parameter calculated by Bridgman's analysis.

Sample	Measured a (mm)	Measured 2q (mm)	σ_m/σ_{eff}
Cir-120°	0.53	0.46	1.10
Cir-90°	0.54	0.35	1.26
Cir-45°	0.54	0.21	1.60
Slit-2:1	0.54	1.84	0.58
Slit-1:1	0.64	1.04	0.81
Slit-0.5:1	0.89	0.86	1.04
Rectangular	1.06	0.50	1.47
Bridgman-5mm	1.30	0.50	1.61

Cir refers to circumferentially-notched samples, Slit refers to slit-notched samples

The extension as a function of stress state parameter is shown in **Figure 3.27**, some data points collected from reference [142] are also shown for comparison. The extension generally shows an increasing trend as the stress state parameter increases. Based on the results in section **3.2.1-3.2.4**, it can be concluded that shear banding dominant deformation mode is prohibited by increasing the stress state parameter, thus, tensile ductility can be achieved. On the contrary, no tensile ductility can be observed in the reference.

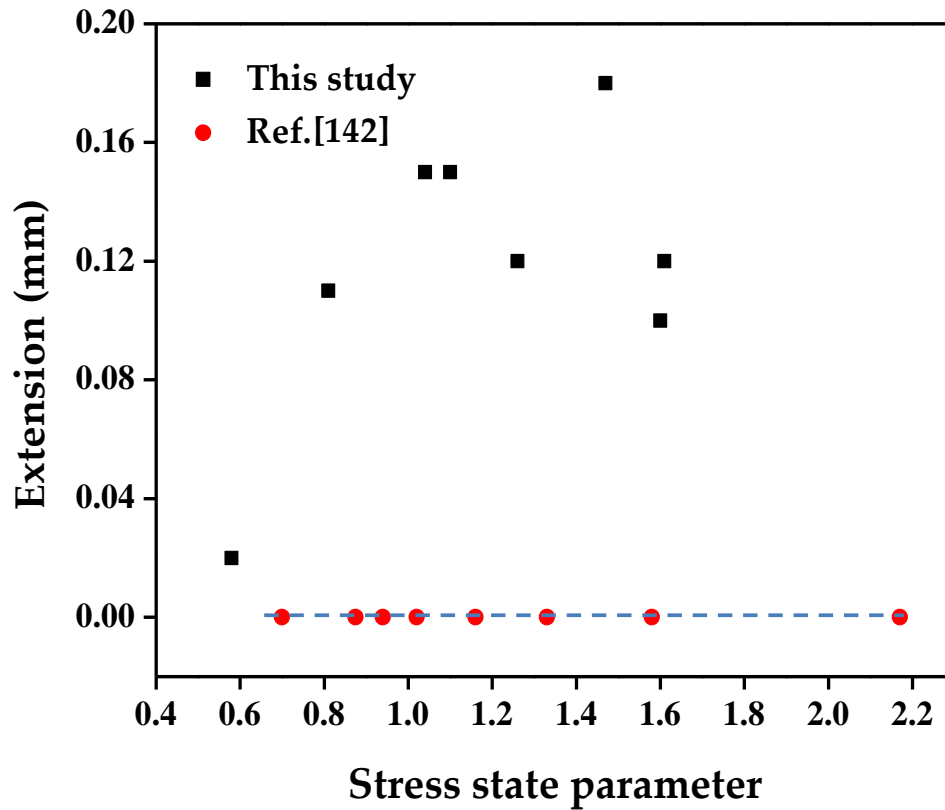


Figure 3.27 Extension as a function of stress state parameter

3.4 Conclusion

Through changing the geometries of the samples, deformation behaviors of BMG samples under tensile confinement condition have been systematically investigated, and tensile ductility has been achieved for various samples. The major conclusions can be drawn as follows:

- (1) In contrary to the negligible macroscopic ductility for BMGs at room temperature, BMGs under tensile confinement condition can exhibit large ductility. The highest ductility for the confined sample is up to

3. Achieving tensile ductility of BMGs at room temperature

~25 %, which is a record has never been reported before for BMGs at room temperature. Moreover, the concept of designing tensile confinement, i.e., intentionally notching or contouring a specimen, may open an avenue for the structural application of BMGs.

- (2) There is a clear transition from highly localized shear banding dominant deformation mode to homogeneous deformation mode as the confinement condition becoming more severe, i.e., decreasing notch angles or decreasing sample aspect ratios. This phenomenon is attributed to the delay of shear banding by controlling the resolved shear stress.

Chapter 4

4 Approaching ideal tensile strength of BMG

4.1 Introduction

High strength is a long-standing goal for structural materials and is the primary considering factor for engineering applications. The ideal strength, which is an important material property, refers to the upper bound of stress that a material can sustain without damage. The ideal strength of crystals has been studied extensively for years, and several reviews related to ideal strength have been documented [143, 144].

Generally speaking, the ideal strength of crystals is controlled by the energy required to break a bond by shear compared to that by tension. The ideal tensile strength is roughly $E/10$ [145, 146], where E is the Young's modulus. As regarding the ideal shear strength, the ground-breaking work was done by Frenkel [147], who calculated the theoretical shear strength by an assumption of cooperative shearing and obtained $\tau_{\text{ideal}} \approx G/5$, where G is the shear modulus. However, most metals plastically deform at the stress of 3-4 orders of magnitude lower compared with their ideal strength. The large discrepancy between the ideal strength and the testing strength motivated the theory of dislocation [148, 149]. For metals, shear modulus is smaller than Young's modulus, and thus metals always fail by shearing. On the contrary, for ceramics, shear modulus is larger than Young's modulus, and thus ceramics always fail by tension [150]. The schematic map of ideal strengths for metals and ceramics is shown in **Figure 4.1**.

Unlike the conventional metals, the recently emerging BMGs have unique mechanical properties. For example, BMGs have high yield stress and high elastic limit as compared to their crystalline counterparts. All BMGs fail at an elastic limit of 2%, corresponding to strength of $\sim E/50$ [49]. The failure mode for BMGs at low temperature ($<T_g$) is shear banding, which is a process of localization of plastic strain during deformation. Based on the analysis in section 3.1, shear stress can be tuned to be below the critical shear stress, and

then tensile stress dominates. As such, BMG sample can fail by tensile mode by suppressing shear banding. Then the questions for BMGs are: What is the tensile fracture strength? As there are no defects such as dislocations in monolithic BMG, is the measured tensile strength close to the ideal tensile strength? What is the fracture morphology for BMG fail under tensile mode?

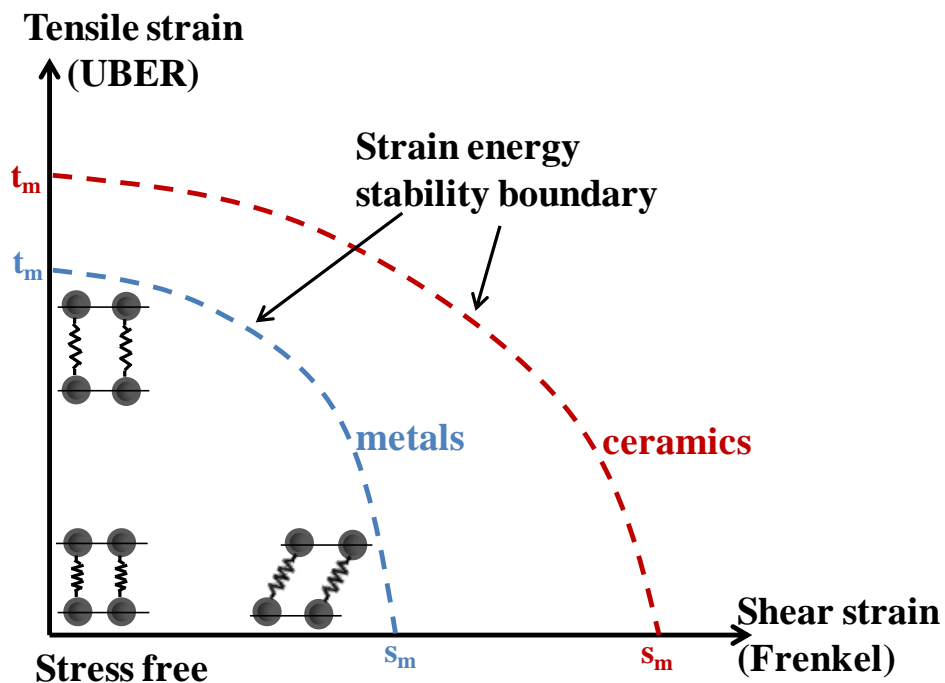


Figure 4.1 Schematic map of material ideal strengths for metals and ceramics. The blue and red dashed lines showing the boundary of strengths for metals and ceramics, respectively. s_m and t_m denote the maximum shear and tensile strength of a perfect crystal, adapted from [150].

In this Chapter, the tensile fracture strength of BMG samples with various geometries is investigated, and compared with the ideal tensile

strength. The fracture morphology of BMG under tensile confinement is also presented.

4.2 Results and discussion

4.2.1 Variation of tensile stress as stress state parameter

The tensile stress as a function of stress state is shown in **Figure 4.2**, some data points collected from reference are also shown for comparison [142]. The tensile stress is defined as the maximum stress obtained from the stress-extension curve. The tensile stress shows an increasing trend as the stress state increases, and the maximum tensile stress is about 3.6 GPa at the stress state of 1.6, which is about 2.3 times higher than that obtained in uniaxial test. The minimum stress is about 1.6 GPa, which is comparable to the stress under uniaxial tension for this material. As further increasing the stress state, the tensile stress slightly decreases. On the contrary, the tensile stress from the reference shows a decreasing trend as the stress state increases, which is totally different from our work.

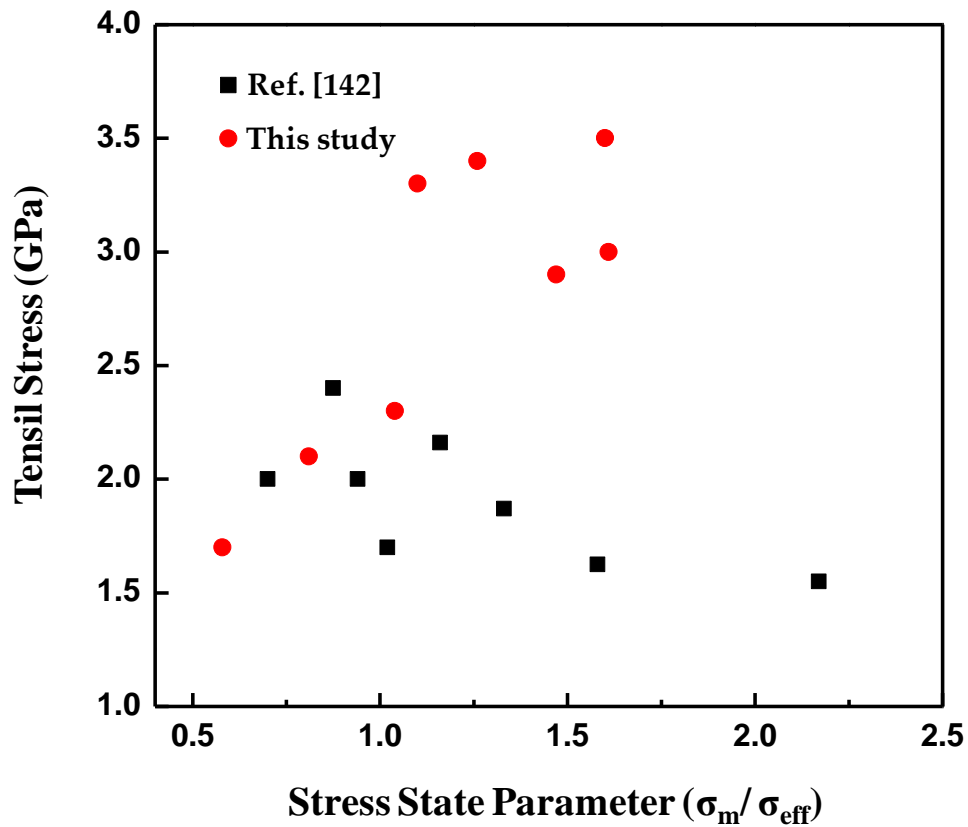


Figure 4.2 Tensile stress as a function of stress state parameter

4.2.2 Approaching ideal tensile strength

Figure 4.3 shows the correlation between fracture strength and Young's modulus. For crystalline metals, the fracture strength is approximately 0.65 % of the modulus. For metallic glasses tested under non confinement condition, the fracture strength is about 2 % of the modulus. For our study, the strength of this Zr-based BMG is about 5 % of its modulus, which is very close to the strength of perfect crystal (whiskers), putting BMG among the highest strength materials.

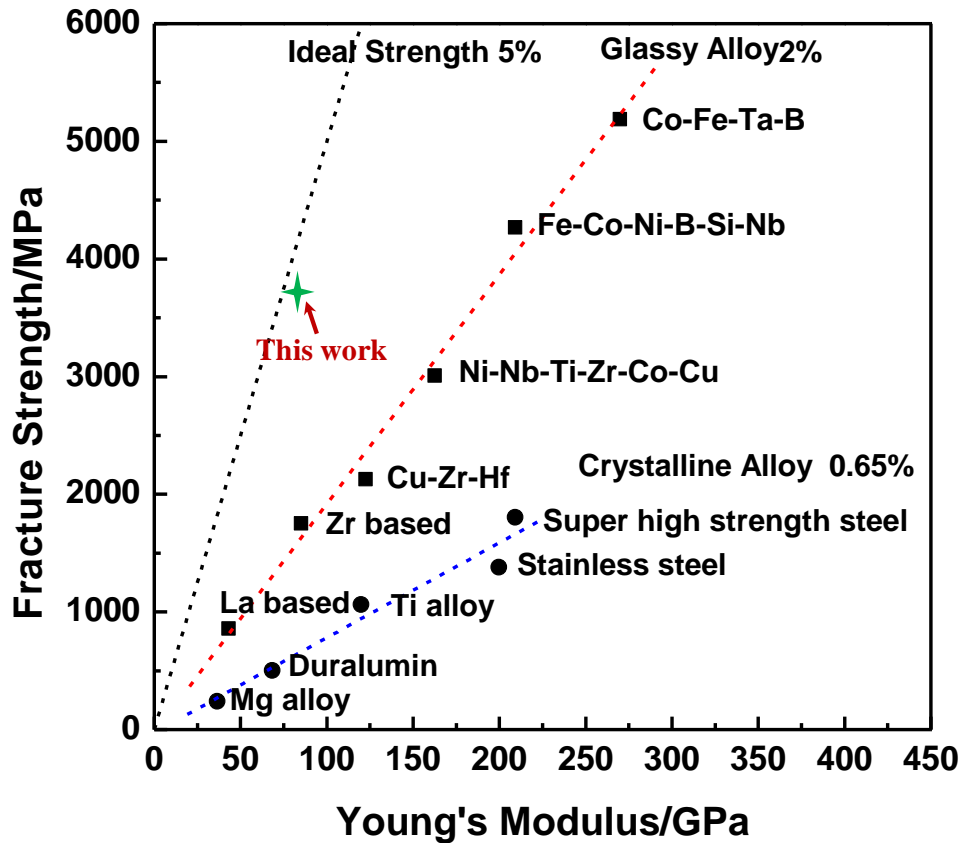


Figure 4.3 Correlation between fracture strength and Young's modulus. The data in this work is tested under tensile confinement condition. The data for crystalline materials are also shown for comparison [4].

The ideal strength of a material is in principle related to the cohesive forces between atoms. In general, high cohesive forces are associated with large elastic constants, high melting points, and small coefficients of thermal expansion. Under tension, the atomic distance in the loading axis is larger than the initial value a_0 , while the atomic distance normal to the loading axis is smaller than a_0 . When the strength reaching the maximum tensile strength,

the atomic bond breaks and leaves the fracture surface. The cohesive force as a function of the separation between atoms is illustrated in **Figure 4.4**.

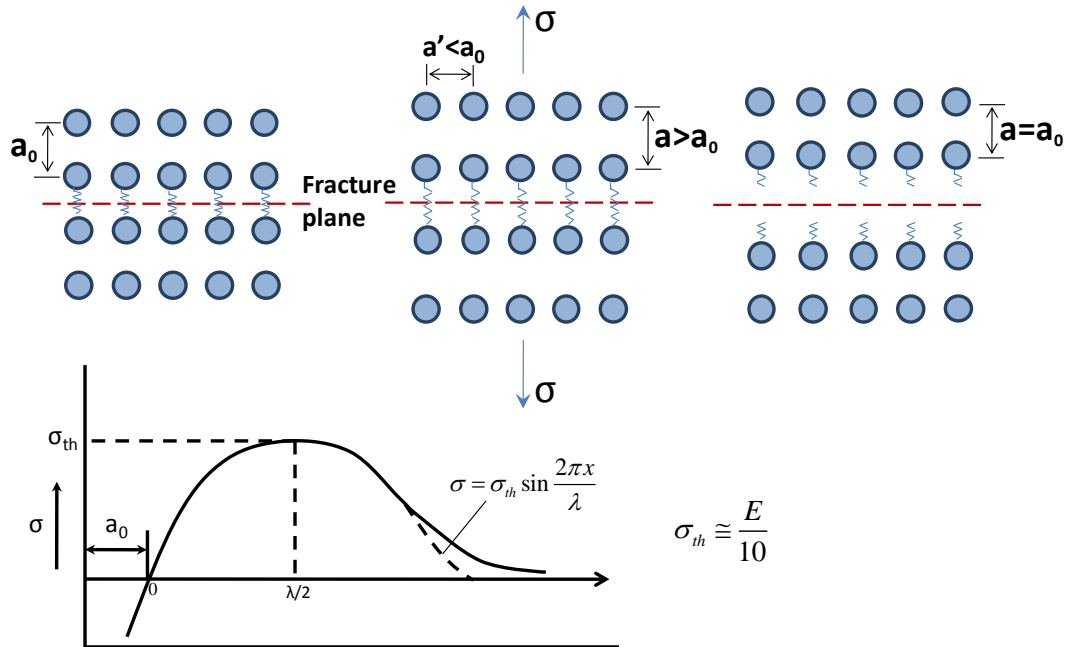


Figure 4.4 Atomistic model of ideal tensile strength.

If assuming that the cohesive force curve is a sine curve, the estimated ideal tensile strength would be $\sim E/10$. The real expression for the cohesive force curve can be more complicated, therefore, a good approximation of the ideal tensile strength is in the range of $E/10 \sim E/20$.

However, engineering materials typically have fracture stresses that are 10 to 1000 times lower than the theoretical value. The first explanation of the discrepancy between the observed fracture strength and the theoretical cohesive strength was proposed by Griffith [151]. Griffith proposed that a material contains a population of pre-existing cracks which produces a stress

concentration so that the theoretical cohesive strength is reached in localized region whereas the nominal stress is well below the theoretical value. In this work, Griffith theory is adopted to calculate the intrinsic defect in BMGs. Based on Griffith's theory, the fracture strength is:

$$\sigma_f = \left(\frac{E\gamma_s}{4c} \right)^{\frac{1}{2}} \quad (4.1)$$

where γ_s is the surface energy, E is Young's modulus, c is half crack length.

On the other hand, the theoretical cohesive strength can be expressed as :

$$\sigma_{\max} = \left(\frac{E\gamma_s}{a_0} \right)^{\frac{1}{2}} \quad (4.2)$$

where γ_s is the surface energy, E is Young's modulus, a_0 is interatomic distance.

It is generally known that the basic plastic flow carrier of metallic glass is cooperative shearing of atomic clusters termed as shear transformation zones (STZs) [43, 61, 152-154]. In analogy to concept of the pre-exist cracks, we assume that the size of STZ is comparable to that of the pre-exist crack. Recently, it is reported by Pan et al. [155] that the STZ size is experimentally estimated to be 1.3-1.9 nm by nanoindentation method. Besides, simulational works have also been carried out and predicted the size of solute-centered

clusters to be 1-1.5 nm [156, 157]. Based on these previous studies, we estimate the averaged STZ size in our study is to be ~1 nm. According to equation (4.1) and (4.2), taking $E=78$ GPa [97], $a_0=0.4$ nm, $2c \approx 1$ nm, the calculated maximum tensile strength is 3.5 GPa, which exhibits a fair agreement with the our measured maximum value.

Table 4.1 Experimentally measured ultra-high strengths in metals.

Material	Max Elastic strain (%)	Measured Strength (GPa)	Ideal Strength $-E/10$ (GPa)	Sample Size	Method of Testing	Ref.
Fe	4.9	13.1	21	1.6 μm	Tension	[158]
Cu	2.8	2.9	11	1.3 μm	Tension	[158]
Ag	4.0	1.7	8	3.8 μm	Tension	[158]
Au	1.9	1.5	8	1.4 μm	Tension	[158]
Zn	2.0	2.2	11	1.0 μm	Tension	[158]
Ag-NW	9.1	7.3	8	16.5 nm	Bending	[159]
Au-NW	7.0	5.6	8	40 nm	Bending	[160]
Au-NP	0.8	0.8	8	300 nm	Compression	[161]
Au-NP	0.4	1	8	300 nm	Compression	[162]
$\text{Cu}_{49}\text{Zr}_{51}$	4.4	3.8	8.3	200 nm	Tension	[163]
$\text{Zr}_{64.13}\text{Cu}_{15.75}$ $\text{Ni}_{10.12}\text{Al}_{10}$	5	3.7	7.8	~ 2.5 mm	Tension	This work

Such high strength phenomena are usually reported in small size samples (nanometer scale) and defect free samples, for example metallic whiskers. In our study, we show that even in bulk sized samples, the ideal tensile strength can be reached. **Table 4.1** summarizes the experimentally measured ultra-high strengths in metals [158-163].

4.2.3 Fracture morphology under tensile confinement

Fracture morphology is a useful method to determine if the material is brittle or ductile, and is important for investigating the fracture process of materials. The fracture morphology of samples with various notch shapes will be present in this section.

Figure 4.5 shows the representative fracture morphology of 120° circumferentially-notched sample. It can be seen that most of the fracture surface morphology is the feature of shear, suggesting shear banding is the dominant failure mode. However, some 'dimple like' structure is found in the center of the sample, which is shown in the higher magnification image in **Figure 4.5 b)**. The typical fracture morphology for BMGs in tensile test is 'cores' and some 'ridating veins'. Such 'dimple' structure is rare to see for BMGs in tensile test, indicating this material is more ductile under confinement condition.

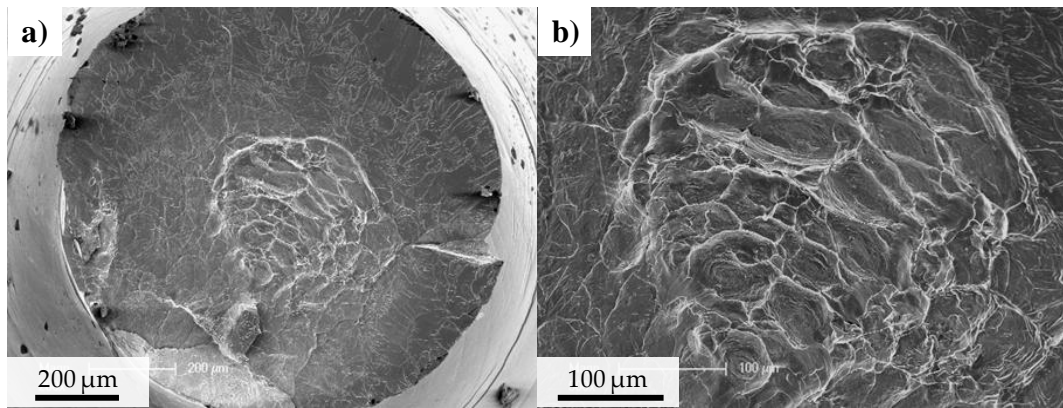


Figure 4.5 Representative fracture morphology of circumferentially-notched sample with a notch angle of 120° .

Representative fracture morphology of the circumferentially-notched sample with notch angle of 90° is shown in **Figure 4.6**. As the notch angle decreases, the fracture surface becomes flat, and once again, the ‘dimple-like’ structure is found in the center, and the ratio of the ‘dimple-structure’ area is slightly increased as compared with that of 120° sample. Another feature need to be emphasized is that some cracks (as indicated in **Figure 4.6 b**) are found in this sample, which is not seen in the 120° sample. The size of the dimple structure is about $30\ \mu\text{m}$, as indicated in **Figure 4.6 c**).

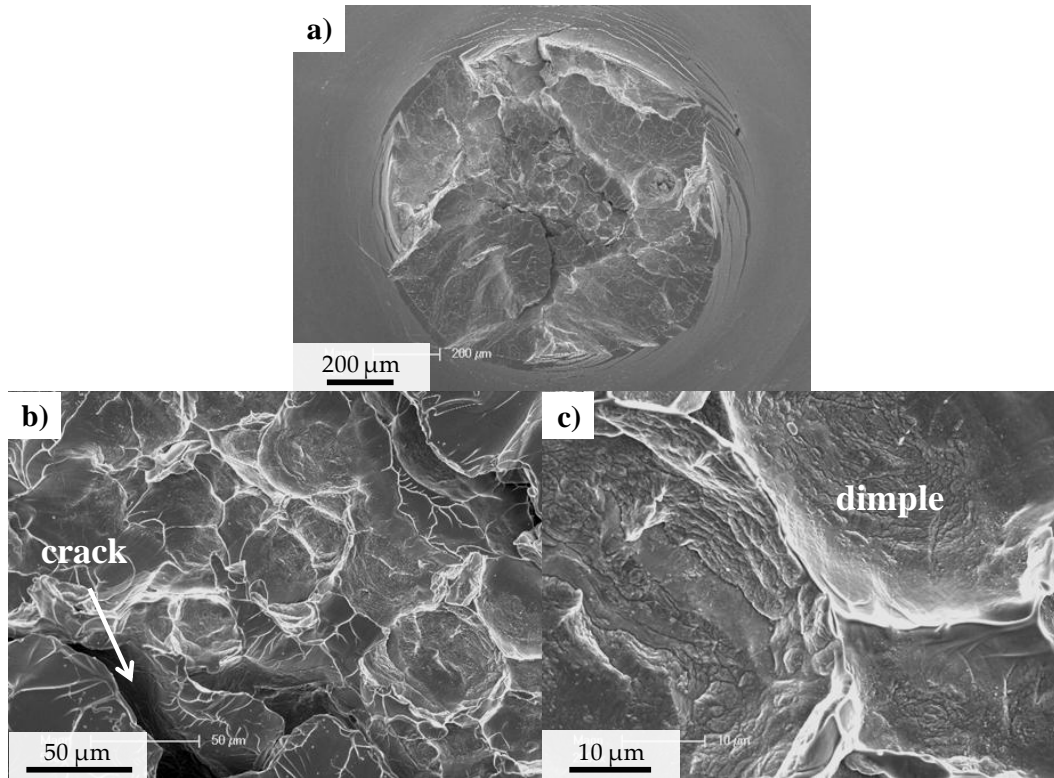


Figure 4.6 Representative fracture morphology of circumferentially-notched sample with a notch angle of 90° .

Figure 4.7 shows the representative fracture morphology of the circumferentially-notched sample with notch angle of 45° . When the notch angle decreases to 45° , a large number of cracks are found in the center of the sample, strongly indicating a different fracture mode as compared with the shear banding dominant fracture mode. Besides, a transition from tension to shear is detected (as shown in **Figure 4.7 b**), which is a direct evidence for the changing of fracture mode from shear banding to tension. We speculate that the 'dimple-like' structure is the initial site of crack formed by debonding of atoms, and followed by shearing. Furthermore, some melting droplets are found in the vicinity of tension region, indicating a large heat releasing during

the fracture. All these unusual features, such as cracks, transition zone, melting droplets, strongly indicate that tension, instead of shear banding, is the dominant fracture mode under tensile confinement.

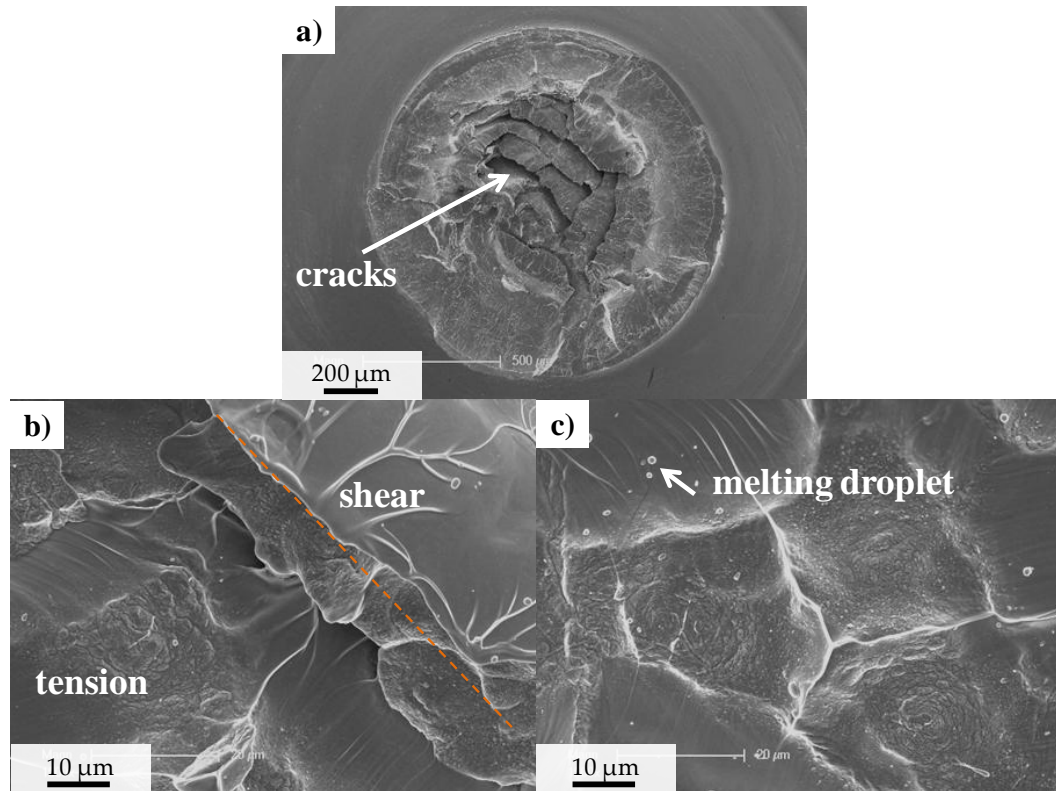


Figure 4.7 Representative fracture morphology of circumferentially-notched sample with a notch angle of 45° .

Figure 4.8 shows fracture morphology of slit-notched samples with various aspect ratios. **Figure 4.8 a), b)** show the fracture morphology of 2:1 sample. The fracture morphology of 2:1 sample consists of two distinct zones, i.e., the smooth zone followed by the zone with cores and radiating veins. The smooth zone, which is $\sim 74 \mu\text{m}$ in width, is considered to be the initial stage of the plastic deformation. Compared with the reported smooth zone ranging

from sub-micrometers to a few tens of micrometers in width, the current zone size is reasonable. These features, which are consistent with those of uniaxial tension test, indicate the fracture mode of 2:1 sample is shear banding. The fracture morphology of 1:1 sample is shown in **Figure 4.8 c) and d)**.

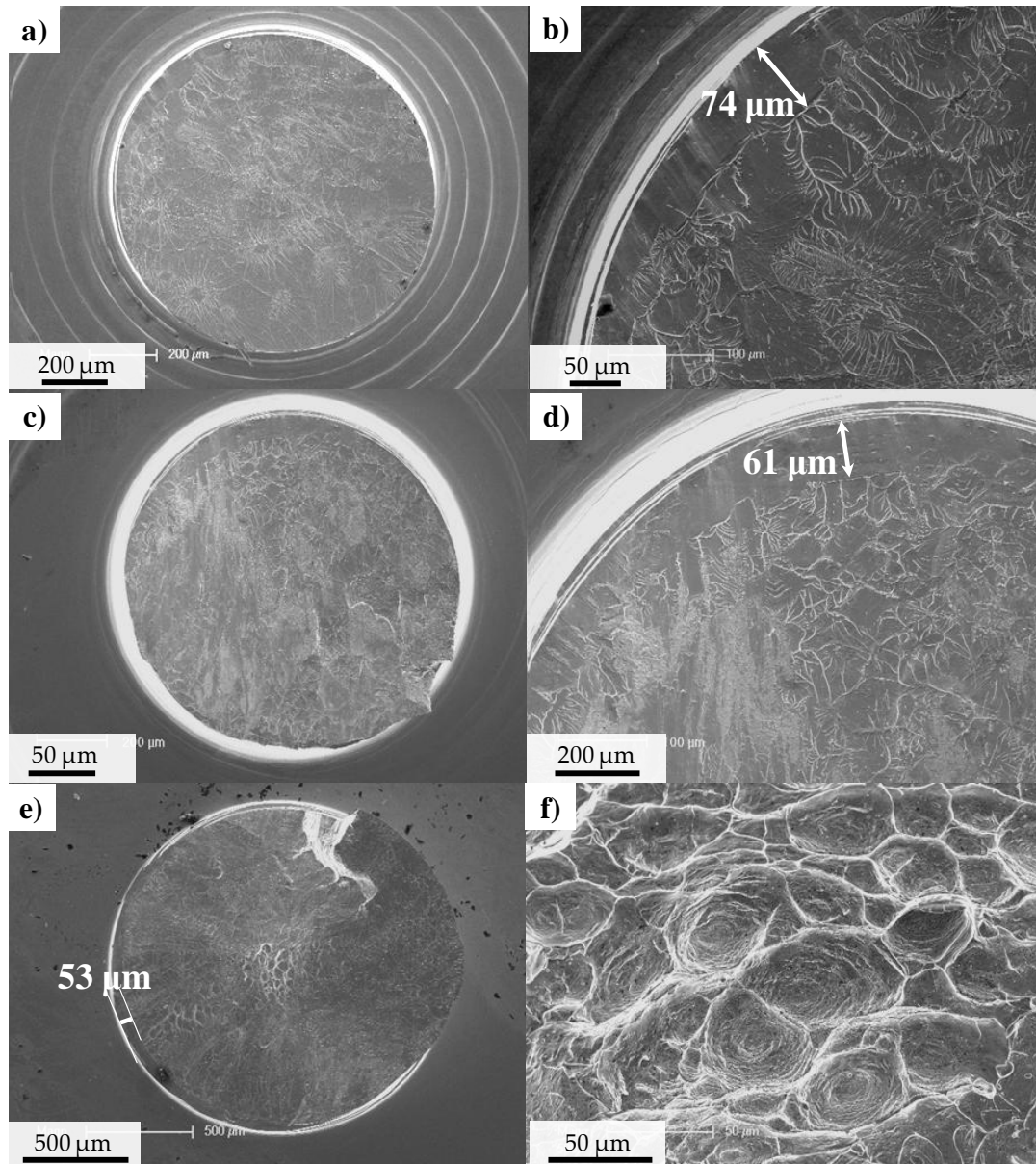


Figure 4.8 Fracture morphology of slit-notched samples with various aspect ratios. a) b) aspect ratio 2:1, c) d) aspect ratio 1:1, e) f) aspect ratio 0.5:1.

The width of the smooth zone is $\sim 61 \mu\text{m}$. The feature of cores and radiating veins becomes faint as compared with that of 2:1 sample. As decreasing the aspect ratio to 0.5:1, the width of the smooth zone further decreases to $\sim 53 \mu\text{m}$, and the feature of cores and radiating veins is hard to identify. Interestingly, the 'dimple-like' structure is found in the center of the sample, which is analogous to that found in the circumferentially-notched samples, indicating a more ductile fracture behavior of the 0.5:1 sample.

Figure 4.9 shows the representative fracture morphology of the 5 mm cylindrical sample with Bridgman notch. Cracks can also be found, as shown in **Figure 4.9 b)**. Moreover, some micro-voids as well as some melting droplets are found in the vicinity of the 'dimple like' structure. These melting droplets indicate a large amount of heat is released when the sample breaks.

Based on the above results, some unique features are found in the fracture morphology of BMGs under tensile confinement condition. First, there is a clear transition from shear dominant fracture mode to tensile dominant fracture mode as the stress state parameter increasing. Second, 'dimple-like' structure which is usually an indication of ductile fracture, can be found in this BMGs. Third, cracks and micro-voids are also found in the fracture surface. These features prove that the nature of this BMG under tensile confinement condition is ductile fracture

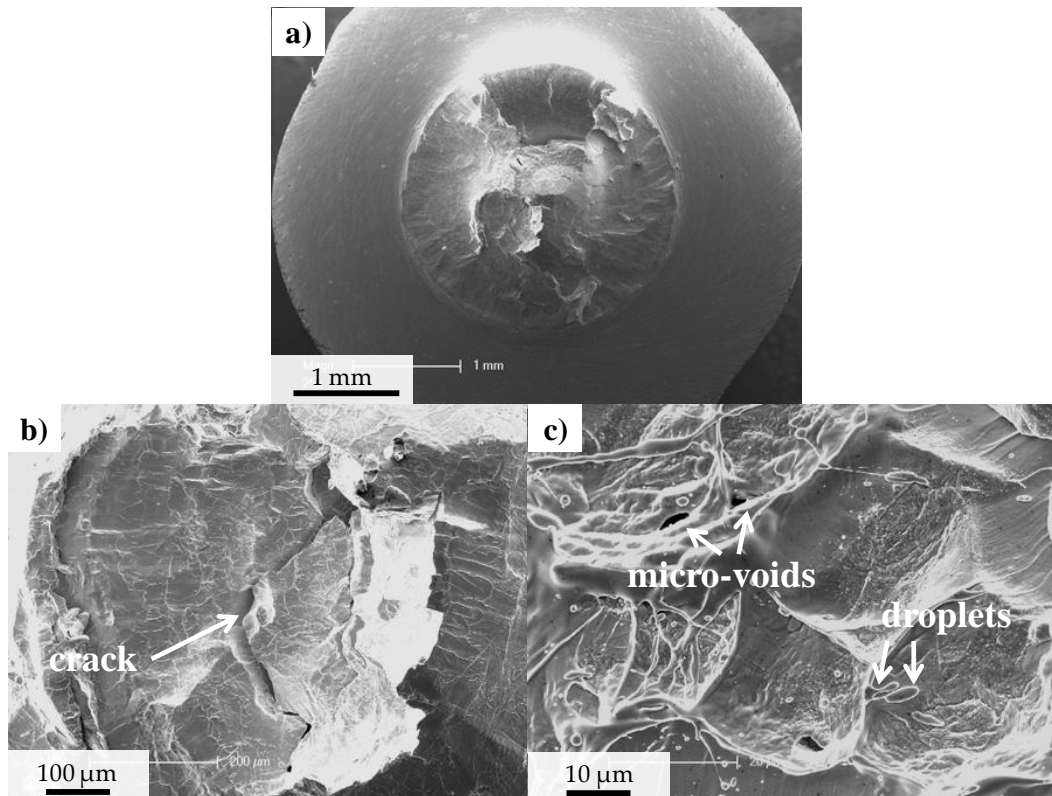


Figure 4.9 Representative fracture morphology of the 5 mm cylindrical sample with Bridgeman notch.

4.3 Conclusion

By suppressing shear stress, the tensile strength and fracture morphology of BMG under tensile confinement condition have been systematically studied. The most salient conclusions can be drawn as follows:

- (1) The tensile strength of BMG under confinement condition shows an increasing trend as the stress state parameter increases, which is in contrary to the previously reported results. The maximum tensile

strength that had been achieved in this work is up to 3.6 GPa, which is 2.3 times higher than that obtained under uniaxial tension.

- (2) Unlike the fracture features of uniaxial tension where smooth zone and the zone with cores and radiating veins can be found, several unique features have been found in the fracture morphology of BMG under tensile confinement condition, such as micro-voids, cracks, and 'dimple-like' structures. These features strongly indicate that this 'strong-yet-ductile' BMG becomes 'stronger-and-ductile' under confinement condition.
- (3) Based on Griffith's theory, the calculated tensile strength of this BMG is about 3.5 GPa, which is very close to the value obtained by our experiment. The ultimate tensile strength is $\sim E/20$, which is approaching the ideal tensile strength, putting BMG among the highest strength materials.

Chapter 5

5 Strain hardening and densification in metallic glass

5.1 Introduction

It is well known that metallic glasses shear off catastrophically within a narrow region (~100 nm) which is named shear band, at room temperature right after the initial ~2% elastic limit [49]. It is this shear banding that dominates the deformation behaviour, such as brittleness without any macroscopic plastic strain. Deformation of metallic glasses through shear banding always leads to softening [73, 103], whether it is at room temperature or at ambient temperature. This is because metallic glasses deform through a

localized shear on the plane of maximum stress (~45 degree to the loading direction) due to isotropic nature of the structure of metallic glasses [52, 137]. Shear banding is a highly inhomogeneous and softening process usually in a catastrophic manner where free volume will only increase [31]. Thus softening associated with shear banding is regarded as a natural phenomenon in metallic glasses.

On the other hand, even within the shear band, softening is the dominate mechanism, as severe plastic deformation causes dilatation by the increase in free volume. The mechanism of strain softening has been attributed to temperature rise [73] or strain caused dilatation [164] within shear band. Although its mechanism remains debatable, the softening itself is a commonly observed phenomenon. So as a whole, all the deformation behaviour of metallic glasses is dominated by the shear banding, and softening is brittle behaviours are the key phenomenon. It is this softening and lack of the capability of strain hardening hinders the application of BMGs as engineering materials.

However, due to the isotropic nature of metallic glass, the maximum shear stress can be geometrically constrained (as presented in **Chapter 3**) and the catastrophic failure of metallic glass can be bypassed. Therefore, under the condition that shear banding is constrained, delayed or even eliminated, metallic glasses like any other materials may in principle, exhibit radically

different deformation behaviour, and other deformation mechanisms can appear.

In this chapter, for the first time in a tensile constrained mm-sized bulk specimen where the shear banding is constrained, we demonstrate homogeneous deformation at room temperature, leading to strain hardening and densification. Such hardening is attributed to densification (e.g. free volume annihilation) in the specimen due to stress induced annealing at room temperature. Such a discovery provides totally fresh angle for the interpretation of mechanical behavior of metallic glasses and helps us to understand the true deformation behaviour, and design of better structure for engineering application of metallic glasses.

5.2 Results

5.2.1 Strain hardening characterized by micro hardness

In this section, samples were fabricated with different geometries for compression, tension and annealing test. For better illustration, the geometries of these samples are listed in **Table 5.1**.

Table 5.1 Geometries of the samples for compression, tension and annealing tests.






Samples	Geometries
2:1 compression	
1:1 compression	
2:1 tension	
1:5 tension	
Annealed samples for hardness test	

Figure 5.1 shows the stress-strain curves of BMG samples under compression and tension with varied aspect ratios. **Curve 1** is the compressive curve of a 2:1 sample. It shows that the sample yields at about 1.6 GPa, followed by serrated flow corresponding to a characteristic negative slope of in the stress-strain curve.

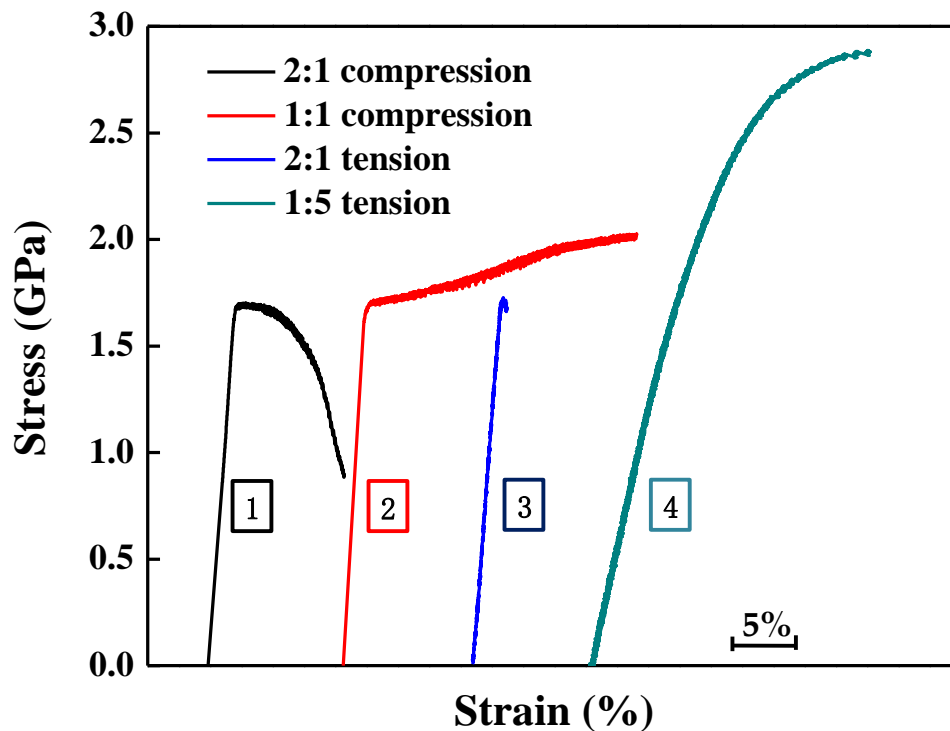


Figure 5.1 Stress-strain curves of BMG samples under compression and tension with different aspect ratios.

Curve 2 is the compressive curve of a confined sample with aspect ratio 1:1. For this confined sample, it shows a ‘strain hardening’ like behavior after yielding, which is caused by the increase of contact area during plastic deformation. If corrected by the true area, there will not be the strain hardening behavior. **Curve 3** is the tensile stress strain curve of a sample with aspect ratio 2:1. In analogy to the tensile behavior of uniaxial tension, this BMG sample shows negligible tensile ductility and fails catastrophically after yielding. **Curve 4** is the curve for sample under tensile confinement condition. In sharp contrast with the three curves presented above, it shows an obvious strain hardening behavior after yielding at about 1.8 GPa, and the stress

further increases to about 2.8 GPa. This strain hardening behavior is like that of a ductile material, which has never been reported in BMGs.

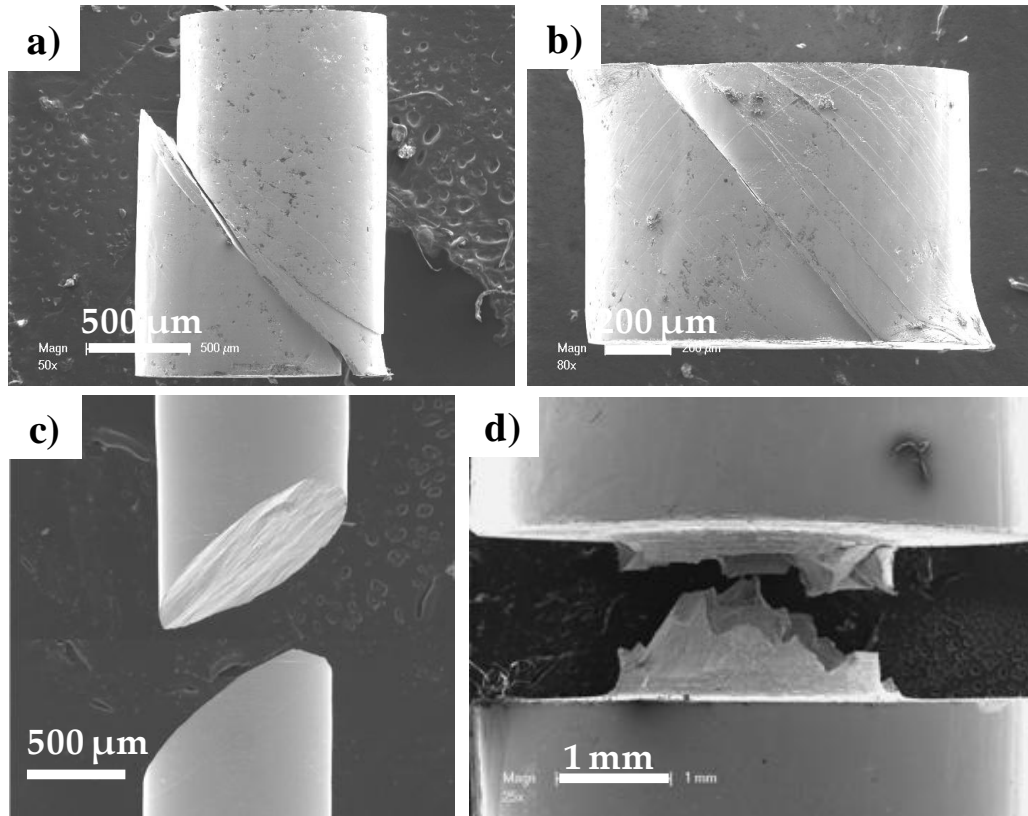


Figure 5.2 SEM images showing the side view of BMG samples after fracture. a) compression 2:1 sample, b) compression 1:1 sample, c) tension 2:1 sample, d) tension 1:5 sample.

Figure 5.2 shows the SEM images of the side view of BMG samples after fracture. **Figure 5.2 a)** shows the SEM image of 2:1 sample in compression. This sample fails along a dominant shear band, about 45° with respect to the loading axis. As shown in **Figure 5.2 b)**, the 1:1 sample has multiple shear bands and also fails along one dominant one. The left top corner and lower right corner show the sign of area increase due to contact with the cross head

of the testing machine. **Figure 5.2 c)** shows the fracture of 2:1 sample under tension, indicating no macroscopic tensile ductility. **Figure 5.2 d)** shows the SEM image of 1:5 tensile sample. This sample exhibits completely different fracture behavior as compared to other samples, and no obvious shear bands can be found. The fracture process of this sample can be found in section 4.2.3.

The hardness of the plastically deformed area was studied by microhardness testing. **Figure 5.3** shows the hardness traces of undeformed sample, deformed samples (2% and 7%).

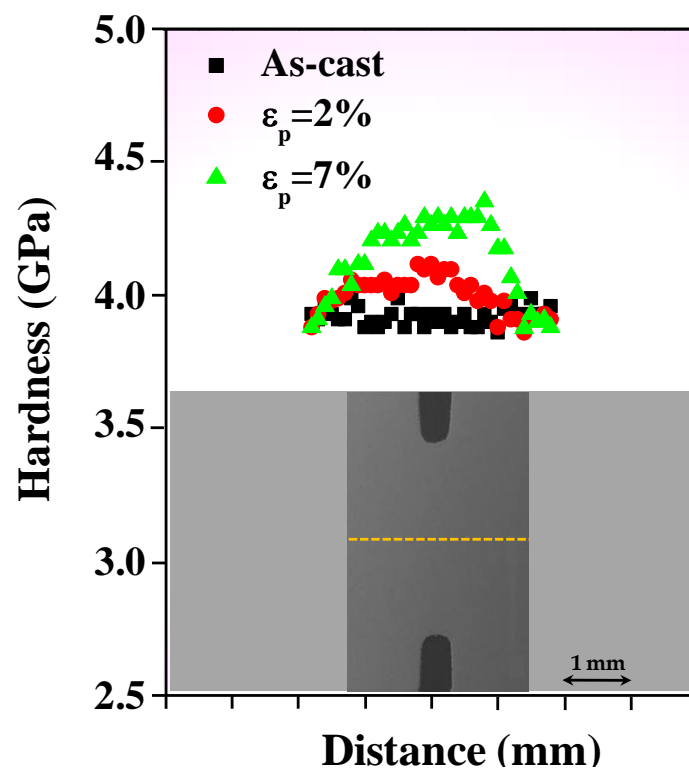


Figure 5.3 Microhardness traces of the plastically deformed samples with different permanent strain. The inset shows the trace of hardness measurement.

To rule out the influence of notch on microhardness, the undeformed sample (as-cast) for microhardness testing is fabricated exactly as that prepared for notched samples. The microhardness for as-cast sample is constant (around 400 kg/mm²) across the thin disk, proving no influence of the notch shape on microhardness. However, the deformed specimens show peak hardness right at the centre and gradually decline to the level of the as-cast sample. The jump in peak hardness of 12% is highest for the 7% deformed, while the peak hardness was 5% for the 2% deformed sample. This is another indication of strain hardening. It is noticed that the hardened area goes beyond the thin disk at the center, indicating that the plastically affected body is actually much beyond the actual narrow disk of the tensile specimen. The fact that there is a hardness peak in the centre also indicates that the deformation is more severe at the center and progressively declines and the affected volume is actually in a diamond-like shape.

It is well known that thermal annealing (sub- T_g) leads to structural relaxation in BMGs, and induces a hardness increase. Therefore, for comparison, the microhardness testing was also conducted for annealed samples. All the samples were prepared the same procedure as that for the tensile testing, and subsequently annealed for 30 mins at 473 K, 523 K, and 573 K, respectively. **Figure 5.4** shows the microhardness traces of annealed samples. In consistent with the as-cast samples, no hardness increase is found

inside or near the notch zone. The averaged microhardness for samples annealed at 473 K, 523 K, and 573 K are 409 HV, 423 HV, and 432 HV, respectively, showing an increasing trend as the annealing temperature increases.

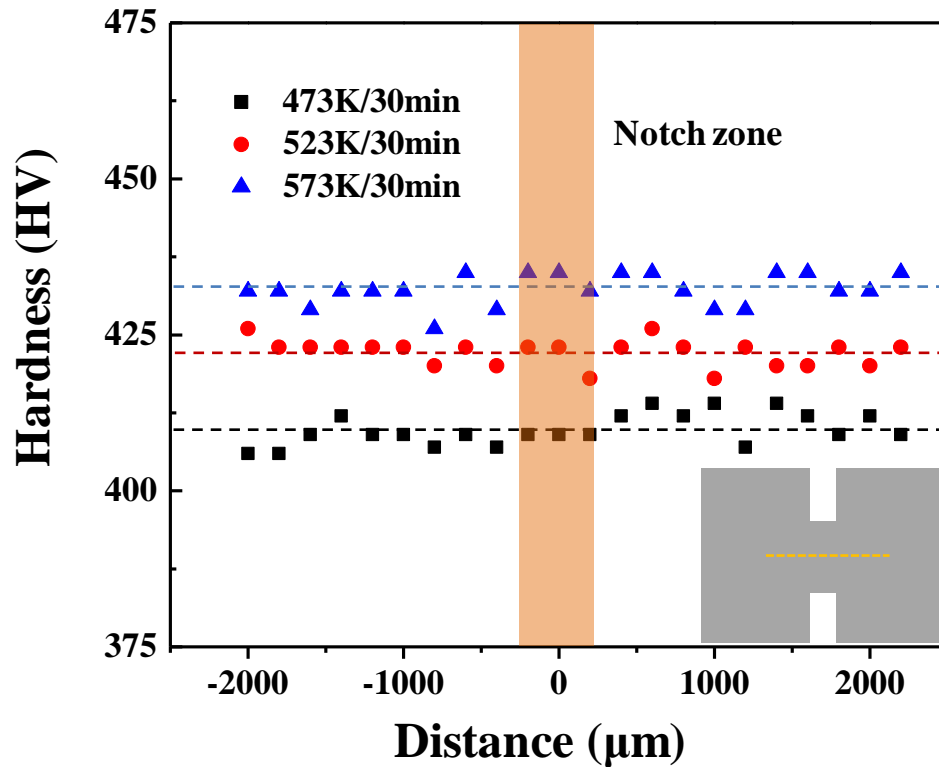


Figure 5.4 Microhardness traces of the annealed samples.

Figure 5.5 shows the SEM images of indent morphologies. Figure 5.5 a) shows the morphology of an indent located 2 mm away from the center of a 7% plastically deformed sample. Since this region is far away from the notch, and the stress level during tensile testing is within the elastic limit of this BMG, this indent can be treated as the hardness of undeformed or as-cast sample. However, the indent in the center of deformed notch (as shown in Figure 5.5

b)), is smaller than the undeformed one, strongly indicating a hardness increase in the notch region. In addition, a large number of pile-ups are found around the indent. For the annealed sample (as shown in **Figure 5.5 c)**), pile-ups can also be found but less than those found in deformed sample. The size of indents measured by SEM and the tested hardness values are mutual agreement.

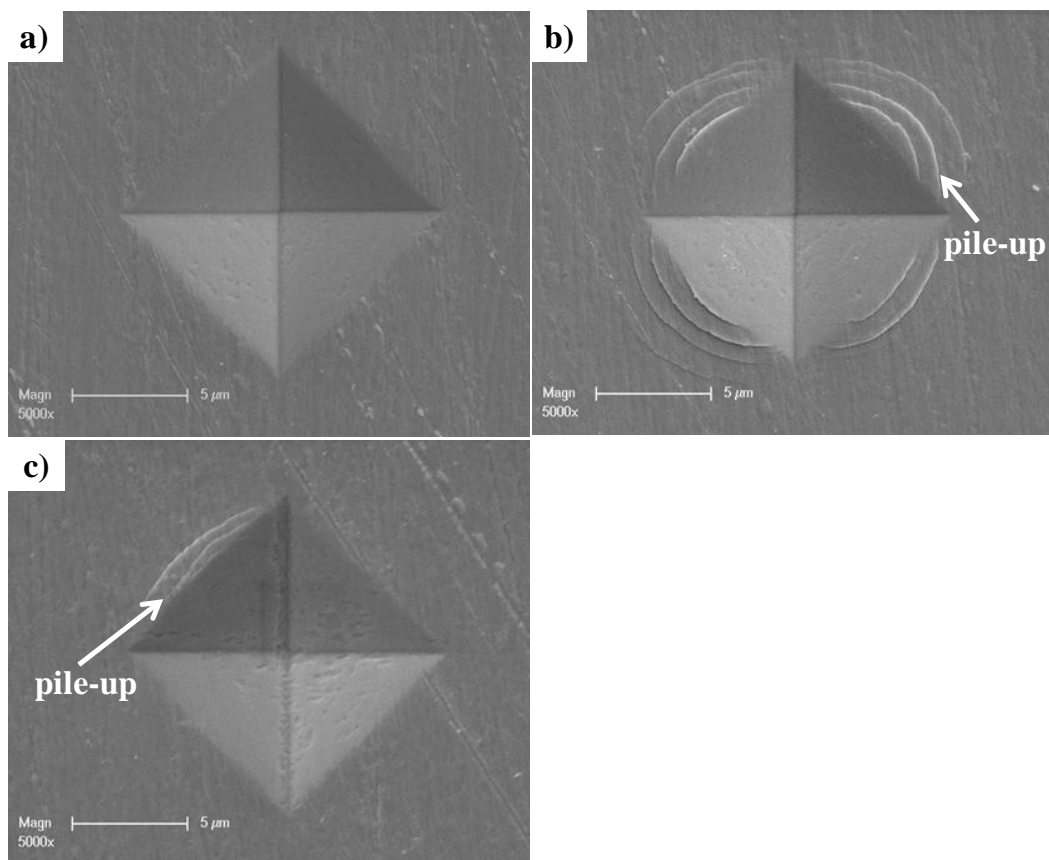


Figure 5.5 SEM images of the indent morphology. a) 2 mm away from the center of a 7% plastically deformed sample, b) center of the corresponding 7% plastically deformed sample, c) 573 K annealed sample.

5.2.2 Densification characterized by DSC

In order to investigate the reasons for the hardening after homogeneous deformation, samples experienced different amount of plastic deformation were subjected to DSC study. Since all the samples are prepared from the cylindrical rod shape, there is a gradient of structural change from the center to the outer surface of the sample induced by different cooling rate. To rule out the influence of cooling rate induced structural difference, the DSC result of a deformed sample is compared with that of an undeformed reference with the same diameter. The morphologies of the deformed sample and undeformed sample for DSC testing can be seen in **Figure 5.6**.

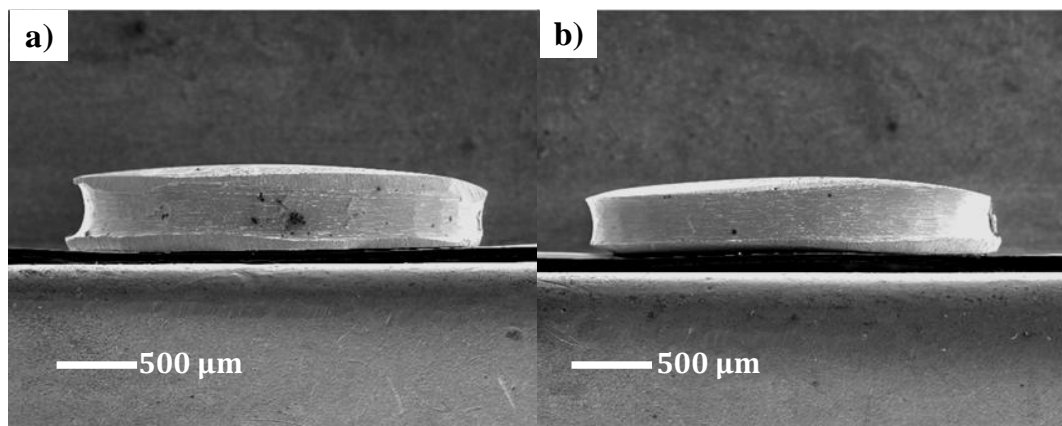


Figure 5.6 SEM images of the samples for DSC testing. a) a plastically deformed sample, b) an undeformed reference.

Figure 5.7 shows the DSC curves of as-cast, deformed samples and annealed samples. The corresponding thermal properties measured by DSC are summarized in Table 5.2.

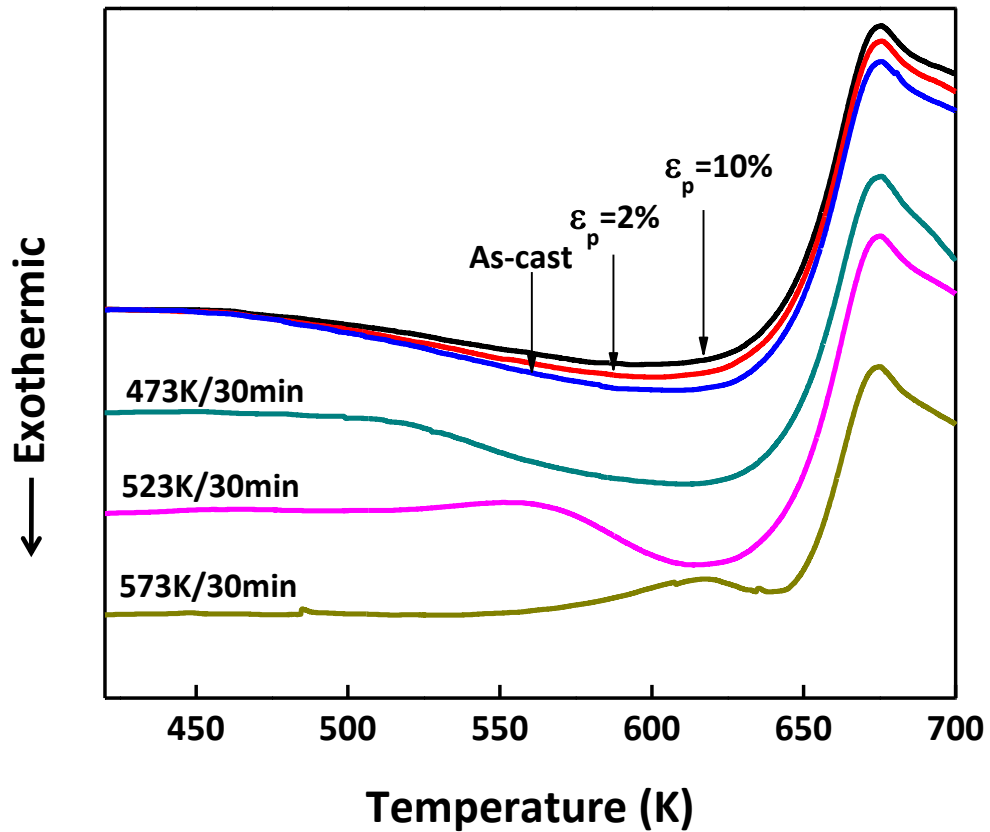


Figure 5.7 DSC curves of the plastically deformed and annealed samples.

Results show the *reduction* in exothermic heat as plastic deformation increases, instead of an *increase* usually seen in the plastically deformed samples. For the annealed samples, the relaxation enthalpy also decreases as the annealing temperature increasing. It has been reported by Slipenyuk and Eckert that the relaxation enthalpy before the glass transition region is

proportional to the annihilation of excess free volume [165]. The relaxation enthalpy decreases to 5.9 J/g and 4.4 J/g for the 2% and 10% plastically deformed samples. This is a strong indication of free volume reduction (densification) in the sample due to plastic deformation, which is in sharp contrast to free volume increase due to plastic deformation studied before [139, 166, 167]. To the best of our knowledge, such densification of BMG induced by tensile stress has never been reported before. The free volume reduction is consistent with the hardness measurement.

Table 5.2 Thermal properties of the as-cast, annealed and plastically deformed samples corresponding to Figure 5.7.

Sample	T_g (K)	ΔH_r (J/g)
As-cast	646	7.1
473 K/30min	646	4.8
523 K/30min	647	2.4
573 K/30min	653	0.08
$\epsilon_p=2\%$	646	5.93
$\epsilon_p=10\%$	646	4.4

Figure 5.8 shows the variation of normalized relaxation enthalpy and Vickers hardness as a function of plastic strain. The normalized relaxation enthalpy exhibits a decreasing trend as the plastic strain increases, while the hardness exhibits an increasing trend. Such correlation between relaxation

enthalpy and hardness with plastic strain is radically different from the previous studies, where strain softening is usually observed [168-171]. The results strongly suggest that strain induced hardening and densification are the dominant phenomena.

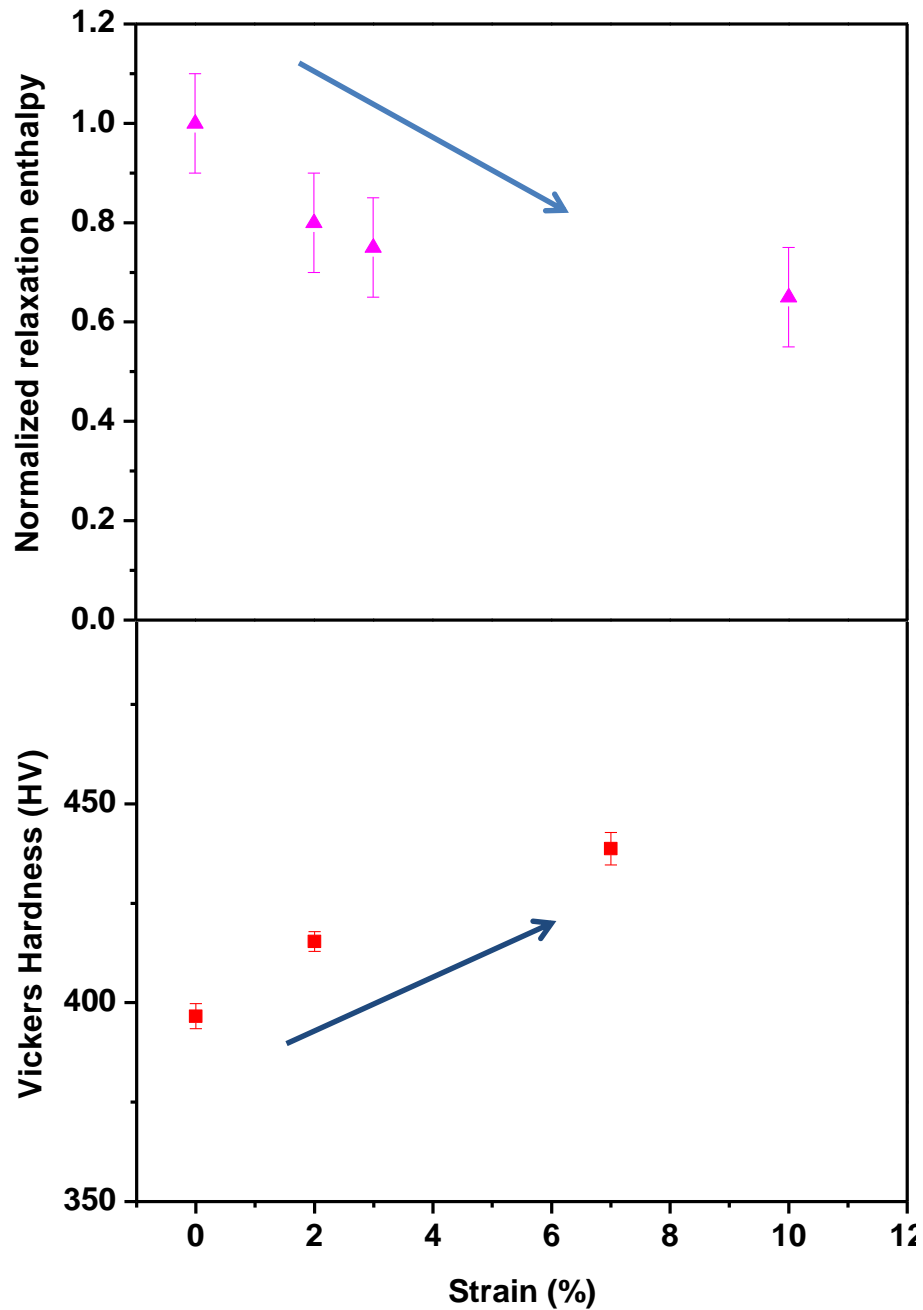


Figure 5.8 Variation of Normalized relaxation enthalpy and Vickers hardness as a function of plastic strain.

5.3 Discussion

5.3.1 The possibility of crystallization of BMGs during plastic deformation

BMGs generally fail in a brittle manner without any macroscopically ductility under quasistatic tensile loading at room temperature [53]. So far, significant tensile ductility has been reported only for small scale samples (around 100 nm) [104, 172, 173], and no mechanisms for strain hardening have been established. For the small samples, Deng et al. demonstrated that nano sized crystals were detected during the plastic deformation [172]. On the other hand, Pauly et al. recently reported that detectable tensile plastic strain (~0.5%) as well as strain hardening phenomenon were found in developed CuZr-based BMGs [174]. They attributed the strain hardening phenomenon to the formation of nanocrystals during plastic deformation. Based on the above arguments, therefore, for the current work, it is of paramount importance to see if the strain hardening is induced by formation of nanocrystals.

Figure 5.9 shows TEM images of as-cast and deformed samples. It shows typical characteristics of amorphous structure, and the corresponding selected area electron diffraction (SAED) pattern shows halo ring for each sample.

Therefore, it can be concluded that the strain hardening behavior found in our study is not due to the formation of nanocrystals during the plastic deformation.

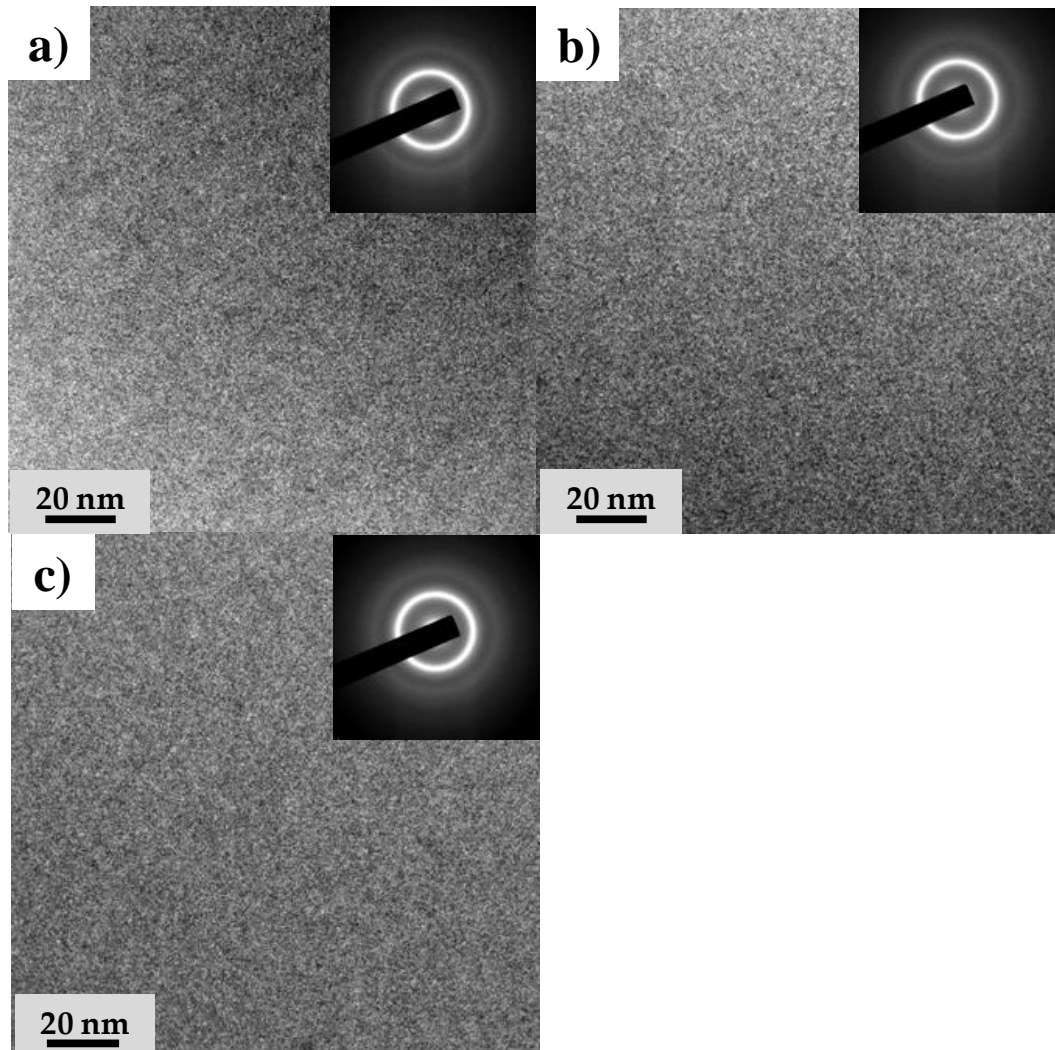


Figure 5.9 TEM images of as-cast, 2% plastically deformed and 7% plastically deformed sample.

5.3.2 Comparison between thermal annealing and mechanical annealing for BMGs

The influence of thermal annealing, which induces structural relaxation and sometimes partial crystallization in BMGs, has been widely documented [175-177]. During thermal annealing, the excess free volume is removed and causes structural relaxation of BMG. Generally, the microhardness of BMG increases as the annealing temperature increasing below T_g . As further increasing the annealing temperature, crystallization may occur. The microhardness change above T_g is not discussed in this work. To the best of our knowledge, the reported maximum hardness increase for the annealing sample is 13% higher than the as-cast sample [177].

On the other hand, mechanically induced structure change and thus has been reported in the nano-structured metals before, e.g. by indentation [178, 179] and tensile test [180-182]. Such an annealing behaviour has been also reported in metals of nano-structured materials where high stress can cause grain growth [183], elimination of dislocations [184, 185]. This is due, no doubt, to the large excess energy associated with grain boundaries in nc materials which is expected to cause instability in their nc grain size distributions. Evolution towards equilibrium can be driven, or promoted, by stress during deformation. Similarly metallic glasses are also in a thermally

non equilibrium state and mechanically it is therefore possible that mechanically driven structure can happen in metallic glasses, as long as the condition is right, i.e. high tensile stress and without shear banding. This is not seen before as the shear band dominate the deformation mechanism, thus it was hidden disguised the true mechanical phenomenon. The reason for us not to see this before is because the early premature shear banding denied our chances, it is not that the MG is not capable of hardening. It is known that metallic glasses upon annealing, volume reduction can happen. This shows that metallic glasses, can be densified mechanically just like other amorphous materials.

Based on the above argument, we speculate that in this tensile confinement condition the excess free volume is removed by the high tensile stress, which is consistent with the DSC result presented in section 5.2.2. The comparison between thermal annealing and mechanical annealing on microhardness of BMG is illustrated in **Figure 5.10**. It shows that mechanical annealing is somewhat more effective in increasing the hardness than thermal annealing. However, the maximum hardness induced by mechanical annealing is almost equal to that induced by thermal annealing, indicating a complete relaxation of the structure.

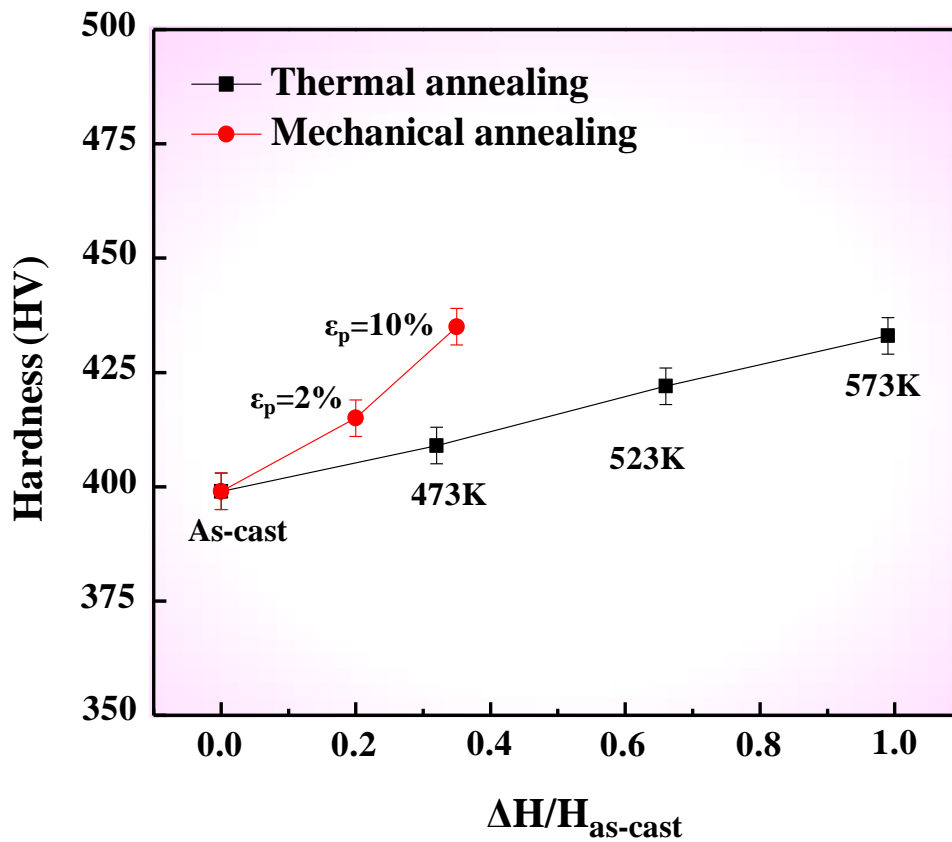


Figure 5.10 Variation of Vickers hardness as a function of reduced relaxation enthalpy.

5.3.3 Strain hardening mechanism in BMG

The DSC result undoubtedly provides the evidence that strain hardening in metallic glass is due to stress induced densification. Densification is common in polymer and ceramic materials [186]. Under high pressure, SiO₂ and other ceramics are seen to reduce their volume up to 25% [187]. These are possible primarily due to the fact that these materials have

more space and the packing density is not high. But for metallic glasses, any plastic deformation will cause increase in free volume. Even at high temperature, creep will cause increase in free volume [188].

The only few cases, where possible densification or strain hardening are reported, are either in small samples [173], or induced not by tensile stress [189, 190]. Our case is completely different, clearly increase in free volume for the first time is reported. Such a phenomenon may have presented in the deformed sample before, for example in heavily compressed or rolled specimens where multiple shear bands formed and the softening and hardening behaviours may co-exist. This is to say that while the materials softening in the shear band while rest of materials, at least parts of them harden. The hardening phenomenon is hidden either by the fact that shear banding force premature failure at low stress, or the deformed part is difficult to be separated with the shear band region. Our study shows that as long as shear banding is prevented, the region may harden. The discovery of hardening will certainly let us to rethink or reinterpretate the mechanical behaviour of metallic glasses.

5.4 Conclusion

Tensile ductility induced strain hardening and densification of BMG have been investigated. The major conclusions can be drawn as follows:

- (1) The hardness of the deformed sample increases as the plasticity increasing, which is radically different as compared with the strain induced softening commonly reported in literature. The maximum hardness increase is about 13 % higher than the as-cast sample, which is equivalent to the maximum hardness increase induced by thermal annealing.
- (2) The DSC results show a reduction in the relaxation enthalpy after plastic deformation, indicating a decrease in excess free volume. The maximum relaxation enthalpy reduction is about 40 % lower than the as-cast sample. The relaxation enthalpy reduction induced by mechanical deformation is somewhat more effective than that induced by thermal annealing.
- (3) The possibility of nanocrystallization during plastic deformation is discussed. TEM results show that the strain hardening in this study is not induced by the formation of nanocrystals during plastic deformation.

- (4) The mechanism of strain hardening is attributed to densification of the structure induced by high level of tensile stress.

Chapter 6

6 Concluding remarks

6.1 Summary of this thesis

This dissertation explored the mechanical properties of a bulk metallic glass under tensile confinement condition, aiming to provide an in-depth understanding on strength, ductility and fracture of metallic glasses. The tensile confinement condition was created by fabrication of tensile samples with variant geometries. It was firstly revealed by this thesis that the mechanical properties of BMGs under confinement condition were in stark contrast with those of unconfined condition. The main results of this thesis are summarized as follows:

- (1) The tensile plasticity of BMGs under confinement condition was examined. It was found that tensile plasticity increased with increasing the severity of confinement condition, showing a trend of continuous increase. This is contrary to the previous study which reported a decreasing trend of plasticity as increasing the stress state parameter. A possible explanation is that the material utilized in this study is a tough BMG, and the influence of defects such as micro-voids and micro-cracks can be minimized. It was also found that permanent homogeneous tensile plasticity can reach as high as 10 %, tensile elongation before fracture can reach up to ~30%, which were both much larger than those of unconfined BMGs. It indicates that a tough BMG can be even tougher under complex stress state. The unexpected tensile plasticity exhibited by BMGs under confinement condition provides a useful guideline for engineers in selection of BMGs as structural materials.
- (2) The strength of BMGs under tensile confinement was systematically investigated. It was revealed that the tensile strength increased with increasing the stress state parameter, and the highest tensile strength was up to 3.6 GPa, which is comparable to that computed from Griffith's theory. This value is approximately $E/20$ (where E is Young's

modulus), approaching the theoretic strength limit and placing this BMG among the highest strength materials. The fracture of BMGs under variant stress state was examined from a fractography point of view. It was found that the main feature of the fracture surface under uniaxial tension was the radiating vein and core structure, and the fracture was by shear banding. When decreasing the aspect ratio of the tensile specimen, the main fracture feature changed into the shearing and tensile 'dimple-like' combined structure, and the fracture angle decreased. With further decreasing the aspect ratio, the fracture surface exhibited the feature like that of a ductile metal, and 'dimple-like' structure and micro-cracks were observed on the center of the sample. Such fracture morphology evolution provides insights not only for understanding fracture mechanism but also for analyzing the failure of BMG component.

- (3) The strain hardening and densification of BMGs were studied. The microhardness test showed approximately 10% increase in hardness. In addition, DSC results also demonstrated that the relaxation enthalpy was decreased with increasing the deformation strain. These results are in sharp contrast to the previous observations of deformation induced 'strain softening' in metallic glasses, where the deformation strain is accommodated by abundant shear bands. Since the confinement

condition is created in this study, the shear banding instability can be delayed and the radically different mechanism can be revealed. The results indicate BMGs can behave like ductile materials if shear banding can be delayed or even eliminated. This study is the first to provide the definitive prove that deformation induced hardening can occur in monolithic BMGs, and is of paramount importance for fundamental understanding of deformation mechanism.

6.2 Future work

In this thesis, the mechanical properties of BMGs under tensile confinement condition were systematically studied and several original findings were unveiled. These findings are of crucial importance for understanding the nature of the deformation mechanism in metallic glasses, and supporting the application of BMGs as engineering materials. Based on the experimental results obtained, discussion presented and conclusion drawn from this research work, the following possible avenues towards future work are pointed out below.

- (1) The metallic glass used in this study was a Zr-based bulk metallic glass and it exhibited totally different behavior under the tensile

confinement condition, such as higher strength, strain-hardening behavior and 'dimple-like' fracture morphology. It would be interesting to see whether it is applicable to BMGs containing other main elements under the tensile confinement condition. For example, ductile BMG system like Pt- and Pd-, and brittle BMG systems such as Fe- and Mg-based BMGs are highly recommended.

- (2) Various tensile confinement conditions were created in this study. A quantitative comparison requires the establishment of multiaxial mechanics. The best possible approach would be to use finite element analysis to establish the stress states under tension confinement conditions in quantitative terms.
- (3) The essence of the tensile confinement method adopted in this study was to delay the instability of shear banding. For BMG, it is more prone to tensile shear instability than compressive shear instability. Therefore, the mechanical properties of BMGs under compressive confinement condition should be better. Future research should attempt to address the compressive properties under confinement condition.

Bibliography

- [1] Klement W, Willens RH, Duwez P. *Nature* 1960;187:869.
- [2] Chen HS, Turnbull D. *Acta Metall.* 1969;17:1021.
- [3] Kui HW, Greer AL, Turnbull D. *Appl. Phys. Lett.* 1984;45:615.
- [4] Inoue A. *Acta Mater.* 2000;48:279.
- [5] Peker A, Johnson WL. *Appl. Phys. Lett.* 1993;63:2342.
- [6] Inoue A, Nishiyama N, Kimura H. *Mater. Trans. JIM* 1997;38:179.
- [7] Inoue A, Zhang T, Nishiyama N, Ohba K, Masumoto T. *Mater. Trans. JIM* 1993;34:1234.
- [8] Lou HB, Wang XD, Xu F, Ding SQ, Cao QP, Hono K, Jiang JZ. *Appl. Phys. Lett.* 2011;99:
- [9] Xu DH, Duan G, Johnson WL. *Phys. Rev. Lett.* 2004;92:245504.
- [10] Jia P, Guo H, Li Y, Xu J, Ma E. *Scripta Mater.* 2006;54:2165.
- [11] Guo FQ, Poon SJ, Shiflet GJ. *Appl. Phys. Lett.* 2003;83:2575.
- [12] Tan H, Zhang Y, Ma D, Feng YP, Li Y. *Acta Mater.* 2003;51:4551.
- [13] Ma H, Shi LL, Xu J, Li Y, Ma E. *Appl. Phys. Lett.* 2005;87:181915.
- [14] Park ES, Kim DH. *J. Mater. Res.* 2005;20:1465.
- [15] Ponnambalam V, Poon SJ, Shiflet GJ. *J. Mater. Res.* 2004;19:1320.

- [16] Lu ZP, Liu CT, Thompson JR, Porter WD. *Phys. Rev. Lett.* 2004;92:245503.
- [17] Men H, Pang SJ, Zhang T. *J. Mater. Res.* 2006;21:958.
- [18] Shen J, Chen QJ, Sun JF, Fan HB, Wang G. *Appl. Phys. Lett.* 2005;86:151907.
- [19] Guo FQ, Wang HJ, Poon SJ, Shiflet GJ. *Appl. Phys. Lett.* 2005;86:091907.
- [20] Park ES, Kim DH. *J. Mater. Res.* 2004;19:685.
- [21] Schroers J, Johnson WL. *Appl. Phys. Lett.* 2004;84:3666.
- [22] Johnson WL, Fundamental aspects of bulk metallic glass formation in multicomponent alloys, in: R. Schulz (Ed.) *Metastable, Mechanically Alloyed and Nanocrystalline Materials, Pts 1 and 2*, Transtec Publications Ltd, Zurich-Uetikon, 1996, pp. 35.
- [23] Johnson WL. *MRS Bull.* 1999;24:42.
- [24] Ashby MF, Greer AL. *Scripta Mater.* 2006;54:321.
- [25] Greer AL, Ma E. *MRS Bull.* 2007;32:611.
- [26] Inoue A, Shen BL, Koshihara H, Kato H, Yavari AR. *Nat. Mater.* 2003;2:661.
- [27] Shen BL, Inoue A. *J. Phys.-Condens. Matter* 2005;17:5647.
- [28] Kakiuchi H, Inoue A, Onuki M, Takano Y, Yamaguchi T. *Mater. Trans.* 2001;42:678.
- [29] Inoue A, Takeuchi A. *Acta Mater.* 2011;59:2243.
- [30] Ashby MF. *Acta Metall.* 1972;20:887.
- [31] Spaepen F. *Acta Metall.* 1977;25:407.

- [32] Demetriou MD, Johnson WL. Mater. Sci. Eng. A-Struct. Mater. Prop. Microstruct. Process. 2004;375:270.
- [33] Demetriou MD, Johnson WL. Acta Mater. 2004;52:3403.
- [34] Demetriou MD, Johnson WL. J. Appl. Phys. 2004;95:2857.
- [35] Kawamura Y, Nakamura T, Inoue A. Scripta Mater. 1998;39:301.
- [36] Kawamura Y, Shibata T, Inoue A, Masumoto T. Scripta Mater. 1997;37:431.
- [37] Wang G, Shen J, Sun JF, Huang YJ, Zou J, Lu ZP, Stachurski ZH, Zhou BD. J. Non-Cryst. Solids 2005;351:209.
- [38] Wang G, Fang SS, Xiao XS, Hua Q, Gu HZ, Dong YD. Mater. Sci. Eng. A-Struct. Mater. Prop. Microstruct. Process. 2004;373:217.
- [39] Schroers J. JOM 2005;57:35.
- [40] Schroers J, Paton N. Advanced Materials & Processes 2006;164:61.
- [41] Lewandowski JJ, Shazly M, Nouri AS. Scripta Mater. 2006;54:337.
- [42] Schuh CA, Lund AC, Nieh TG. Acta Mater. 2004;52:5879.
- [43] Argon AS. Acta Metall. 1979;27:47.
- [44] Megusar J, Argon AS, Grant NJ. Mater. Sci. Eng. 1979;38:63.
- [45] Lu J, Ravichandran G, Johnson WL. Acta Mater. 2003;51:3429.
- [46] Cohen MH, Turnbull D. J. Chem. Phys. 1959;31:1164.
- [47] Turnbull D, Cohen MH. J. Chem. Phys. 1961;34:120.
- [48] Argon AS, Kuo HY. Mater. Sci. Eng. 1979;39:101.
- [49] Johnson WL, Samwer K. Phys. Rev. Lett. 2005;95:195501.
- [50] Leamy HJ, Chen HS, Wang TT. Metallurgical Transactions 1972;3:699.

- [51] Bruck HA, Rosakis AJ, Johnson WL. *J. Mater. Res.* 1996;11:503.
- [52] Liu CT, Heatherly L, Easton DS, Carmichael CA, Schneibel JH, Chen CH, Wright JL, Yoo MH, Horton JA, Inoue A. *Metall. Mater. Trans. A-Phys. Metall. Mater. Sci.* 1998;29:1811.
- [53] Schuh CA, Hufnagel TC, Ramamurty U. *Acta Mater.* 2007;55:4067.
- [54] Duine PA, Sietsma J, Vandenbeukel A. *Acta Metallurgica Et Materialia* 1992;40:743.
- [55] Daniel BSS, Reger-Leonhard A, Heilmaier M, Eckert J, Schultz L. *Mechanics of Time-Dependent Materials* 2002;6:193.
- [56] Wright WJ, Hufnagel TC, Nix WD. *J. Appl. Phys.* 2003;93:1432.
- [57] Jiang WH, Fan GJ, Liu FX, Wang GY, Choo H, Liaw PK. *J. Mater. Res.* 2006;21:2164.
- [58] Chen LY, Fu ZD, Zhang GQ, Hao XP, Jiang QK, Wang XD, Cao QP, Franz H, Liu YG, Xie HS, Zhang SL, Wang BY, Zeng YW, Jiang JZ. *Phys. Rev. Lett.* 2008;100:075501.
- [59] Huang YJ, Shen J, Sun JF. *Appl. Phys. Lett.* 2007;90:081919.
- [60] Kobayashi S, Maeda K, Takeuchi S. *Acta Metall.* 1980;28:1641.
- [61] Falk ML, Langer JS. *Phys. Rev. E* 1998;57:7192.
- [62] Mayr SG. *Phys. Rev. Lett.* 2006;97:195501.
- [63] Spaepen F. *Scripta Mater.* 2006;54:363.
- [64] Yang B, Wadsworth J, Nieh TG. *Appl. Phys. Lett.* 2007;90:061911.
- [65] Lee ML, Li Y, Schuh CA. *Acta Mater.* 2004;52:4121.

- [66] Argon AS, Shi LT. *Acta Metall.* 1983;31:499.
- [67] Argon AS, Shi LT. *Philos. Mag. A-Phys. Condens. Matter Struct. Defect Mech. Prop.* 1982;46:275.
- [68] Srolovitz D, Vitek V, Egami T. *Acta Metall.* 1983;31:335.
- [69] Falk ML. *Phys. Rev. B* 1999;60:7062.
- [70] Lacks DJ. *Phys. Rev. Lett.* 2001;87:225502.
- [71] Lund AC, Schuh CA. *Acta Mater.* 2003;51:5399.
- [72] Pampillo CA. *J. Mater. Sci.* 1975;10:1194.
- [73] Lewandowski JJ, Greer AL. *Nat. Mater.* 2006;5:15.
- [74] Courtney TH, *Mechanical Behaviour of Materials*, McGraw-Hill, New York, 1990.
- [75] Zhang ZF, Eckert J, Schultz L. *Acta Mater.* 2003;51:1167.
- [76] Mukai T, Nieh TG, Kawamura Y, Inoue A, Higashi K. *Intermetallics* 2002;10:1071.
- [77] He G, Lu J, Bian Z, Chen DJ, Chen GL, Tu GC, Chen GJ. *Mater. Trans. JIM* 2001;42:356.
- [78] Lowhaphandu P, Ludrosky LA, Montgomery SL, Lewandowski JJ. *Intermetallics* 2000;8:487.
- [79] Donovan PE. *Acta Metall.* 1989;37:445.
- [80] Wright WJ, Saha R, Nix WD. *Mater. Trans.* 2001;42:642.
- [81] Zhang ZF, He G, Eckert J, Schultz L. *Phys. Rev. Lett.* 2003;91:045505.
- [82] Alpas AT, Edwards L, Reid CN. *Mater. Sci. Eng.* 1988;98:501.

- [83] Bengus VZ, Diko P, Csach K, Miskuf J, Ocelik V, Korolkova EB, Tabachnikova ED, Duhaj P. *J. Mater. Sci.* 1990;25:1598.
- [84] Davis LA, Yeow YT. *J. Mater. Sci.* 1980;15:230.
- [85] Inoue A, Zhang W, Zhang T, Kurosaka K. *Acta Mater.* 2001;49:2645.
- [86] Inoue A, Sobu S, Louzguine DV, Kimura H, Sasamori K. *J. Mater. Res.* 2004;19:1539.
- [87] Lewandowski JJ, Lowhaphandu P. *Philos. Mag. A-Phys. Condens. Matter Struct. Defect Mech. Prop.* 2002;82:3427.
- [88] Mukai T, Nieh TG, Kawamura Y, Inoue A, Higashi K. *Scripta Mater.* 2002;46:43.
- [89] Noskova NI, Vildanova NF, Filippov YI, Potapov AP. *Phys. Status Solidi A-Appl. Res.* 1985;87:549.
- [90] Saida J, Inoue A. *Scripta Mater.* 2004;50:1297.
- [91] Takayama S. *Scripta Metallurgica* 1979;13:463.
- [92] Schuh CA, Lund AC. *Nat. Mater.* 2003;2:449.
- [93] Vaidyanathan R, Dao M, Ravichandran G, Suresh S. *Acta Mater.* 2001;49:3781.
- [94] Donovan PE. *Mater. Sci. Eng.* 1988;98:487.
- [95] Bailey NP, Schiotz J, Jacobsen KW. *Phys. Rev. B* 2006;73:
- [96] Schroers J, Johnson WL. *Phys. Rev. Lett.* 2004;93:255506.
- [97] Liu YH, Wang G, Wang RJ, Zhao DQ, Pan MX, Wang WH. *Science* 2007;315:1385.

- [98] Han Z, Wu WF, Li Y, Wei YJ, Gao HJ. *Acta Mater.* 2009;57:1367.
- [99] Sunny G, Yuan F, Prakash V, Lewandowski J. *Exp. Mech.* 2009;49:479.
- [100] Sunny G, Lewandowski J, Prakash V. *J. Mater. Res.* 2007;22:389.
- [101] Wu WF, Li Y, Schuh CA. *Philos. Mag.* 2008;88:71.
- [102] Wu FF, Zhang ZF, Mao SX, Eckert J. *Philos. Mag. Lett.* 2009;89:178.
- [103] Bei H, Xie S, George EP. *Phys. Rev. Lett.* 2006;96:105503.
- [104] Guo H, Yan PF, Wang YB, Tan J, Zhang ZF, Sui ML, Ma E. *Nat. Mater.* 2007;6:735.
- [105] Luo JH, Wu FF, Huang JY, Wang JQ, Mao SX. *Phys. Rev. Lett.* 2010;104:215503.
- [106] Conner RD, Dandliker RB, Johnson WL. *Acta Mater.* 1998;46:6089.
- [107] Choi-Yim H, Johnson WL. *Appl. Phys. Lett.* 1997;71:3808.
- [108] Leonhard A, Xing LQ, Heilmaier M, Gebert A, Eckert J, Schultz L. *Nanostructured Materials* 1998;10:805.
- [109] Choi-Yim H, Busch R, Koster U, Johnson WL. *Acta Mater.* 1999;47:2455.
- [110] Hays CC, Kim CP, Johnson WL. *Phys. Rev. Lett.* 2000;84:2901.
- [111] Inoue A, Zhang T, Chen MW, Sakurai T, Saida J, Matsushita M. *J. Mater. Res.* 2000;15:2195.
- [112] Kim CP, Busch R, Masuhr A, Choi-Yim H, Johnson WL. *Appl. Phys. Lett.* 2001;79:1456.
- [113] Xu YK, Xu J. *Scripta Mater.* 2003;49:843.
- [114] Lee JC, Kim YC, Ahn JP, Kim HS. *Acta Mater.* 2005;53:129.

- [115] Hofmann DC, Suh JY, Wiest A, Duan G, Lind ML, Demetriou MD, Johnson WL. *Nature* 2008;451:1085.
- [116] Wu Y, Xiao YH, Chen GL, Liu CT, Lu ZP. *Advanced Materials* 2010;22:2770.
- [117] Takayama S. *Mater. Sci. Eng.* 1979;38:41.
- [118] Zhao JX, Wu FF, Qu RT, Li SX, Zhang ZF. *Acta Mater.* 2010;58:5420.
- [119] Lee JC, Kim YC, Ahn JP, Kim HS, Lee SH, Lee BJ. *Acta Mater.* 2004;52:1525.
- [120] Wang D, Li Y, Sun BB, Sui ML, Lu K, Ma E. *Appl. Phys. Lett.* 2004;84:4029.
- [121] Sun BB, Wang YB, Wen J, Yang H, Sui ML, Wang JQ, Ma E. *Scripta Mater.* 2005;53:805.
- [122] Chen LY, Zeng YW, Cao QP, Park BJ, Chen YM, Hono K, Vainio U, Zhang ZL, Kaiser U, Wang XD, Jiang JZ. *J. Mater. Res.* 2009;24:3116.
- [123] Wu WF, Zhang CY, Zhang YW, Zeng KY, Li Y. *Intermetallics* 2008;16:1190.
- [124] Chen HS, Krause JT, Coleman E. *J. Non-Cryst. Solids* 1975;18:157.
- [125] Lewandowski JJ, Wang WH, Greer AL. *Philos. Mag. Lett.* 2005;85:77.
- [126] Hajlaoui K, Yavari AR, LeMoulec A, Botta WJ, Vaughan FG, Das J, Greer AL, Kvik A. *J. Non-Cryst. Solids* 2007;353:327.
- [127] Hajlaoui K, Yavari AR, Doisneau B, LeMoulec A, Botta WJF, Vaughan G, Greer AL, Inoue A, Zhang W, Kvik A. *Scripta Mater.* 2006;54:1829.

- [128] Oh JC, Ohkubo T, Kim YC, Fleury E, Hono K. *Scripta Mater.* 2005;53:165.
- [129] Du XH, Huang JC, Hsieh KC, Lai YH, Chen HM, Jang JSC, Liaw PK. *Appl. Phys. Lett.* 2007;91:131901.
- [130] Yao KF, Ruan F, Yang YQ, Chen N. *Appl. Phys. Lett.* 2006;88:122106.
- [131] Yao KF, Zhang CQ. *Appl. Phys. Lett.* 2007;90:061901.
- [132] Park ES, Kim DH. *Acta Mater.* 2006;54:2597.
- [133] Yokoyama Y, Fujita K, Yavari AR, Inoue A. *Philos. Mag. Lett.* 2009;89:322.
- [134] Volkert CA, Donohue A, Spaepen F. *J. Appl. Phys.* 2008;103:083539.
- [135] Shan ZW, Li J, Cheng YQ, Minor AM, Asif SAS, Warren OL, Ma E. *Phys. Rev. B* 2008;77:155419.
- [136] Yavari AR, Georgarakis K, Botta WJ, Inoue A, Vaughan G. *Phys. Rev. B* 2010;82:172202.
- [137] Shiflet GJ, He Y, Poon SJ. *J. Appl. Phys.* 1988;64:6863.
- [138] Zhang ZF, Eckert J. *Phys. Rev. Lett.* 2005;94:094301.
- [139] Pan J, Chen Q, Liu L, Li Y. *Acta Mater.* 2011;59:5146.
- [140] Harmon JS, Demetriou MD, Johnson WL, Samwer K. *Phys. Rev. Lett.* 2007;99:135502.
- [141] Bridgman PW. *Studies of large plastic flow and fracture.* Harvard University Press, Cambridge, MA, 1964.
- [142] Flores KM, Dauskardt RH. *Acta Mater.* 2001;49:2527.
- [143] Zhu T, Li J, Ogata S, Yip S. *MRS Bull.* 2009;34:167.

- [144] Zhu T, Li J. Progress in Materials Science 2010;55:710.
- [145] Orowan E. Reports on Progress in Physics 1948;12:185.
- [146] Pokluda J, Cerny M, Sandera P, Sob M. Journal of Computer-Aided Materials Design 2004;11:1.
- [147] Frenkel J. Z. Phys. 1926;37:572.
- [148] Orowan E. Z. Phys. 1934;89:605.
- [149] Taylor GI. Proceedings of the Royal Society of London Series a-Mathematical and Physical Sciences 1934;146:0501.
- [150] Ogata S, Li J, Hirosaki N, Shibutani Y, Yip S. Phys. Rev. B 2004;70:104104.
- [151] Griffith AA. Philos. Trans. R. Soc. London 1920;221A:163.
- [152] Bouchbinder E, Langer JS, Procaccia I. Phys. Rev. E 2007;75:036107.
- [153] Zink M, Samwer K, Johnson WL, Mayr SG. Phys. Rev. B 2006;73:172203.
- [154] Schall P, Weitz DA, Spaepen F. Science 2007;318:1895.
- [155] Pan D, Inoue A, Sakurai T, Chen MW. Proc. Natl. Acad. Sci. U. S. A. 2008;105:14769.
- [156] Miracle DB. Nat. Mater. 2004;3:697.
- [157] Sheng HW, Luo WK, Alamgir FM, Bai JM, Ma E. Nature 2006;439:419.
- [158] Brenner SS. J. Appl. Phys. 1956;27:1484.
- [159] Coleman RV, Sears GW. Acta Metall. 1957;5:131.
- [160] Wu B, Heidelberg A, Boland JJ, Sader JE, Sun XM, Li YD. Nano Letters 2006;6:468.
- [161] Wu B, Heidelberg A, Boland JJ. Nat. Mater. 2005;4:525.

- [162] Greer JR, Nix WD. *Phys. Rev. B* 2006;73:245410.
- [163] Volkert CA, Lilleodden ET. *Philos. Mag.* 2006;86:5567.
- [164] Spaepen F. *Nat. Mater.* 2006;5:7.
- [165] Slipenyuk A, Eckert J. *Scripta Mater.* 2004;50:39.
- [166] Liu JW, Cao QP, Chen LY, Wang XD, Jiang JZ. *Acta Mater.* 2010;58:4827.
- [167] Haruyama O, Nakayama Y, Wada R, Tokunaga H, Okada J, Ishikawa T, Yokoyama Y. *Acta Mater.* 2010;58:1829.
- [168] Steif PS, Spaepen F, Hutchinson JW. *Acta Metall.* 1982;30:447.
- [169] Kanungo BP, Glade SC, Asoka-Kumar P, Flores KM. *Intermetallics* 2004;12:1073.
- [170] Flores KM, Suh D, Dauskardt RH, Asoka-Kumar P, Sterne PA, Howell RH. *J. Mater. Res.* 2002;17:1153.
- [171] Li J, Wang ZL, Hufnagel TC. *Phys. Rev. B* 2002;65:144201.
- [172] Deng QS, Cheng YQ, Yue YH, Zhang L, Zhang Z, Han XD, Ma E. *Acta Mater.* 2011;59:6511.
- [173] Jang DC, Greer JR. *Nat. Mater.* 2010;9:215.
- [174] Pauly S, Gorantla S, Wang G, Kuhn U, Eckert J. *Nat. Mater.* 2010;9:473.
- [175] Xie S, George EP. *Acta Mater.* 2008;56:5202.
- [176] Ramamurty U, Jana S, Kawamura Y, Chattopadhyay K. *Acta Mater.* 2005;53:705.
- [177] Dmowski W, Fan C, Morrison ML, Liaw PK, Egami T. *Mater. Sci. Eng. A-Struct. Mater. Prop. Microstruct. Process.* 2007;471:125.

- [178] Zhang K, Weertman JR, Eastman JA. *Appl. Phys. Lett.* 2004;85:5197.
- [179] Jin M, Minor AM, Stach EA, Morris JW. *Acta Mater.* 2004;52:5381.
- [180] Gianola DS, Van Petegem S, Legros M, Brandstetter S, Van Swygenhoven H, Hemker KJ. *Acta Mater.* 2006;54:2253.
- [181] Legros M, Gianola DS, Hemker KJ. *Acta Mater.* 2008;56:3380.
- [182] Fan GJ, Fu LF, Choo H, Liaw PK, Browning ND. *Acta Mater.* 2006;54:4781.
- [183] Rupert TJ, Gianola DS, Gan Y, Hemker KJ. *Science* 2009;326:1686.
- [184] Shan ZW, Mishra RK, Asif SAS, Warren OL, Minor AM. *Nat. Mater.* 2008;7:115.
- [185] Huang L, Li QJ, Shan ZW, Li J, Sun J, Ma E. *Nature Communications* 2011;2:547.
- [186] Rouxel T, Ji H, Hammouda T, Moreac A. *Phys. Rev. Lett.* 2008;100:225501.
- [187] Bridgman PW, Simon I. J. *Appl. Phys.* 1953;24:405.
- [188] Ott RT, Kramer MJ, Besser MF, Sordelet DJ. *Acta Mater.* 2006;54:2463.
- [189] Caron A, Kawashima A, Fecht HJ, Louzguine-Luzguin DV, Inoue A. *Appl. Phys. Lett.* 2011;99:171907.
- [190] Concustell A, Mear FO, Surinach S, Baro MD, Greer AL. *Philos. Mag. Lett.* 2009;89:831.